Search for Non-thermal Dark Matter in Monojet Events in Proton-Proton Collisions at $\sqrt{s}$ = 13 TeV

by

Sonaina Undleeb, M.Sc., M.Phil.

A Dissertation

In

PHYSICS

Submitted to the Graduate Faculty
of Texas Tech University in
Partial Fulfillment of
the Requirements for the Degree of

DOCTOR OF PHILOSOPHY

Pending Approval

Dr. Shuichi Kunori
Chair of Committee

Dr. Nural Akchurin

Dr. Sung-Won Lee

Dr. Teruki Kamon

Dr. Giorgio Bornia

Dean of the Graduate School

Dr. Rauf Arif

December, 2017

ACKNOWLEDGEMENTS

I would like to express my sincere gratitude to my advisor Dr. Shuichi Kunori for the continuous support of my Ph.D. research, for his patience, motivation and vast knowledge. His guidance helped me throughout my research period as well as during thesis writeup. I could not have imagined having a better advisor and mentor for my Ph.D. study. I would also like to thank the rest of my thesis committee: Dr. Sung Won Lee, Dr. Nural Akchurin, Dr. Teruki Kamon and Dr. Giorgio Bornia for their perspicacious comments and encouragement. My heartfelt appreciation also goes to TTU High Energy Physics group for always being supportive and providing a very comfortable and friendly research environment.

Last but not least, I would like to thank my family: my parents, husband, son and my siblings for their continuous support throughout my Ph.D. and my life.

TABLE OF CONTENTS

ABSTRACT

This dissertation presents a search for dark matter in events with one or more jets and large missing transverse energy using proton-proton collisions at center-of-mass energy of 13 TeV. The data was collected in 2016 by the Compact Muon Solenoid (CMS) detector at the Large Hadron Collider (LHC) corresponding to an integrated luminosity of 35.9 fb^{-1}. The results are interpreted in terms of Light Non-thermal dark matter model which explains presence of dark matter as well as baryon asymmetry in the universe. Model independent limit on narrow resonance is also obtained for monojet dominant coupling parameter space. There is no evidence for an excess of events above the background processes in the signal region, therefore cross section limits are set for different mediator masses.

LIST OF TABLES

LIST OF FIGURES

LIST OF ABBREVIATIONS

ALICE: A Large Ion Collider Experiment

ATLAS: A Toroidal LHC ApparatuS

CERN: European Organization for Nuclear Research

CMB: Cosmic Microwave Background

CMS: Compact Muon Solenoid

CR: Control Region

CSC: Cathode Strip Chamber

DAQ: Data AcQuisition system

DT: Drift Tube

EM: ElectroMagnetic

ECAL: Electromagnetic CALorimeter

EWK: Electromagnetic and WeaK interaction

ES: Endcap preShower

GEANT: GEometry ANd Tracking

HB: Hadronic Barrel

HCAL: Hadronic CALorimeter

HE: Hadronic Endcap

HF: Hadronic Forward

HLT: High Level Trigge

HO: Hadronic Outer

ISGS: Initial State Gluon Splitting

JEC: Jet Energy Correction

JES: Jet Energy Scale

JER: Jet Energy Resolution

L1T: Level-1 Trigger

LO: Leading Order

LHC: Largh Hadron Collider

LHCb: Large Hadron Collider Beauty experiment

MC: Monte Carlo

MET: Missing Transverse Energy

NLO: Next-to-Leading Order

NNLL: Next-to-Next-to-Leading-Log

NNLO: Next-to-Next-to-Leading Order

NLL: Next-to-Leading Logarithmic

PAT: Physics Analysis Tool

PDF: Parton Distribution Function

PF: Particle Flow

POG: Particle Object Group

PU: PileUp

QCD: Quantum ChromoDynamics

QED: Quantum ElectroDynamics

RECO: offline RECOnstruction

RPC: Resistive Plate Chamber

SDSS: Sloan Digital Sky Survey

SHERPA: Simulation of High-Energy Reactions of PArticles

SM: Standard Model

SUSY: SUperSYmmetry

CHAPTER 1
MOTIVATION AND THEORETICAL BACKGROUND

The Standard Model of particle physics (SM) has always been appreciated by physicists as it does not just describe the known particles (like electron and quarks) but it also predicts new particles e.g. Higgs. But while it is incredible, it does not provides a complete picture of the Universe, for example it cannot account for the dark matter and dark energy which makeup 95% of Universe. Therefore physicists are actively considering alternatives like physics beyond the Standard Model, particularly to explain dark matter and origin of the matter in the Universe. There are strong cosmological observations for non-baryonic dark matter and among others candidates, the weakly interacting massive particles (WIMPs) describe particle dark matter candidates which are highly motivated by particle as well as astrophysics [1–3]. On the other hand, several broad and comprehensive searches are looking for wide range of non-WIMP candidates in parallel, which can provide explanation for dark matter existence and baryon asymmetry. Dark matter and baryonic matter are mysteriously related and modern physics is trying to solve the pressing puzzle that "why dark matter's density is so close to the baryonic matter density i.e. $\Omega_{DM} \approx 5\Omega_B$?". Moreover anti-matter is not included into visible matter density, which leads to asymmetric universe with an initial excess of baryons over anti-baryons. Non-WIMPs models are highly motivated since they account for the origin of the observed baryon asymmetry, dark matter, strong CP problem, and the gauge hierarchy problem [4–6]. This dissertation includes review and study of Light Non-thermal DM model, which explains both the presence of dark matter and imbalance of baryonic matter in the Universe.

The first section of this chapter gives an overview of Standard Model particle content and their properties. The second and third sections incorporate Physics beyond SM and description on dark matter including signatures, potential candidates and detection strategies.

1.1 The Standard Model

The Standard Model of particle physics is a theory which describes the fundamental constituents of Universe and their interactions. It incorporates all the known elementary particles as well as the fundamental forces to hold these particle together. This theory was formulated in 1970s through the work of many scientists around the globe [8]. Discoveries of top quark (1995) [9], tau neutrino (2000) [10] and Higgs boson (2012) [11] [12] demonstrate a great success of SM. Moreover it has proven itself useful in predicting several properties of weak neutral currents and the W and Z bosons with a great accuracy.

1.1.1 Particles

SM includes seventeen fundamental particles which are divided into further classes as shown in Figure 1.1. These particles can be distinguished in terms of their properties e.g. electromagnetic and color charges, spin and hypercharge etc. Further classifications of these elementary particles include fermions (6 quarks and 6 leptons) and bosons (4 gauge bosons and a Higgs boson). Fermions are spin half $(1/2)$ particles and follow the Pauli exclusion principal which states that no two fermions can occupy the same place at the same time. Each fermion has an antiparticle whose charge is opposite to the fermion. Quarks come in six flavors *(up*, *down*, *charm*, *strange*, *top*, *bottom)*. A distinguishing property of quarks is that they carry color charge in addition to electromagnetic charge and weak isospin, which allows them to interact with other particles through strong force. Quarks do not exist individually rather they form composite particles namely mesons (quark doublets) and baryons (quark triplets), which are collectively called as hadrons. Proton and neutron (together nucleons) are the two familiar baryons with lowest mass. Characteristics of quarks are enlisted in Table 1.1.

The remaining six fermions are called leptons and do not carry color charge. Historically leptons were considered to be light particles and hadrons were believed to be the heavy ones but this perception did not hold anymore with the discovery of tau lepton (weighs almost
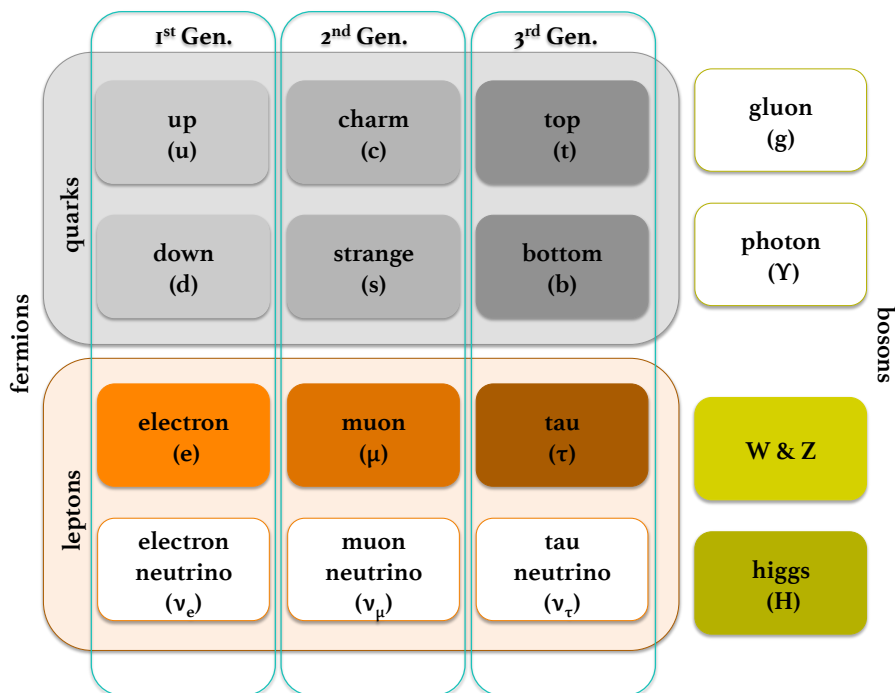
Figure 1.1: Particle contents of Standard Model. Color flow (from light to dark) represents lighter to massive particles, white represents massless particles.

twice the proton mass). Neutrinos form an important subgroup within the leptons. They are almost massless and come in three flavors, matched to their partner leptons ie. electron, muon and tau. They do not posses any electric charge either and hence weak interaction is the only permissible interaction which makes their detection quite challenging.

Quark	Discovered	Spin	Electric Charge	Color Charge	Mass (MeV/c^2)
up (u)	1968	1/2	$+\,2/3$	r, g, b	2.3
down (d)	1968	1/2	$-\,1/3$	r, g, b	4.8
charm (c)	1970	1/2	$+\,2/3$	r, g, b	1275
strange (s)	1968	1/2	$-\,1/3$	r, g, b	95
top (t)	1995	1/2	$+\,2/3$	r, g, b	173,200
bottom (b)	1977	1/2	$-\,1/3$	r, g, b	4,420

Table 1.1: SM quarks and their properties.

The quarks and leptons are grouped into three generations with corresponding particles

possess similar physics behavior as shown in Figure 1.1. Stable particles (hadrons) are made up of generation 1 (e.g. stable atoms made of electrons, protons, and neutrons) whereas generation 2 always constitute unstable hadrons. The longest lived particle, containing quark form this generation, is the lambda (Λ) baryon which is made up of *up*, *down* and *strange* quarks with life time 10^{-9} seconds. Particle form generation 3 are the heaviest particles which decay with very short half life. Leptons and their properties are enlisted in Table 1.2.

Lepton	Discovered	Spin	Electric Charge	Mean Life (s)	Mass (MeV/c^2)
electron (e)	1897	1/2	-1	∞	0.511
electron neutrino (ν_e)	1956	1/2	0		$< 10^{-5}$
muon (μ)	1936	1/2	-1	2.197×10^{-6}	105.7
muon neutrino (ν_μ)	1962	1/2	0		$< 10^{-5}$
tau (τ)	1975	1/2	-1	$(291 \pm 1.5) \times 10^{-15}$	1777
tau neutrino (ν_τ)	2000	1/2	0		$< 10^{-5}$

Table 1.2: SM leptons and their properties.

Other than fermions there are four gauge bosons which are defined as force carriers of fundamental interactions. These interactions occur via exchange of gauge bosons, generally known as force mediator particles .Microscopically the effect of such exchange is equivalent to the force influencing both the particles and therefore the exchange particle is referred to have mediated that force. All the gauge bosons are spin 1 particles and in contrast to fermions, they do not obey the Pauli exclusion principle which means they do not have any theoretical restriction on their spatial density. The SM mediators are photons (γ), W^+, W^-, Z and gluons. Photons are massless and are responsible for electromagnetic force between electrically charged particles. Theory of quantum electrodynamics explains photons very well. Gauge bosons W^+, W^- and Z are mediators of weak interactions influencing quarks and leptons. $W^\pm$ bosons have mass (≈ 80 GeV) each and have ± 1 electric charge whereas Z is neutral with mass (≈ 90 GeV). Moreover $W^\pm$ only interact with left handed particles and right handed antiparticles whereas Z mediates interaction with both left handed particles

and antiparticles.

Boson	Interaction field	Spin	Electric Charge	Color Charge	Mass (GeV/c^2)
gluon (g)	Strong	1	0	8 colors	0
photon (γ)	Electromagnetic	1	0	none	0
$W^\pm$	Weak	1	± 1	none	80.39
Z	Weak	1	0	none	91.19
Higgs (H)		0	0	none	125.9

Table 1.3: SM bosons, their interactions and properties.

The last gauge boson is gluon which comes in eight types and acts as the exchange particle for the strong force between quarks. All gluons carry color charge (red, green or blue) and therefore also participate in the strong interactions, which makes it harder to understand the theory of Quantum Chromodynamics (QCD). There are color singlet and color octet states for gluons where singlet states can only interact with other singlets but since strong force is very short ranged therefore such type of interaction does not exist and so the gluon in the singlet state [13–19]. These states are linearly independent and are given below

$$\frac{r\bar{r} + b\bar{b} + g\bar{g}}{\sqrt{3}} \tag{1.1}$$

Above expression represents color singlet states while octet states are given in 1.2.

$$\frac{r\bar{b} + b\bar{r}}{\sqrt{2}}$$

$$\frac{-i(r\bar{b} - b\bar{r})}{\sqrt{2}}$$

$$\frac{r\bar{g} + g\bar{r}}{\sqrt{2}}$$

$$\frac{-i(r\bar{g} - g\bar{r})}{\sqrt{2}}$$

$$\frac{b\bar{g} + g\bar{b}}{\sqrt{2}}$$ (1.2)

$$\frac{-i(b\bar{g} - g\bar{b})}{\sqrt{2}}$$

$$\frac{r\bar{r} - b\bar{b}}{\sqrt{2}}$$

$$\frac{r\bar{r} + b\bar{b} - 2g\bar{g}}{\sqrt{6}}$$

Finally Higgs boson is the last boson in the list which is a scalar massive particle, theorized in 1964 by Peter Higgs [20], when all the attempts to create a gauge invariant theory for weak force were completely unsuccessful. The gauge symmetry predicts that gauge bosons for electromagnetic and weak forces i.e. photon, $W^{\pm}$ and Z should be massless but since except photon all of them are massive therefore electroweak symmetry breaks [21]. The results of 1962 [22]and 1963 [23] research studies concluded that the electroweak symmetry would be broken in presence of an unfamiliar field and consequently some of the particles would acquire mass. This unusual field was referred to as Higgs field and corresponding symmetry breaking phenomena was named as Higgs mechanism. Higgs field is assumed to be everywhere and building blocks of matter (quarks and leptons) and gauge bosons ($W^{\pm}$ and Z), moving around through space, interact with this field and therefore acquire mass. On the other hand gluon and photon are massless as they are not influenced by Higgs field. Interestingly Higgs boson interacts with its own field and this is the reason it is massive. In

addition Higgs boson is not like other SM gauge bosons because Higgs mechanism does not result in any kind of force (like the strong, electromagnetic, and weak forces) [20–24]. Being a very massive particle, Higgs boson decays immediately after it is produced. The only way to confirm its existence is through high energy particle accelerators and experiments at Large Hadron Collider (LHC) played a very significant role in this regard. The Higgs hunt was started with experiments at LHC (CERN) in early 2010 and at Tevatron (Fermilab) till the end of 2011 and finally on 4th July 2012 both CMS [11] (Figure 1.2) and ATLAS experiments [12] independently confirmed the existence of Higgs boson with mass of 125 GeV. Characteristics of Higgs boson and gauge bosons along with their interactions are given in Table 1.3.
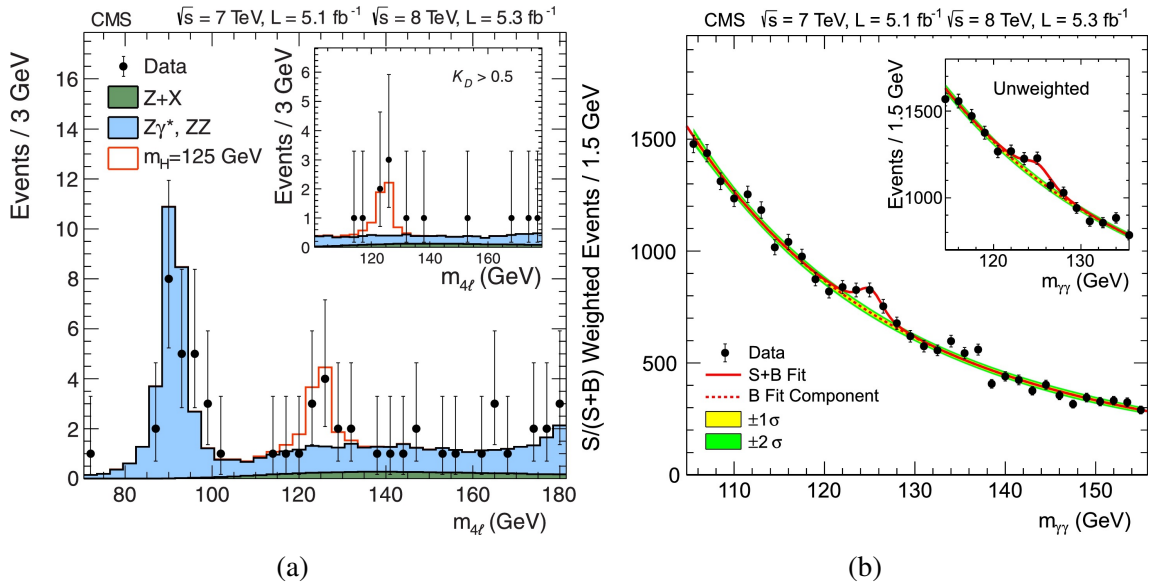
Figure 1.2: Figure demonstrates CMS results in terms of invariant mass distribution of (a) four leptons in $H \rightarrow Z \rightarrow 4l$ and (b) diphoton in $H \rightarrow 2\gamma$. Higgs boson signal with mass 125 GeV and added background expectation are shown [11].

1.1.2 Interactions

Fundamental interactions or forces are those which are irreducible to more basic interactions. There are four such known forces, namely strong, electromagnetic, weak and gravity,

mathematically each of them is described as field. Gravitational force is explained by Einstein's theory of general relativity and is referred to the spacetime curvature. Remaining three are called discrete quantum fields and are very well explained by SM.

Gluons mediate strong interactions as they "glue" quarks together to form hadrons e.g. proton and neutron which form structure of atomic nuclei. Photons are carrier of electromagnetic interactions, where electric and magnetic fields are responsible for chemical bonding and electromagnetic waves. Weak force is mediated by $W^{\pm}$ and Z bosons and acts on both quarks and leptons. An example of weak interaction is β decay.

Electromagnetic force influences electrically charged particles and includes both electrostatic force as well as combined effect of electric and magnetic forces for moving charges. It is a long range force and describes many everyday phenomena like friction, lightening and working of electric current devices e.g. television, scanner and computers etc. Electric and magnetic phenomena are historically known and in 19th century it was discovered that both of these phenomena are actually two different aspects of same interaction. Later this merged interaction was quantified by Maxwell in 1864. Electromagnetic and weak interactions are combined into electroweak interactions at above the unification energy ≈ 246 GeV. It is important to understand this unified theory as it plays an important role in understanding modern cosmology and evolution of the Universe.

Strong force is very short range force which exists only within atomic nucleus ($\approx 10^{-15}$m) and therefore is the most complex SM interaction. Outside the nucleus this force just vanishes. After the discovery of nucleus in 1908, it was clear that there exists another type of force that is strong enough to overcome the electrostatic repulsion between protons inside an atomic nucleus. Presence of such force ensures the existence of nucleus and is known as nuclear force.

It is believed that all of these forces are related and can be merged into one single force at very high energy (Planck scale). So far the high energy particle accelerator cannot reach such high energy to experimentally probe this. It will not be wrong to say that devising

theoretical frame work for unified forces will be one of the greatest achievement in theory of particle physics. Electromagnetic and weak forces have already been unified with the Nobel winning electroweak theory of Sheldon Glashow, Abdus Salam, and Steven Weinberg whereas efforts are being made in developing Grand Unification Theory (GUT) for further merger of electroweak and strong forces. [13–19]

1.2 Physics Beyond Standard Model

The standard model of elementary particles (SM) agrees very well with experiment but it leaves some phenomena unexplained. Following are some of them:

- What is the origin of particles masses?

- What is the nature of dark matter and dark energy?

- How one can explain the neutrino masses and mixing?

- What is the origin of imbalance in baryonic matter and antibaryonic matter?

In order to find answers to these and several other questions, particle physicists have been interested in physics beyond the Standard Model (BSM). The infinite possibilities open up when we go beyond the standard model [25–27].

1.3 Dark Matter

There is enormous astrophysical and cosmological evidence for presence of dark matter(DM) in our universe [28]. According to the recent measurements from the Planck mission, the baryonic matter makes up 4.9% of the Universe whereas dark matter 26.6% and the remaining 68.5% contribution comes form the dark energy [29]. Dark matter is dark as it is not in the form of visible stars and planets. Secondly it is not in form of dark clouds of normal matter otherwise they could be detected by their absorption of radiation passing through them. Thirdly it is not antimatter as we would be able to see the unique gamma rays in its annihilation with the matter.

1.3.1 Evidence

- The Galactic Scale

Observation of galaxies rotation curves gives most compelling and direct evidence for dark matter. The observed rotation curve shows a typical flat behavior at large distances as shown in Figure 1.3, whereas according to Newtonian dynamics the circulation velocity should be falling $\propto 1/\sqrt{r}$ beyond the optical disk [28].

$$v(r) = \sqrt{\frac{GM(r)}{r}} \tag{1.3}$$

$M(r)$ is given by $M(r) \equiv 4\pi \int \rho(r)r^2 dr$ where $\rho(r)$ is the mass density. The flat behavior means the velocity $v(r)$ is approximately constant and hence indicates the presence of a halo with $M(r) \propto r$ and $\rho \propto 1/r^2$.
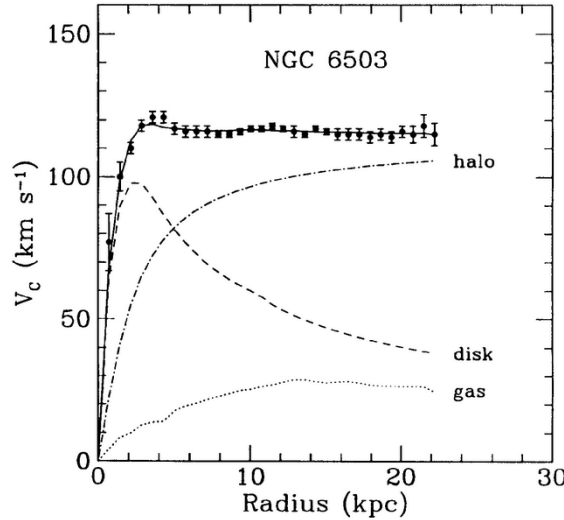
Figure 1.3: Rotation curve of NGC 6503 for gas, disk and dark matter [42].

Strong gravitational lensing of elliptical galaxies also provide evidence for dark matter [30] e.g. presence of substructure around distinct massive elliptical galaxies via weak modulation of strong lensing [31, 32]. Another signature comes from the Oort discrepancy in the disk of Milky Way which refers to the insufficient number of ob-

served stars around sun and thus the necessary balance must be made by some unob-
served matter [33]. Further evidence include: weak gravitational lensing of faraway
galaxies by foreground structure [34], the velocity dispersions of dwarf spheroidal
galaxies which are found to be larger than predictions based on the assumption that the
mass-to-light ratios should be similar to those observed in globular clusters [35, 36],
the velocity dispersions of spiral galaxy satellites which infer dark halo presence
around the spiral galaxies [37, 38].

- The Scale of Galaxy Clusters

Galaxy cluster scales give a strong signature of dark matter. In a study, velocity dis-
persion of galaxies in the Coma cluster was measured which inferred the mass-to-light
ratio of approximately 400 solar mass per solar luminosity. This value exceeds the
ratio in the solar neighborhood by two order of magnitude [38] and most recent esti-
mates are also consistent [39–41].

Various methods can be used to find cluster mass e.g. weak gravitational lensing,
by applying virial theorem to observed distributions of radial velocities and by look-
ing into hot emitting gas distribution in clusters by studying X-ray emission. For a
system with spherical symmetry, the equation of hydrostatic equilibrium is given as
following:

$$\frac{1}{\rho}\frac{dP}{dr} = -a(r) \tag{1.4}$$

where P is pressure, ρ is the density and a is acceleration of the gas, at radius r.
Above expression can be rewritten in terms of temperature for an ideal gas.

$$\frac{d\log\rho}{d\log r} + \frac{d\log T}{d\log r} = -\frac{r}{T}(\frac{\mu m_p}{k})a(r) \tag{1.5}$$

m_p refers to mass of proton. This equation can be further simplified by considering

the fact that the outside the core, temperature of clusters is approximately constant and at large radii, density of observed gas follows a power law. The temperature found in such way and corresponding observed temperature are inconsistent and hence proposes the existence of significant amount of dark matter inside the cluster.

These results can be checked against gravitational lensing data estimates. According to Einstein's theory of general relativity, mass bends light. The gravitational field lines of massive objects expand over large distances in space cause the near by passing light rays deviate and refocus somewhere else. The gravitational mass of the cluster distorts the images of background objects which can be used to predict the shape of potential well and thus cluster's mass [44]. Figure 1.4 shows Hubble Space Telescope image of galaxy cluster where light arcs are result of strong gravitational lensing.
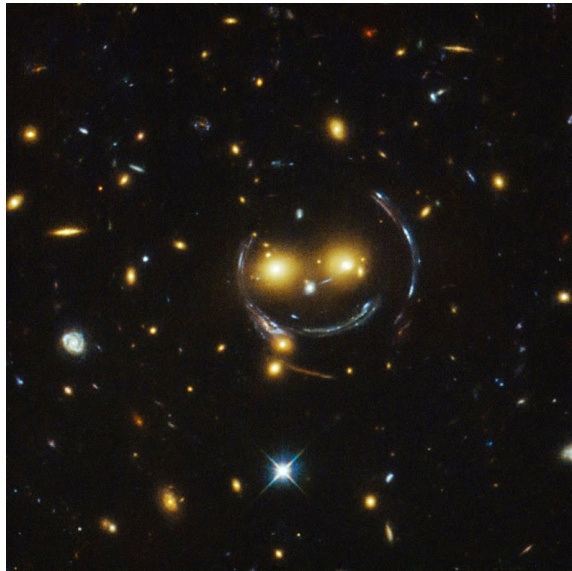
Figure 1.4: Hubble Space Telescope image of galaxy cluster SDSS J1038+4849 showing light arcs caused by strong gravitational lensing [51].

- Cosmological Scales

  Analysis of Comic Microwave Background (CMB) which is the leftover heat of Big Bang, helps to estimate the total amount of dark matter in our universe [45, 46]. Re-

sults of several CMB experiments e.g. WMAP [47], ACBAR [48] and CBI [49] and cosmological measurements obtained by SDSS [47] are consistent with Big Bang nucleosynthesis predictions [50].

1.3.2 Dark Matter Candidates

Previous section describes several compelling evidence of dark matter existence so it is natural to ask what is dark matter comprised of? This section includes some of the proposed candidates in the literature.

1.3.2.1 Thermal Dark Matter

Thermal production is a mechanism in which dark matter was created from particles in thermal equilibrium in the early universe. After Big Bang when temperature of Universe was extremely high, the thermal equilibrium obtained and number densities of dark matter particles (Weakly Interacting Massive Particles) and photons were approximately equal to each other. The number of both WIMPs and photons dropped together with the decrease in temperature and as soon as the temperature reduced below the mass of WIMPs, the number of such particles started to drop exponentially. The annihilation of WIMPs stopped at certain point when their density decreased enough that probability of finding another WIMP to annihilate became small. This situation is called "freeze-out" with significant number of WIMPs still present in the Universe and their final relic density is insensitive to the initial conditions [2, 3]. The main properties of WIMPs are described below.

- Weakly Interacting Massive Particles (WIMPs)

  The key features of this particle class are as follows: interaction around typical weak-force, interactions with fine structure constant $\alpha \sim 10^{-2}$ and particle mass near the weak scale $m \sim 100$ GeV. Supersymmetric nutralino and Kaluza-Klein photon are theoretical WIMPs, introduced to look for new physics at the electroweak breaking scale and possibly explain the difference with Planck scale [52–54].

1.3.2.2 Non-thermal Dark Matter

In contrast to thermal production, non-thermal dark matter is believed not to be in thermal equilibrium with the plasma in the early universe and was created in decays of heavier particles or extended structures. the final relic abundance of such particles can be completely determined by the initial conditions [2]. Theorists proposed several non-thermal dark matter models like Supersymmetric axion models and little higgsino DM model etc. This dissertation studies Light Non-thermal DM model, described in Chapter 4 and the monojet search results are interpreted in terms of this model in Sections 8.3.2 and 8.3.3. Some of the non-thermal dark matter candidates are briefly discussed below.

- Axions

  Axions are hypothetical particles emerged to resolve strong CP problem in QCD. One way to produce axion dark matter is through non-thermal coherent oscillations on the axion field near the QCD phase transition. Axions produced in such cases have zero momentum and low mass $m \sim 10~\mu eV$. It was believed that axion can only be warm or hot dark matter particles [55, 56] however recently it has been hypothesized that axion could also be a cold dark matter for very low reheating temperatures [57–59].

- Gravitinos

  Gravitino is the supersymmetric partner of the graviton in supersymmetric models. Supergravity predicts the gravitino, analog of W and Z bosons in electroweak theory, which may be the lightest supersymmetry particle and a natural DM candidate. Depending on supersymmetry breaking mechanism, the gravitino could be anywhere in the mass range from $\sim$ eV to TeV. Despite of their strong theoretical motivation, gravitinos are very hard to observe as they interact only gravitationally [60].

- Sterile Neutrinos

Sterile neutrinos are similar to SM neutrinos but they do not interact electroweakly. Since mass eigenstates are different from the electroweak ones therefore sterile neutrinos may mix with electroweak, or active, neutrinos. As dark matter, sterile neutrinos may be produced in the early Universe in many ways. Depending on their production mechanism, sterile neutrinos can be constrained by their effects on smaller-scale structure in the Universe [61, 62].

There is a huge list of other dark matter candidates including dark matter from little Higgs models [63, 64], superheavy dark matter (Wimpzillas), mirror particles [65–68], CHarged Massive Particles (CHAMPs) [69], self interacting dark matter [70, 71], D-matter [72], brane world dark matter [73], crypton [74], superweakly interacting dark matter [60] and many more.

1.3.3 Detection Techniques

Three main techniques are carried out to exploit the interaction between dark matter and SM as shown in Figure 1.7. The detection strategies depend on the type and couplings of this interaction. All the three strategies compliment each other as they try to solve the same problem but with different methods. In this section I will briefly go through these astroparticle techniques.

- Direct Detection

  Direct detection is one of the most promising technique in dark matter search. It is based on the idea that if galaxy is full of WIMPs then these galactic WIMPs should pass through earth too and interact with matter (nuclei) in the lab while depositing energy to a single nucleus [75–77]. Direct detection signal is calculated on basis of several ingredients like velocity and density of galactic WIMPs in the solar neighborhood as well as the cross section of WIMP-nucleon scattering. Such type of information can provide the foundation for expected event rate calculation in direct detection experiment. The rate is given as:
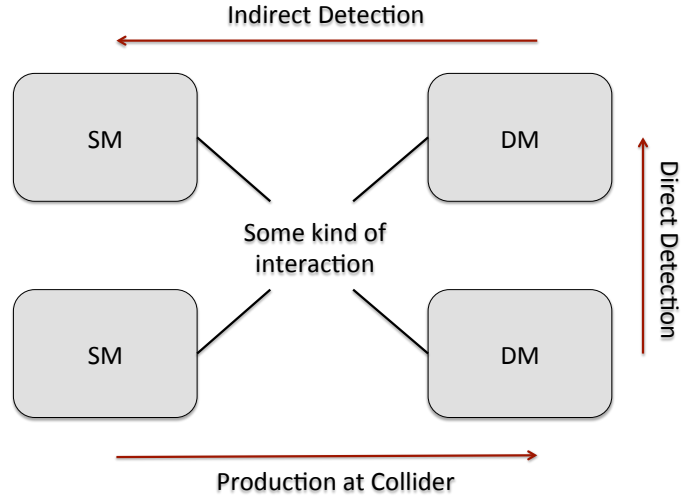
Figure 1.5: Different dark matter detection strategies are explained in a toy Feynman diagram.

$$R \approx \sum_i N_i n_\chi < \sigma_{i\chi} > \tag{1.6}$$

where summation is over nuclei species in the detector and N_i is the number of target nuclei in the detector given by:

$$N_i = \frac{\text{Mass of detector}}{\text{Atomic mass of nuclei species i}} \tag{1.7}$$

n_χ represents local WIMP density whereas WIMP-nuclei scattering cross section is given by σ_χ [78].

The types of scattering are divided into elastic or inelastic and spin-dependent or spin-independent. There are a number of direct detection experiments which are either working or are recently in development. These experiments make use of several detection techniques to measure the recoil of nucleus as a result of dark matter scattering.

These techniques include observation of photon (in experiments CREST and CUORI-CINO), scintillation (in experiments DAMA [79], ZEPLIN-I LIBRA and NAIAD) and ionization (in experiments HDMS, GENIUS, MAJORANA, DRIFT and IGEX). Multiple techniques are also used in some experiments e.g. both ionization and photon techniques are carried out in CDMS [80] and EDELWEISS [81] experiments, XENON, ZEPLIN-II, ZEPLIN-III and ZEPLIN-MAX make use of scintillation and ionization techniques whereas scintillation and photon techniques are incorporated in CRESST-II and ROSEBUD.

So far Large Underground Xenon (LUX) detector provides the best lower cross section limits for spin-dependent and spin-independent neutron interactions. LUX facility includes huge time-projection chamber filled with scintillation liquid xenon (368 kg) which is surrounded by highly sensitive light detectors and shielded by a large tank of water [82].

- Indirect Detection

Indirect DM searches are performed to observe the radiation produced in dark matter self-annihilations. The radiation flux is directly proportional to the dark matter annihilation rate and hence depends on dark matter density. Therefore the regions where dark matter densities are significant are natural places to search for large radiation fluxes. One of the excellent choice for gamma ray or neutrino detection might be dense regions of the galactic halos e.g. galactic center. There is also possibility that Sun or earth have captured dark matter particles in their interior while they lose their kinetic energy via scattering with nucleons and hence these astrophysical objects could serve as dark matter annihilation regions. Galaxy clusters, the Milky Way halo, Milky Way dwarf galaxies, the diffuse gamma-ray background and possible nearby dark-matter subhalos are included in deak matter dense objects [83–86]. Dark matter annihilation could result into variety of SM particles e.g. charged and neutral. How-

ever annihilation products which are charged particles, make it very difficult to locate point sources of such radiation as they move under effect of magnetic field. On the other hand gamma rays and neutrino are easier to interpret as they point directly back to their sources.

Neutrino-telescope observations of Sun and gamma-ray observations of the Milky Way halo and of the dwarf galaxies therein provide interesting constraints on dark matter mass [87–89].

Best upper limits on dark matter annihilation to high energy muons within Sun is provided by IceCube detector and reported as 103 muons/km^2/year [90] whereas SuperKamiokande telescope set the best upper limits for softer muons as 1500 muons/km^2/year [91].

- Production at Collider

  It is not possible to observe dark matter directly in collider experiments, rather it is the large missing transverse energy (MET) accompanying a SM jet, which provides signature for their existence.
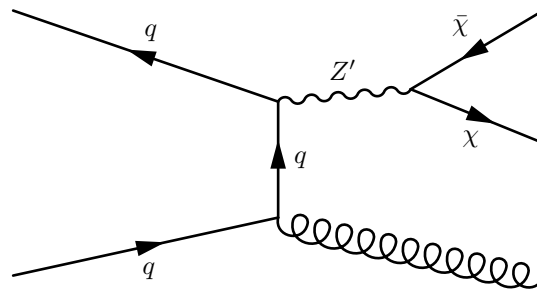
Figure 1.6: Feynman diagram for monojet category in a simplified model where a mediator (Z') couples to dark matter.

The strategy is to cautiously measure the transverse momentum of all particles generated in an interaction and look for any imbalance in momentum. Since total transverse momentum before the collision is almost zero therefore according to law of conser-

vation of momentum, after the collision, vector sum of transverse momenta of all the particles should also be negligible. Resolution and geometry of sub-detectors play a crucial role in accuracy of these calculations.
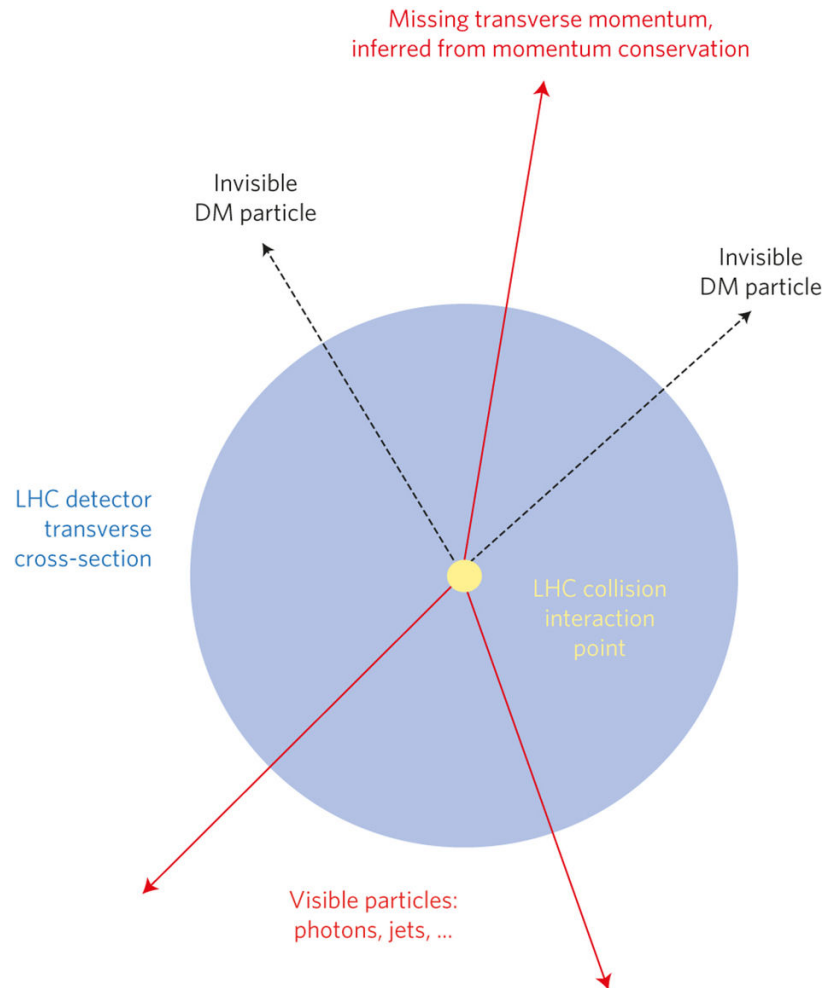
Figure 1.7: Schematic diagram showing missing transverse energy against recoil of visible SM particles in collider [92].

Very common collider dark matter searches are accumulated as mono-X where X refers to SM particle produced as a result of collision. Several mono-X signatures are studied where X is a quark or gluon jet [93, 94], lepton [95, 96] or photon [97–99]. Mono-Z/W [100, 101], mono-top, mono-bottom [102–104] and mono-higgs [105,

106] are also part of such analyses.

It is important to keep in mind that collider searches are different from the traditional dark matter searches as dark matter is created in the collider and is not from the cosmic origins and hence may not be stable on cosmological time scales [107].

CHAPTER 2
EXPERIMENTAL APPARATUS

The main goal of experimental high energy physics is to understand the origin of elec-troweak symmetry breaking and to explore physics beyond the standard model. This led the particle physicists to devise the most powerful possible apparatus, which can help to comprehend the fundamental forces and particles of the universe at the smallest scales of length. The world wide physicists' and engineers' efforts were combined to build the biggest particle accelerator ever i.e. the Large Hadron Collider (LHC), which consists of several particle detectors. This experimental facility is located at European Organization for Nu-clear Research (CERN) near Geneva, Switzerland. The data analyzed in this dissertation is collected at Compact Muon Solenoid (CMS) detector at the LHC, in proton-proton collision experiment in 2016, at center of mass energy 13 TeV with total integrated luminosity 35.9 fb^{-1}. This chapter includes an overview of the experimental apparatus.

2.1 The Large Hadron Collider

LHC is the world's largest and most powerful tool for particle physics research. Figure 2.1 shows a schematic layout of the LHC facility. This machine was installed in the existing 17 miles circumference tunnel that was constructed between 1984 and 1989 for the CERN Large Electron Proton (LEP) collider. The LEP tunnel is located 45-170 meters beneath the Franco-Swiss border and consists of eight straight sections and eight arcs. There are two 2.5 km long transfer tunnels built to connect LHC facility to other parts of CERN. The longer arc sections contain 1232 superconducting dipole twin bore magnets around the ring to keep the particle beams in a circular path. Each section is cooled by a system of Niobium-Titanium Rutherford cables at a super-conductive temperature of 2 K. LHC uses more than 8000 other higher-order multipole and corrector magnets to stabilize and focus the proton beams. A large electric field is used to remove electrons from the Hydrogen, leaving only the protons.

Resulting proton bunches are accelerated in Radio-Frequency (RF) cavities, which produce electromagnetic fields to increase proton's energy at each turn in the accelerator ring until they gain speed almost equal to that of light. The energy of the protons increase until its velocities reaches very close to the speed of light. At this point proton beams are split in 2808 bunches of protons per beam, with about 10^{11} protons per bunch. Once stable beams are acquired, they are squeezed and collided at the four collision points where the particle detectors are placed. The proton bunches in each beam are collided every 25 ns and several proton-proton collisions happen during each bunch crossing. Performance of the collider is characterized by a parameter known as instantaneous luminosity L and is given as a function of the rate of event production.

$$L = \frac{N_e}{\sigma} = \frac{kN^2f}{4\pi\sigma_x^*\sigma_y^*} \tag{2.1}$$

Where N_e is the event rate, σ is the process cross section, k is number of bunches, N is number of protons per bunches, f is the beam revolution frequency (11.25 kHz) and σ_x^* and σ_y^* are horizontal and vertical beam sizes at collision points, 16 μm each. Beam intensity reduces over time and hence the luminosity, with a life time of $\tau \approx 15$ hours. It is therefore required to dump and refill the beam periodically about every 7 hours. The integrated luminosity is calculated as the integral of luminosity as a function of time and directly relates to the number of collisions in a given time period.

$$L = \int \mathcal{L}(t) \, dt \tag{2.2}$$

where $\mathcal{L}(t) = L_0/(1 + t/\tau)^2$ with L_0 as initial luminosity.

CERN accelerator complex is made up of a number of linear and circular accelerators which are linked together and are used to enhance proton's energy before they are injected in the LHC ring. These accelerators are Linac2 (ramp energy up to 50 MeV), the Proton Synchrotron Booster (PSB) (protons from Linac are accelerated here to about 91.6% of
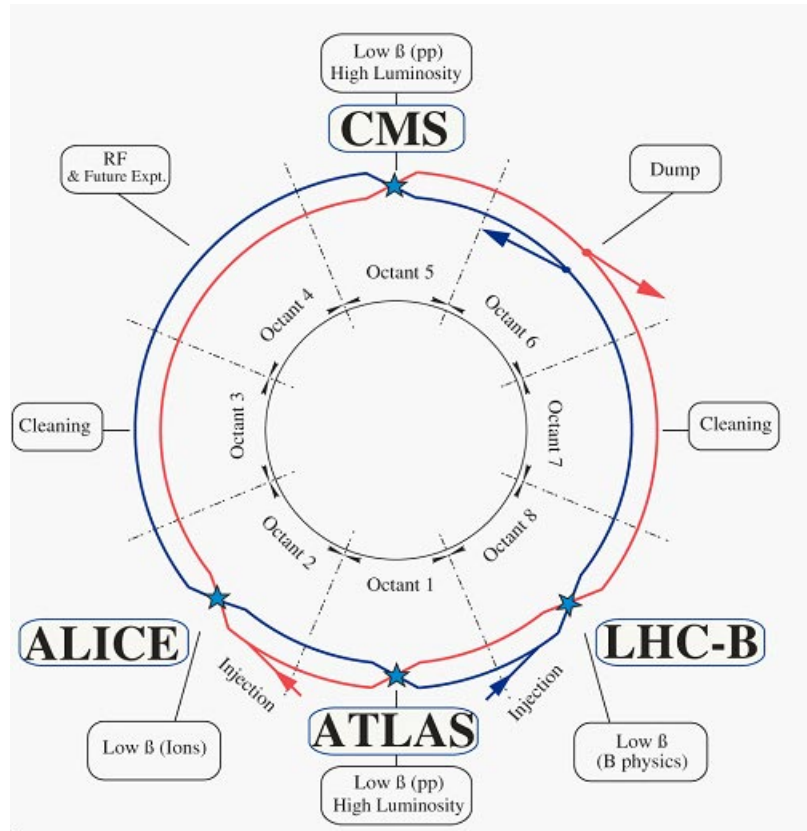
Figure 2.1: Figure shows schematic layout of LHC collider [108].

c), the Proton Synchrotron (PS)(protons energy reaches to 26 GeV), and the Super Proton Synchrotron (SPS) (proton beams acquire 450 GeV energy each).

LHC has seven versatile experiments which use detectors to analyze the huge amount of collision data. ATLAS and CMS are the main experiments which use general purpose detectors to search new physics and are installed at point 1 and 5 respectively. Another experiment named ALICE is built at point 2 which studies heavy lead ion collisions. The purpose of such studies is to search for quark gluon plasma which is believed to exist in first few micro-seconds of the early universe after the Big Bang. b-physics is explored exclusively at LHCb experiment (situated at point 8) whose goal is to understand the matter-antimatter asymmetry of the Universe.
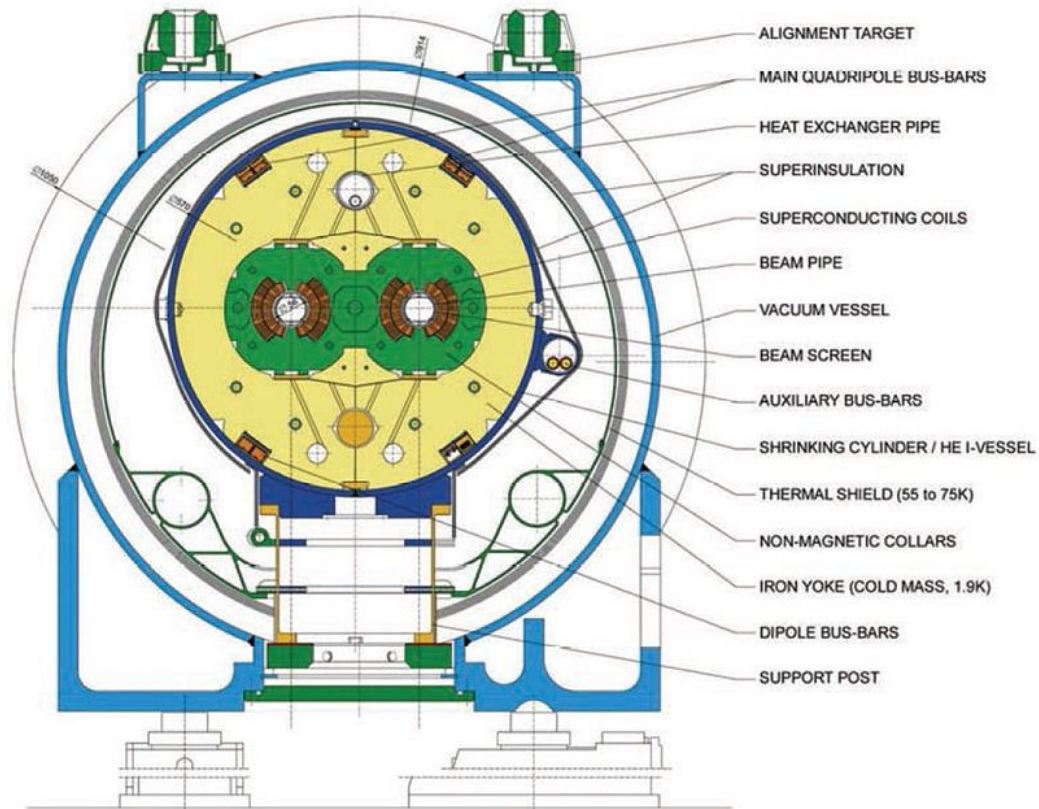
Figure 2.2: Cross section of the two-in-one magnetic design for main LHC dipole magnets [108].

LHC's construction was completed in 2008 and first beams were observed on September 2008 in an inaugural commissioning run. It is designed to collide proton beams with a centre-of-mass energy of 14 TeV and very high luminosity of 10^{34} cm^{-2}s^{-1}. During Run 1 (March 2010 to February 2013), LHC recorded proton beams collision at center of mass energy $\sqrt{s}$ =7-8 TeV followed by the Long Shutdown 1 (February 2013 to April 2015), when LHC went through upgrades and eventually collisions were recorded at $\sqrt{s}$ =13 TeV in Run2 era (from April 2015 through 2016) as shown in Figure 2.3 [108–110].
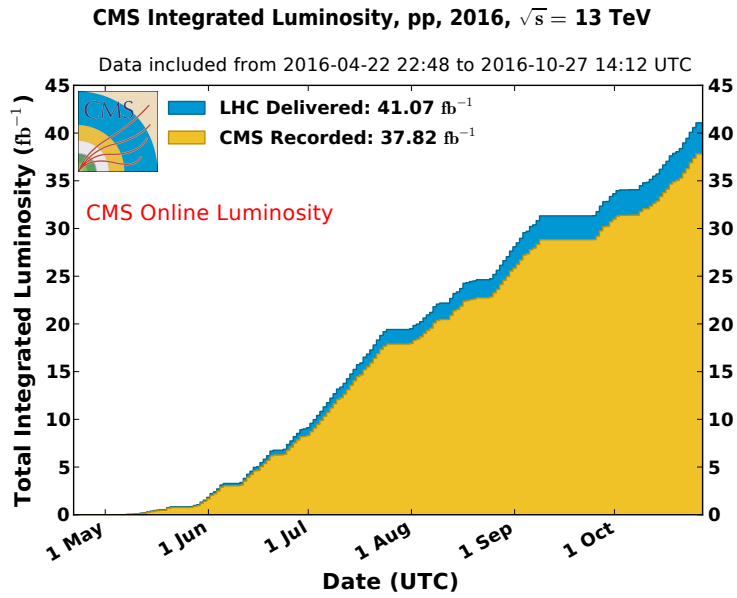
Figure 2.3: Total integrated luminosity delivered to and recorded by CMS during proton-proton stable beams collisions at $\sqrt{s}$ =13 TeV in 2016 [118].
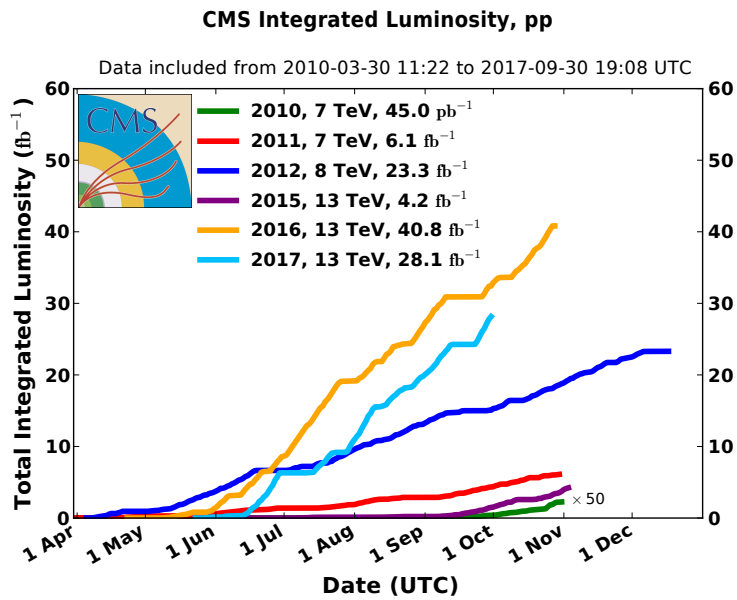
Figure 2.4: Comparison between total integrated luminosity delivered to CMS during proton-proton stable beams collisions in different spans of LHC operation [118].

2.2 The CMS Detector

Compact Muon Solenoid (CMS) is one of the two general purpose detector at LHC which is designed to search for new physics at TeV energy scale (Figure 2.5) . It's goal is to record enormous rate of collisions from the proton beams, about 100 m below ground at Point 5 of the LHC, near Cessy, France. CMS is capable of detecting a variety of new physics signatures. One of the goal was to confirm (or disprove) the existence of last SM particle i.e. Higgs boson. This goal was achieved with the discovery of Higgs boson during Run 1 operation of LHC. This discovery motivated the particle physicists to explore beyond the SM, like existence of dark matter or SUSY, which is the ultimate goal of the Run 2. CMS and ATLAS experiments compliment each other but they differ in design. The outstanding features of CMS are high magnetic field solenoid, a full-silicon-based inner tracking system, crystal scintillator electromagnetic calorimeter and sampling calorimeter for hadrons. This fascinating machine is cylindrical in shape with an overall length of 21.6 m and built around a huge solenoid magnet. It is designed to be symmetric around the 14.6 m diameter beam pipe and weighs 14000 tonnes. The sub-detector systems of CMS are arranged in layers around the interaction region.

Barrel and end cap are the two main regions with the standard coordinate x-axis pointing towards center of LHC, the y-axis pointing upward, and the beam direction is along z-axis. In polar coordinates system r and ϕ represent distance from the beam and azimuthal angle respectively, which are measured in x-y plane whereas polar angle θ is calculated from the z-axis. Pseudorapidity is calculated as a function of θ and is quite handy in coordinate measurement for highly relativistic particles, given as $\eta = -\ln \tan(\theta/2)$. Transverse momentum and energy of the beam are calculated from the x and y components whereas imbalance in momentum is inferred as missing transverse energy e.g.

$$\not{E}_T = -\sum_i p_T^i$$
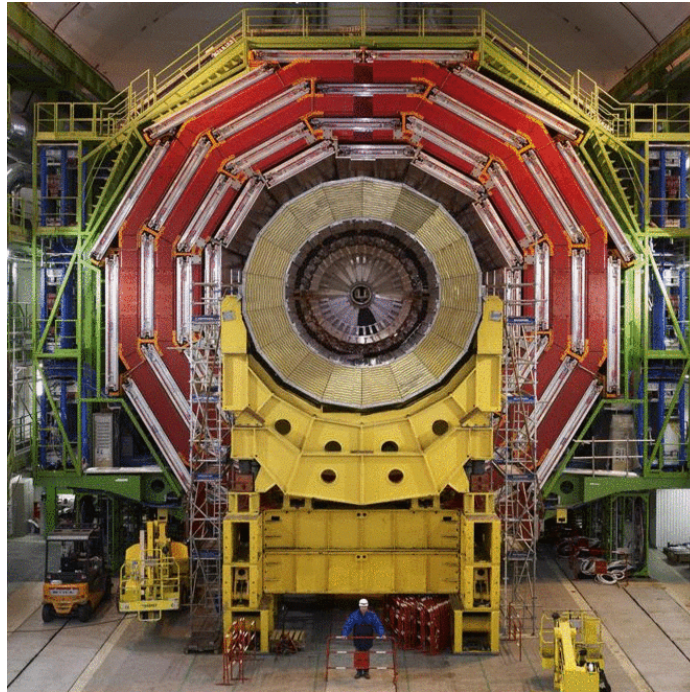
Figure 2.5: The Compact Muon Solenoid (CMS) detector at the Large Hadron Collider, with human figure for scale [119].

Inner most part of the detector is a silicon tracker that surrounds the beam interaction point and measures the position of charged particles in terms of x,y coordinates. CMS coordinate system is shown in Figure 2.7. The full tracking system includes ten layers of silicon microstrip detectors and three layers of silicon pixel detectors. The electromagnetic and hadron calorimeters are sandwiched between the solenoid magnet and the silicon tracker. The ECAL barrel part makes use of avalanche photodiodes whereas end cap region is occupied with vacuum photodiodes. This setup helps to read out scintillation light generated by electromagnetic particle interactions in the lead tungstate crystals. HCAL sits at the outer side of ECAL with hybrid photodetectors in the barrel to detect scintillation light from hadronic interactions with the brass and scintillator detector material. The scintillation light is then transferred to the photodetectors with the help of clear fibers. Outside the solenoid magnet, there is a muon system comprised of four stations embedded in the iron yoke of

Silicon Tracker

Electromagnetic Calorimeter

Hadron Calorimeter

Superconducting Solenoid

Iron return yoke interspersed with muon chambers

———— **Muon**   ———— **Electron**   ———— **Charged hadron (e.g. pion)**

– – – · **Neutral hadron (e.g. neutron)**   – – – – **Photon**
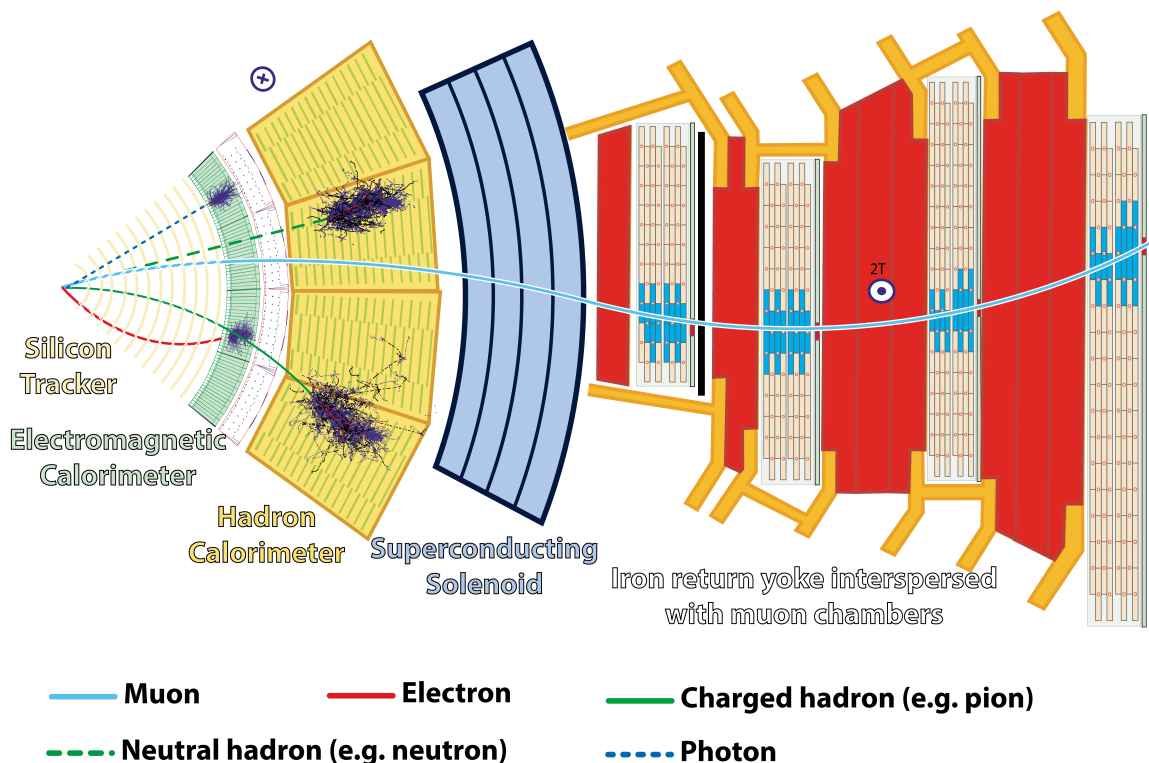
Figure 2.6: Schematic cross section of CMS detector [120].

the magnet. Each muon station includes sub-detectors such as aluminum drift tubes (DT) in the barrel region and cathode strip chambers (CSC) in the endcap region, complemented by resistive plate chambers (RPC) [111]. Figure 2.6 shows a schematic cross section of all sub-detectors.

2.2.1   Solenoid

The CMS magnet is a superconducting solenoid with a magnetic field of 3.8 T which is 100,000 times stronger than the Earth's magnetic field. 13 m long and 6 m in diameter, this gigantic magnet helps to determine the charge -to-mass ratio of high energy charged particles from the curved path they follow in the magnetic field. The total current for 3.8 T is 18,160 A corresponding to stored energy of 2.3 GJ. The magnet is made up of super-conducting niobium-titanium (NbTi) coils in 4 layer winding, which is refrigerated at very

low temperature of 4.5 K. The tracking system along with calorimeters are surrounded by the magnet while the muon system lies outside of it. The magnet is enormously strong and shapes up the experimental structure of CMS.

2.2.2 CMS Tracking System

In order to understand the high energy collisions, it is very crucial to measure the particle's momentum with a great precision, CMS tracker with 205 m^2 of silicon sensors has been designed to fulfill this task. The driving principle is that particle's path would be effected in presence of a magnetic field i.e. more curvature corresponds to lower momentum. The particles are tracked by recording their position in x-y coordinates at the chosen measurement points. The tracker can accurately reconstruct trajectories of several high energy particles like muons, electrons and hadrons. It also keeps track of particles arising from secondary vertices such as b-quarks. Each measurement of the tracking system is accurate to 10 μm which is equivalent to a fraction of human hair width.
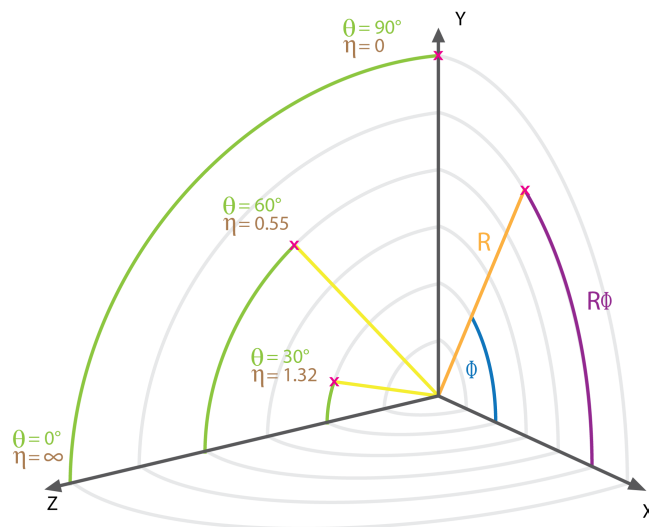
Figure 2.7: Figure shows (η, ϕ) coordinates which are used to track particles inside CMS detector [121].

The CMS tracking system sits at the core of the detector, surrounding the IP and is entirely

silicon based. Cylindrical in shape, the detector is 5.8 m long with a diameter of 2.5 m and encompasses pseudorapidity $|\eta| < 2.5$. Since it is the inner most part of the detector therefore it receives severe radiation doses, roughly 0.18 to 84 Mrad for every 500 fb^{-1} of data. In order to minimize such radiation damages, it is required to select the construction material very cautiously and also the operating temperature is set to -10 °C.
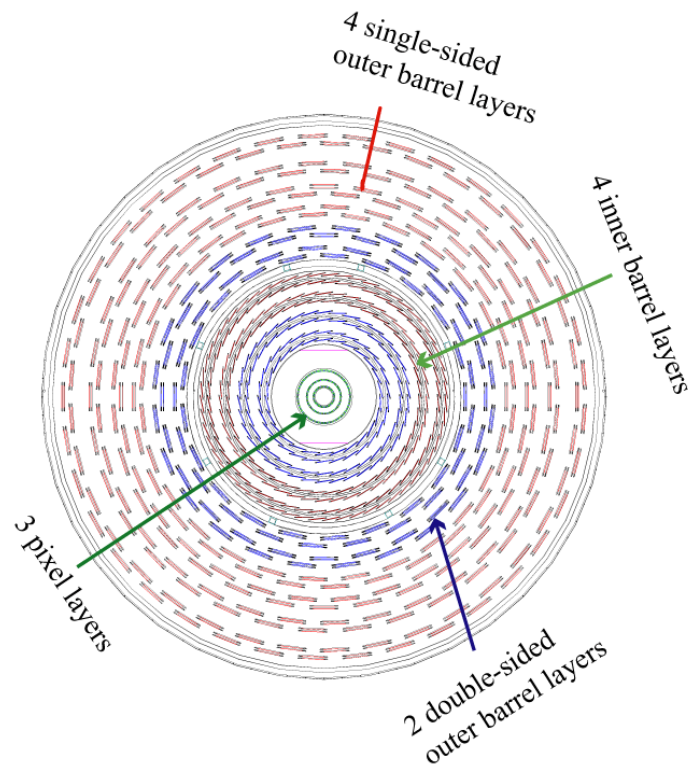
Figure 2.8: Silicon Pixel detector layers are shown in the plane perpendicular to the beam direction [122].

The tracker has two parts, inner pixel detector and outer strip detector with 13 layers in the central region and 14 in the endcaps (Figure 2.9). Starting from the center, first 3 barrel layers (48 million pixels) along with two endcap disks (18 million pixels) make up the pixel detector. Strip detector is comprised of next four layers (10 cm × 180 μm silicon strips) followed by six outer layers (25 cm × 180 μm silicon strips) which makes the total of 9.6 million strip channels.
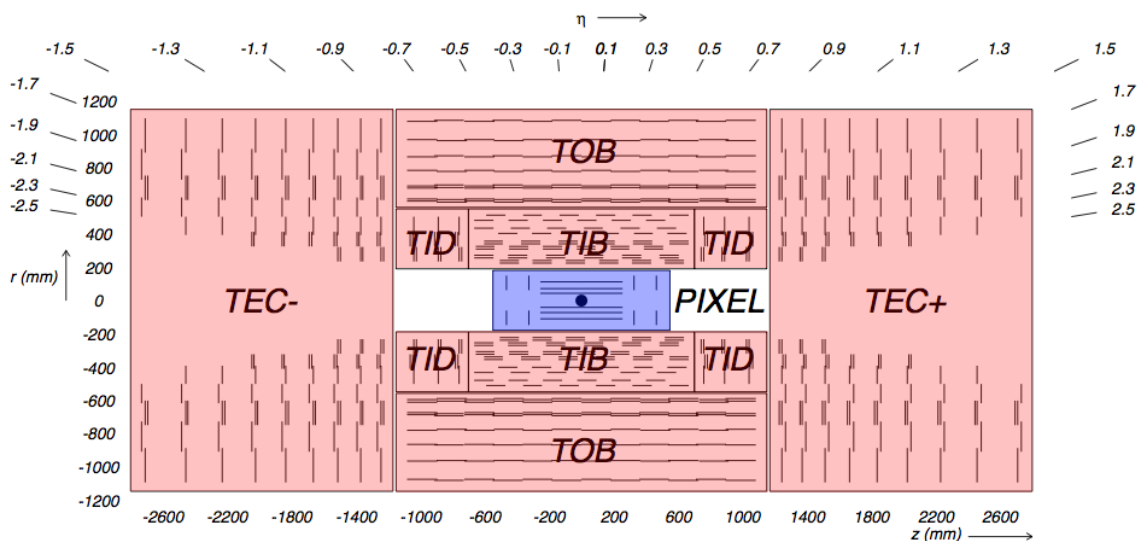
Figure 2.9: Several detectors in the silicon tracker. Silicon pixel detector is shown in blue whereas silicon strip detectors i.e. TIB, TID, TOB and TEC, are shown in red [123].

2.2.3 Electromagnetic Calorimeter

Outside of the tracking system, ECAL (Figure 2.10) is a cylindrical shape calorimeter, constructed from 76,832 lead tungstate $PbWO_4$ crystals. ECAL barrel (EB) region contains 61,200 of such modules with a pseudorapidity coverage of $|\eta| < 1.479$, while each ECAL end cap (EE) consists of 7,324 modules, covering $1.479 < |\eta| < 3$. The purpose of ECAL is to collect energies of electrons and photons and lead tungstate which is extremely dense and transparent material, helps efficiently to accomplish this goal.

The high resolution of electromagnetic objects requires a very fine granularity which is ensured by ECAL's significant features like short radiation length (0.89 cm), high density (8.28 g/cm^3) and a small Moliere radius (2.2 cm). EB and two D-electrodes on each EE are designed by combining variety of supercrystal geometries. Distance of front faces of EB crystals is about 1.29 m from the interaction point, with a size of 22 mm $\times$ 22 mm. EB further extends to an outer radius of 1.77 m. The end caps are separated from IP at $z = \pm 315.4$ cm. The pyramidal shaped lead crystals are polished on all sides to enhance internal reflection. In front of each endcap there are pre-shower detectors which are com-
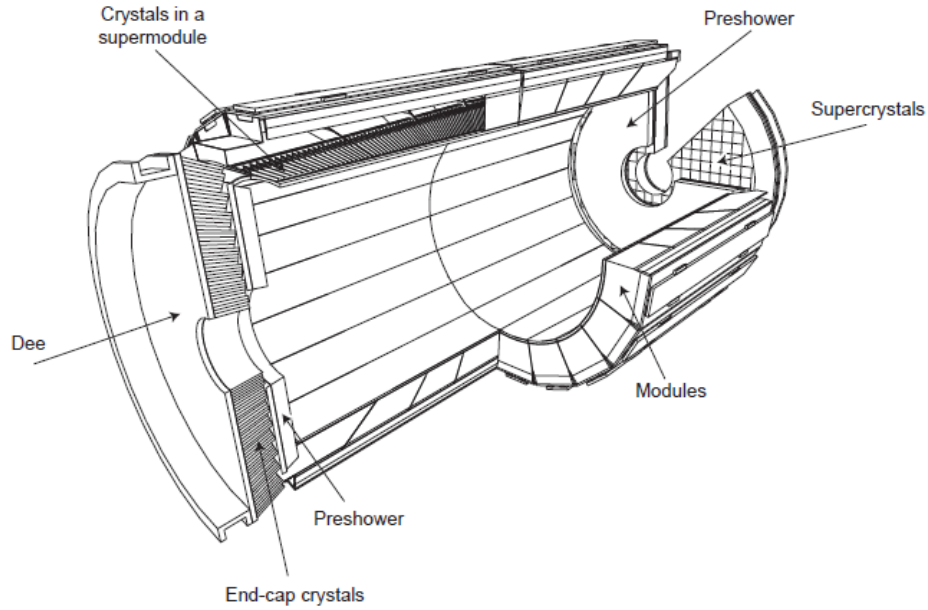
Figure 2.10: Schematics of CMS Electromagnetic Calorimeter (ECAL) [124].

posed of lead absorber and silicon detectors. The features of such detectors are: to identify showers from minimum ionizing particles, detect and veto neutral pion production as well as enhancing the position resolution of the ECAL [112]. Figure 2.11 and 2.12 show ECAL crystals in endcap and barrel regions respectively. Energy resolution of ECAL is calculated as a sum of three terms as follows:

$$\frac{\sigma}{E} = \frac{a}{\sqrt{E}} \oplus \frac{b}{E} \oplus c \tag{2.3}$$

Where a is Stochastic term representing fluctuations in the signal generation process, b is noise term which arise due to readout electronics and last term c is a constant, which comes from detector's nonuniform response, fluctuation in longitudinal energy containment and also energy lost in dead material.
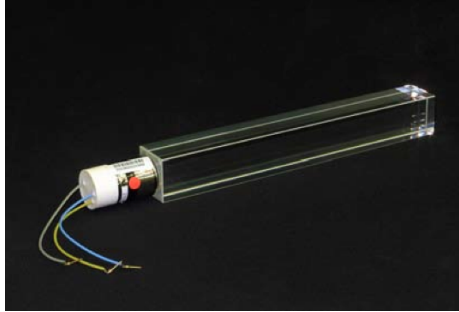
Figure 2.11: Lead Tungstate PbWO^4 crystal with its avalanche photodiode photodetector used in ECAL barrel region is shown [123].
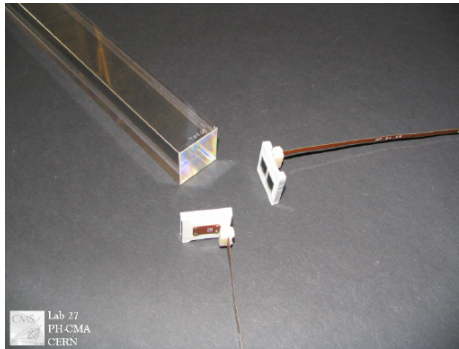
Figure 2.12: Lead Tungstate PbWO^4 crystal attached to photomultiplier used in ECAL barrel region is shown [124].

2.2.4 Hadronic Calorimeter

The next outer component of the CMS detector is hadronic calorimeter, primarily designed to measure the energy and direction of hadronic jets i.e. shower of composite particles of quarks and gluons, while they interact with the detector material. Another important feature of HCAL is its contribution in measurement of missing transverse energy which could provide signature for new physics such as existence of dark matter etc. Collective information from HCAL, ECAL and muon system helps in determining the physical objects like photons, electrons and muons.

This subsystem lies between 1.77 m to 2.95 m from the beam line with an $|\eta|$ coverage of 5.2. It is a sampling calorimeter with layers of absorber and scintillator material. Absorber

material is used to produce cascade of particles from incident hadrons, corresponding energy is deposited and read out from the active scintillator layers.
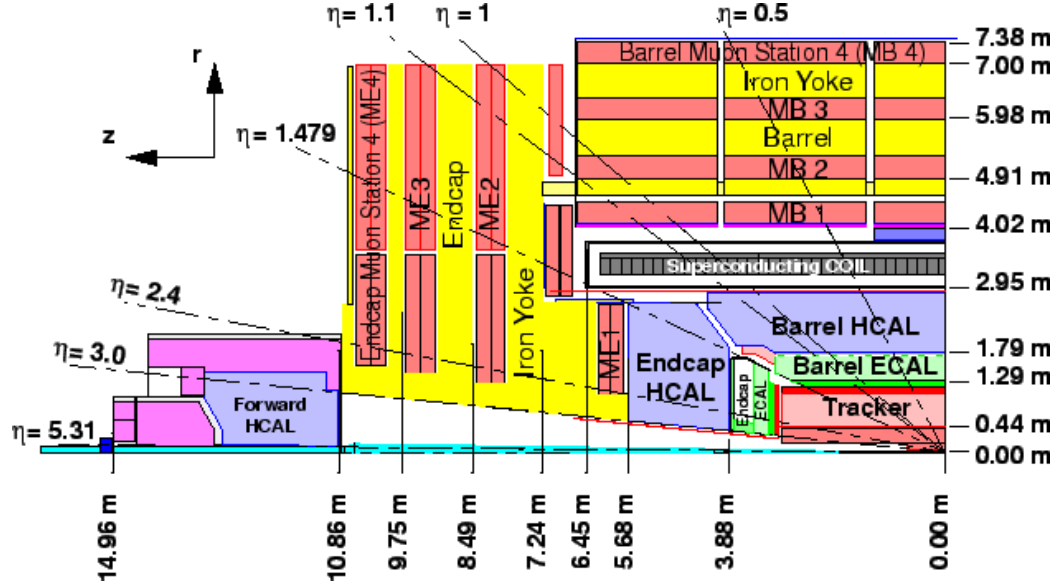
Figure 2.13: Several HCAL regions are shown in longitudinal view of one CMS quadrant [125].

HCAL is organized into four sections: barrel, endcap and forward. HCAL barrel (HB) region covers $|\eta| < 1.3$, whereas the HCAL end caps (HE) covers $1.3 < |\eta| < 3$ and and the HCAL forward (HF) calorimeter covers large pseudorapidity range $|\eta| < 5.2$. The HCAL outer (HO) calorimeter lies outside of the solenoid and absorbs the excessive energy. The granularity of HB, HE and HO tiles is given in terms of (η, ϕ) coordinates as $\Delta\eta \times \Delta\phi =$ 0.087×0.087.

The HB region includes two half-barrels with total 36 identical wedges, each individual wedge weighs 26 tonnes. The scintillating material is organized in form of trays while each scintillator layer contains 108 trays and each wedge is made up of 17 such layers. Thick brass plates are used as separator between the scintillator layers including eight 50.5 mm thick and six 56.5 mm thick plates. Similar to HB, HE disks are designed with 36 identical wedges, containing a total of 1,368 trays of 20,916 trapezoidal shaped scintillator tiles. The

depth of HB is not sufficient enough to manage the whole bulk of particle shower on its own therefore the HO had been included as an extension to measure the energy that is leaked by the barrel and also the late starting shower. The HO is comprised of five ring shaped regions where the magnetic field is returned through an iron yolk. These rings are assigned numbers -2, -1, 0, +1, +2, corresponding to increasing value of z. The interaction length is smaller at the central ring therefore two HO scintillating layers had been placed on either side of the tail catcher iron of thickness 19.5 cm. The other HO rings consists of single scintillating layer.

HF calorimeter is made of iron and quartz fibers and placed 11.2 m away from the IP. Since it covers large range of pseudorapidity thus plays an important role in jet detection and $\not{E}_T$ resolution, which could help in exploring physics searches such as top and Higgs production as well as supersymmetry particles. HF barrel region contains 18 identical wedges, 48 PhotoMultiplier Tubes (PMT) per wedge, with layers of steel plates, each 5mm thick. HF bears high particle flux therefore it requires radiation resistive material and also regular checking of radiation damages. This purpose is served by Cherenkov-light emitting quartz fibers (diameter of 800 μm), embedded in dense steel absorber of thickness 165 cm. Fibers are divided in two type: long, which run through full length of the absorber and short which start at the depth of 22 cm from the front of HF barrel. This design helps in recognizing electromagnetic and hadronic showers as electromagnetic shower loses almost all of its energy in first 22 cm whereas hadronic shower deposits energy throughout the material. The fibers are bundled together to form 13 towers with a granularity of $\Delta\eta \times \Delta\phi =0.175\times$0.175. Figure 2.13 represents different HCAL regions in a cross sectional view of one of the CMS quadrant.

2.2.5   The Muon System

As it is perceived by its name, detecting muons is one of the major task of Compact Muon Solenoid detector. Since muons acquire large penetration power as compared to other

charged particles, they pass through the material almost without any radiative loss, therefore the CMS muon system is positioned at the outermost edge of the experiment. It consists of end caps regions and a barrel region which is divided into four stations. Muon identification and reconstruction of momenta is carried out by three types of gas ionization detectors: drift tubes (DT), cathode strip chamber (CSC) and resistive plate chambers (RPC) (Figure 2.14).
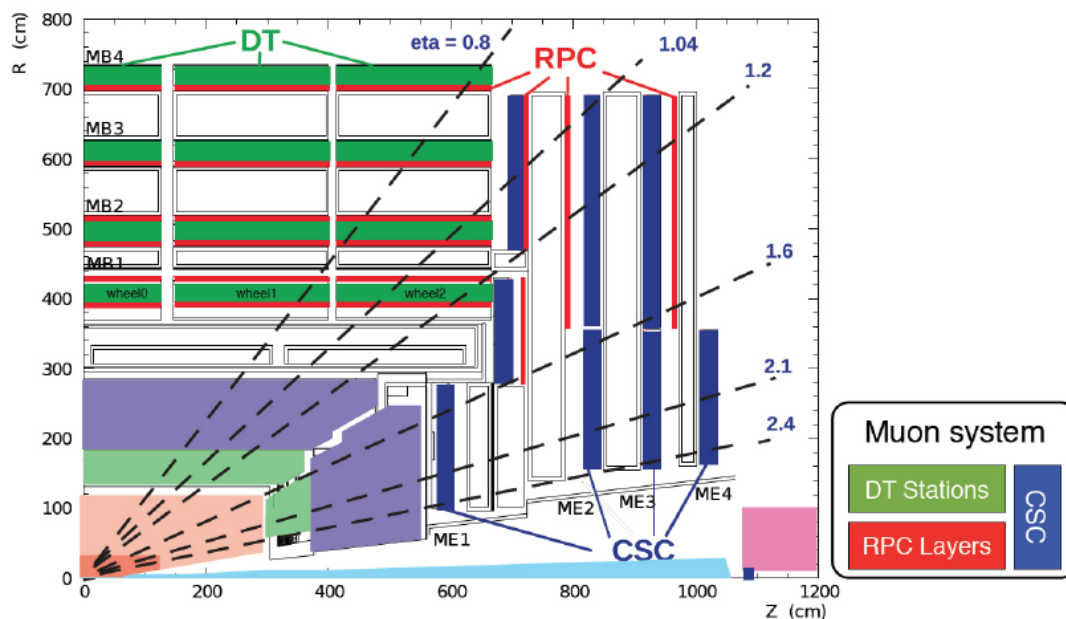
Figure 2.14: Schematic layout of one CMS quadrent. Green parts represent four DT stations in the barrel (MB1-MB4), the four CSC stations in the endcap (ME1-ME4) are shown in blue and the RPC stations are in red [126].

The DT system is made up of drift cells (Figure 2.15), with dimensions of 13 mm × 42 mm each, employed to measure muon positions in barrel region. Every single tube is about 4 cm wide and filled with a mixture of Argon and Carbon dioxide gases. Each of the DT chamber is made up of 12 aluminum layers which are organized in three groups of four, each group contains about 60 tubes. The overall size of a DT chamber is about 2 m × 2.5 m. Whenever a charged particle passes through the gas volume, it ionizes the gas, while electron moves towards an inner anode and the information where it hit the wire as

well as the charged particle's original distance from the wire allow DT to provide particle's coordinates.
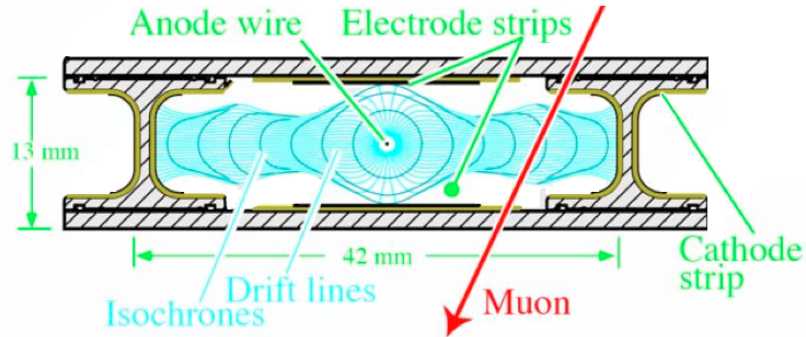
Figure 2.15: Schematics of a DT cell [124].

The CSC is deployed in the endcap disks, contains 468 trapezoidal modules, covering $0.9 < |\eta| < 2.4$, consists of six azimuthal positively charged anode wires crossed with seven radial negatively charged copper cathode strips in the gas. Similar to DT case, the muon hits the gas atoms, releases an electron which moves towards anode while positive ion flocks to the copper cathode. Both anodes and cathodes are perpendicular to each other and hence for each passing particle we get two position coordinates with 80 μm resolution.

Finally RPC are fast gaseous detectors, placed in both barrel and end cap regions. It consists of 480 rectangular shaped barrel chambers, made up of 68136 strips with a total area of 2285 m^2. In addition, end cap regions are comprised of 432 trapezoidal chambers which contain total 41472 strips and corresponding area of 668 m^2.

2.3   The Data Acquisition and Trigger

LHC is able to deliver about 40×10^6 bunch collisions/second which means approximately 20 interactions for each bunch crossing with overall expected event rate of 10^9 Hz. It is impossible to incorporate this enormous amount of data therefore a trigger system consisting of a Level-1 Trigger (L1T) and a High-Level Trigger (HLT) is introduced to reduce

this huge interaction rate to a computationally manageable one(of the order of 100 kHz or so).
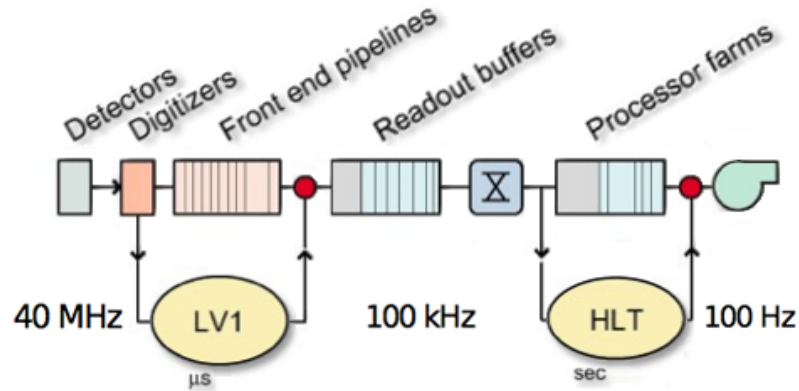
Figure 2.16: Data rates are shown at different stages between detectors and final data storage [127].

The Level 1 trigger accesses data from ECAL, HCAL and muon detectors and uses field programmable gate array (FPGA) technology to compile local trigger primitives. This technology identifies electrons and muons by using the pattern logic. Highest quality objects are sent to a single global trigger which then takes decision of keeping or killing the event. At L1T the event rate is reduced to 100 kHz, acceptance or rejection of the event decision takes place in 3.2 μs. Event must be selected very cautiously at L1T because once an event is rejected, it is lost for good.

After an event is accepted by the L1T (Figure 2.17), all the data flow is processed by data acquisition system (DAQ) which has two main subsystems: event builder and event filter. Event filter transfers the data to software based system HLT, which uses filtering and reconstruction algorithms to process events passing the L1T. HLT uses information from all of the sub-detectors to reconstruct physical objects like electrons, muons, photons, jets and missing transverse energy. Event data passing the HLT is stored in offline software system where is it processed before making available for physics analyses. The HLT decision time is about 300 ms and event rate is reduced to 100 Hz at this level (Figure 2.16).
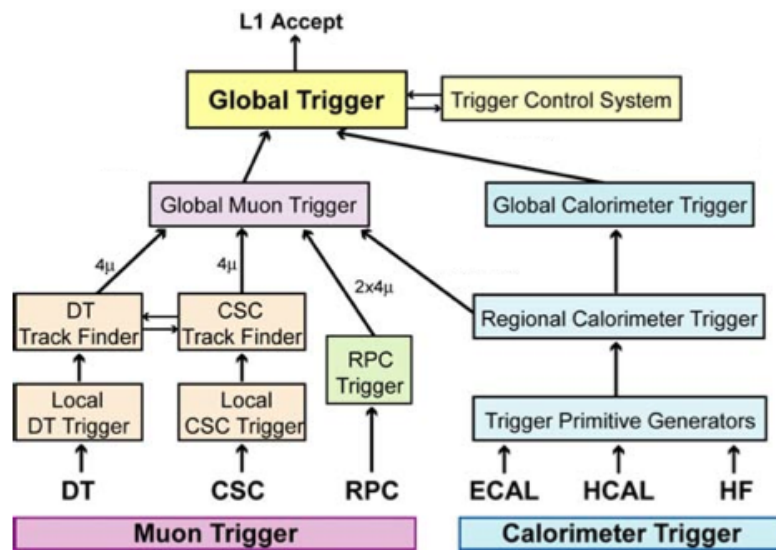
Figure 2.17: CMS triggers use information from sub-detectors. Figure shows L1T decision flow, if the event passes at this stage then data is transferred to DAQ system [124].

CHAPTER 3

EVENT RECONSTRUCTION AND SIMULATION

3.1   Particle Reconstruction

High energy particles' collisions result in production of many unstable, short lived particles which decay abruptly, without interacting with the detector material. Therefore only stable particles are reconstructed with Particle Flow (PF) algorithm e.g. electrons, muons, photons and hadrons. The information about jets and other interesting physics objects can be extracted by using stable PF objects.

Particles are identified and reconstructed on basis of their characteristics and subsequently information from different sub-detectors or collection of sub-detectors can be used. Tracking system, for example, efficiently records trajectories of charged particles, therefore provides a very good measurement of direction and momenta of such particles. On the other hand, combined information from ECAL and tracking system is used to reconstruct electrons. Since photons do not leave a track in the tracker therefore energy deposition in ECAL alone is used to reconstructs them. Muon reconstruction is done with the help of tracker and the muon system collectively. Information form HCAL and ECAL energy deposits assists in reconstruction of charged and neutral hadrons. Finally neutrinos or other particles which feebly interact with detector are identified by looking at the missing information i.e. missing transverse energy which is calculated as follows:

$$\not{E}_T = -\sum_i P_T^i \tag{3.1}$$

Where P_T^i is the transverse momentum of ith PF candidate.

Tracker plays a very important part in reconstruction of charged particles with its outstanding low transverse momentum resolution, therefore it is required to have a best tracking efficiency $\approx 100\%$. A high tracking efficiency ensures the reduction in fake reconstructed

energy. The goal is achieved by using an iterative algorithm which initially imposes tight selection criteria, resulting in negligible fake rate but lower efficiency, then implementing looser selections yields in throwing fake event but increasing the overall tracking efficiency.

Another important piece of information used by PF is known as calorimeter clusters, provided by ECAL and HCAL. Information form calorimeters' sub-detectors are used in calorimeter clustering algorithm, which performs several measurements such as reconstruction of electrons and charged hadrons, energy and direction of photons and neutral hadrons and distinguishing that energy deposition is from neutral or charged hadrons.

3.2   Monte Carlo event Generation

MC event generation technique is widely used in experimental and theoretical physics analyses. This technique is very useful in predicting collider experiments as well as it helps in development of background models to explore new physics processes. In collider experiments we look for new physics signatures, appearing as excess in data over the continuously falling background. These background processes are in fact SM processes that mimic new physics signal like events. The SM backgrounds can be modeled in two way i.e. by using events exclusively from simulation or by combining simulation and data driven techniques. After modeling the background, the next step is to apply correction scale factors to background events, these scale factors are measured using data and often referred as weights. The weights include perturbative QCD corrections, electroweak corrections, physics objects identification and reconstruction scale factors etc. SM simulations is carried out in two parts i.e. particle modeling based on collision event, without looking at particle's interaction with the detector and secondly, taking the detector's response in account while modeling particles' production in the collision.

CMS physicists use a variety of softwares to generate MC collision events and corresponding cross sections such as PYTHIA [113], MADGRAPH [114], Sherpa [115] and POWHEG [116]. Despite of difference in implementation, these softwares share the same

basic principles. From each colliding beam, only one of the proton's parton takes part in the scattering while carrying a fraction of proton's total energy, the corresponding momentum is calculated probabilistically by random sampling from the parton distribution functions (PDFs). Next step is hadronization process, where fragmentation and decays of initial particles are simulated to get the final stable particles.

3.3   GEANT Detector Simulation

In this part of MC event generation, the detector response is simulated. It includes the particle's interaction with the detector itself. The detector simulation is done with GEANT [117] software which includes complete digital representation of the CMS detector. This software package simulates each stable particle passing through the detector and at each step it determines particle's interaction with detector in a probabilistic approach. Features that are considered while simulating events are: particle's energy, material in which the particle is and the magnetic field. Since the detector is not ideal therefore it is not 100% efficient, it requires measuring the CMS calibrations and including them in simulations which will help in simulating detector's response accurately. After simulating the detector's final response, it is needed to correct any mismodeling of detector. For this purpose, scale factors calculated from real data are applied to MC.

CHAPTER 4

NON-THERMAL DARK MATTER MODEL

The light Non-thermal Dark Matter model is a minimal extension to Standard Model with $\sim$ TeV scalar color triplet(s) and a light fermionic DM candidate [128]. This is a viable and economical low-reheat temperature scenario for a late decaying moduli, that is well motivated in string models and offers an alternative of baryogenesis from a non-thermal point of view for the relic density. In this model baryon number is violated in interactions meditated by heavy scalars *X*, which explains the baryogenesis. The decay products of such mediators are non-thermal DM and as a result, relic density relates to the baryonic asymmetry. In this way Non-thermal dark matter model could explain the mini-coincidence puzzle, i.e., why the baryon and DM abundances are so similar.

In such models, light dark matter can be singly produced at the LHC as it is not parity protected [128]. This leads to the large missing transverse energy ($\not{E}_T$) and a associated energetic jet whose transverse momentum distribution is featured by a Jacobian-like shape, which exhibits peaks at half of the mediator mass *X*. New renormalizable baryon number violating interactions in Lagrangian ensure the successful baryogenesis and is given in equation 4.1.

$$L_{int} = \lambda_1^{\alpha,\rho\delta}\epsilon^{ijk}X_{\alpha,i}\bar{d}_{\rho,j}^c P_R d_{\delta,k} + \lambda_2^{\alpha,\rho}X_\alpha^*\bar{n}_{DM}P_R u_\rho + C.C. \tag{4.1}$$

Here $\bar{d}^c$ is the charge-congugate of the Dirac spinor. P_R is the right-handed projection operator. X_s are iso-single color triplet scalars with hypercharge $4/3$ and n_{DM} represents dark matter particle which is a SM singlet. The indices, $\rho, \delta = \{1, 2, 3\}$ are for the three quark generations, whereas $i, j = \{1, 2, 3\}$ are the $SU(3)$ color indices. Successful baryogenesis requires more than one new scalar [129], thus $\alpha = 1, 2$ represents a minimal case with two X mediators.

In these models, the emphasize is on single dark matter production in the decay of heavy colored mediator *X* and thus several production channels are investigated. These channels include monojet, dijet, paired dijet and 2jets+$\not{E}_T$ topologies.

4.1   Production Mechanism

4.1.1   Single-*X* channels

The monojet channel is a s-channel resonant process where *X* couples to two down type quarks (*d,s,b*) or one up type quark (*u,c*) and dark matter, as shown in Figure 4.1 (left). The transverse momentum of recoiled energetic jet peaks approximately at half of the resonance energy M_{X_1}.
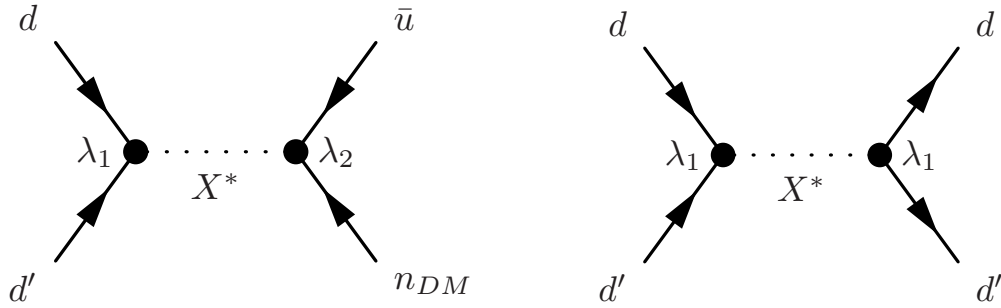
Figure 4.1:   s-channel resonant processes leading to monojet (left) and dijet (right) final states.

The PDF integrated total cross section is proportional to the square of coupling constants according to:

$$\sigma \propto \frac{|\lambda_1|^2 |\lambda_2|^2}{\Gamma_{X_1}} \tag{4.2}$$

where Γ_{X_1} is the decay width of *X*.

$$\Gamma_X = \frac{1}{8\pi M_X^2} \left[2|\lambda_1|^2 \sum_{i\neq j} |\overrightarrow{p}_{ij}| (M_X^2 - M_{d_i}^2 - M_{d_j}^2) + |\lambda_2|^2 \sum_i |\overrightarrow{p}_i| (M_X^2 - M_{u_i}^2 - M_{n_{DM}}^2) \right] \tag{4.3}$$

The u and d represent up and down type quarks respectively. The $\overrightarrow{p}_{ij}$ is the final state momentum and M_{d_i} and M_{d_j} are final state masses, where different quark generations are indicated by $\{i, j\} = 1, 2, 3$. Final state momentum is given as $\overrightarrow{p}_i$.

For heavy mediator $\sim$ TeV scale, the cross section depends on couplings mainly and is determined by the lesser between λ_1 and λ_2.

$$\sigma \propto \frac{|\lambda_1|^2 |\lambda_2|^2}{(2|\lambda_1|^2 + |\lambda_2|^2)} \tag{4.4}$$

The dijet channel is a s-channel process similar to the monojet channel but with two different down type quarks in the final state Figure 4.1 (right). Cross section for this channel depends only on λ_1 when $\lambda_1 >> \lambda_2$. Branching ratios of the channels are shown in Figure 4.2.

$$\sigma \propto \frac{|\lambda_1|^4}{(2|\lambda_1|^2 + |\lambda_2|^2)} \tag{4.5}$$

Multiple jets and missing transverse energy channel includes initial state gluon-splitting (ISGS) process, which contribute as single X channel and leads to 2 jets and missing transverse energy final states (Figure 4.3). This process has significant cross-section due to the fact that it includes valance d quark and gluon which are not PDF suppressed.
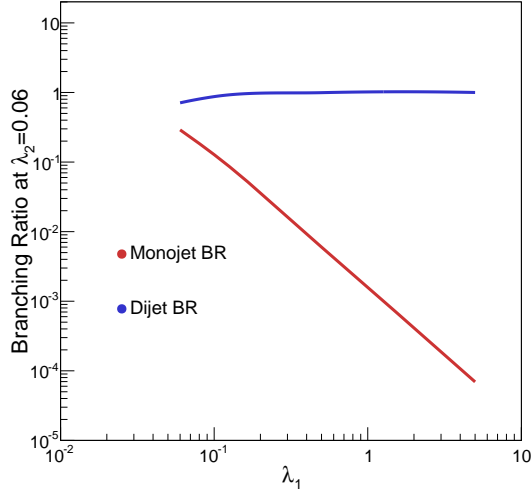
Figure 4.2: Branching ratio for monojet and dijet channels as a function of λ_1 with $M_{X_1} = 1.0$ TeV.
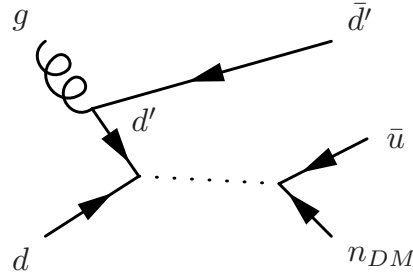
Figure 4.3: Initial state gluon splitting process (2 jets + $\not{E}_T$) .

4.1.2 *X* Pair Production

Both QCD and new physics vertices can contribute to two *X* channel as shown Figure 4.4. *X* pair-production is dominated by very light *t*-channel exchange particles which are shown is last two diagrams. The cross-section is proportional to $|\lambda_1|^4$ and $|\lambda_2|^4$ respectively. Each *X* can decay through the channels discussed in Section 4.1.1. Multiple jets and missing transverse energy arise if we consider both *X* decay through monojet channel (2 jets plus $\not{E}_T$) or one *X* decays through monojet and the other through dijet (three jets plus $\not{E}_T$ channel). We have included two jets plus $\not{E}_T$ channel in our analysis.
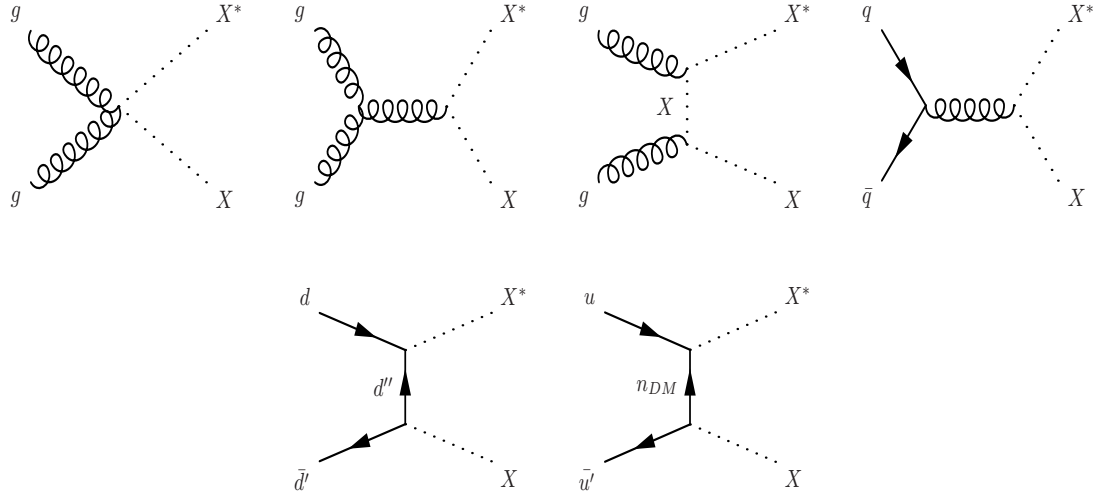
Figure 4.4: Pair production of X

4.2 Model Parameters

The non-thermal DM signal is generated with *MadGraph5* and simulated by CMS full simulation. This model is an example of simplified model and following distinct parameters can be scanned to search for dark matter.

- Dark matter mass ($M_{n_{DM}}$)

- Mediator masses (M_{X_1}, M_{X_2})

- Coupling to standard model (λ_1)

- Coupling to dark matter (λ_2)

Stability of DM is tied to the proton stability given that no additional symmetry e.g. R-parity is invoked. In this case the dark matter and proton mass difference is required to be less than electron mass i.e. $|M_{DM} - M_p| < M_e$. This kinematically stabilizes the dark matter and the proton, resulting that the dark matter mass to be accidentally nearly degenerate with the proton mass.

The other model parameters M_{X_1}, M_{X_2}, λ_1 and λ_2 are allowed to vary. The lighter one of Xs dominates the cross-section in most cases. When interference between X_1 and X_2 occurs, the complex phases cannot be neglected. To simplify our study we assume X_1 be much lighter than X_2 so that the interference becomes negligible. Following mediator mass points are considered:

$$M_{X_2} = \{8000\}\,\text{GeV}$$

$$M_{X_1} = \{500, 750, 1000, 1500, 2000, 2500\}\,\text{GeV}$$

In the heavy M_X limit, the coupling parameter dependence leads the monojet cross-section (Eq. 4.4) into two regions:

(i) $\lambda_1 \approx \lambda_2 \equiv \lambda$ and $\sigma = |\lambda|^2$

(ii) $\lambda_1 \ll \lambda_2$ or $\lambda_2 \ll \lambda_1$, where X width is denominated by the larger of λ_1, λ_2 and hence $\sigma \propto |\min(\lambda_1, \lambda_2)|^2$.

In dijet channel, compared to the monojet case, λ_2 is almost irrelevant unless it is larger than λ_1 and dominates the X scalar width (Eq. 4.5).

At each mediator mass, the $\lambda_1 - \lambda_2$ space is populated by a 16×16 grid of points as follows.

$$\lambda_1 = \{0.01, 0.02, 0.03, 0.04, 0.05, 0.06, 0.07, 0.08, 0.09, 0.1, 0.2, 0.5, 1.0, 2.0, 5.0, 10.0\}$$

$$\lambda_2 = \{0.01, 0.02, 0.03, 0.04, 0.05, 0.06, 0.07, 0.08, 0.09, 0.1, 0.2, 0.5, 1.0, 2.0, 5.0, 10.0\}$$

Figure 4.6 & 4.7 show generator level $\not{E}_T$ for a subset of coupling grid (λ_1, λ_2) for several $M_{X_1} = \{1.0, 1.5, 2.0, 2.5\}$ TeV. We are interested in the parameter space (λ_1, λ_2) where $\not{E}_T$ shows a clear jacobian peak. For large values of λ_1 the monojet production cross section increases but for higher values of λ_1 i.e. $\lambda_1 > 2$ the peak starts to disappear (Figure 4.5 left).

At this point mediator *X* becomes virtual (Figure 4.5 right), which essentially suppresses the decay into monojet channel (as can be seen in branching ratio plot Figure 4.2) and leads in increase of dijet events.

On the other hand, for larger values of λ_2 i.e. $\lambda_2 > 0.5$, two jets plus $\not{E}_T$ channel contributes considerably (Figure 4.6 & 4.7).
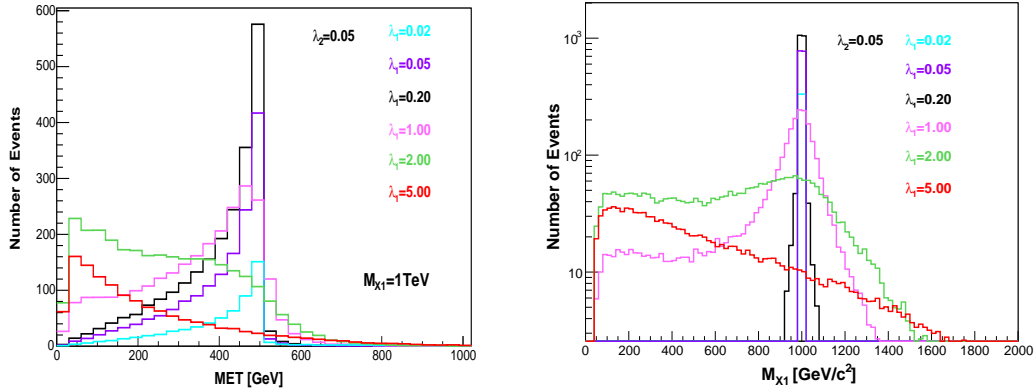
Figure 4.5: Distribution of $\not{E}_T$ (left) and M_{X_1} (right) for various λ_1 while λ_2 =0.05 for 50 fb^{-1}. The number of events in signal region is suppressed by a factor of ≈ 4 for λ_1=5.0 (red) with respect to λ_1=0.05 (purple).

The mediator mass distributions for several M_{X_1} are represented in (λ_1, λ_2) coupling parameter space (Figure 4.8 & 4.9). Mediator widths for several λ_1 and λ_2 are enlisted in Table $4.1 - 4.4$. Generator level study for higher M_{X_1} is also carried out and corresponding plots are in Appendix A.
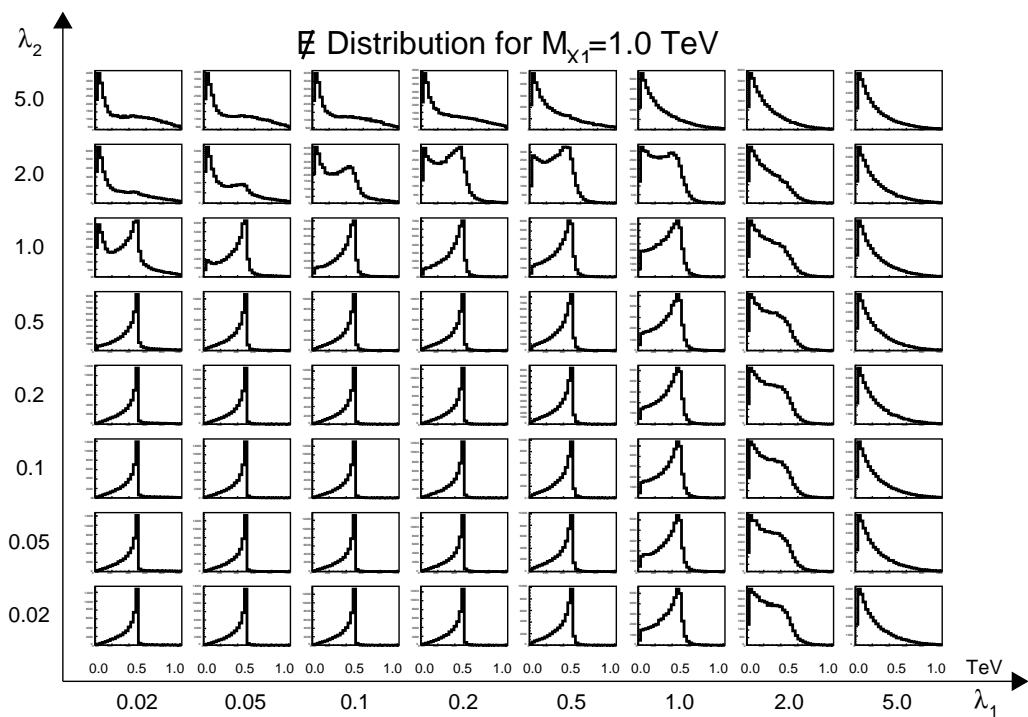
(a)
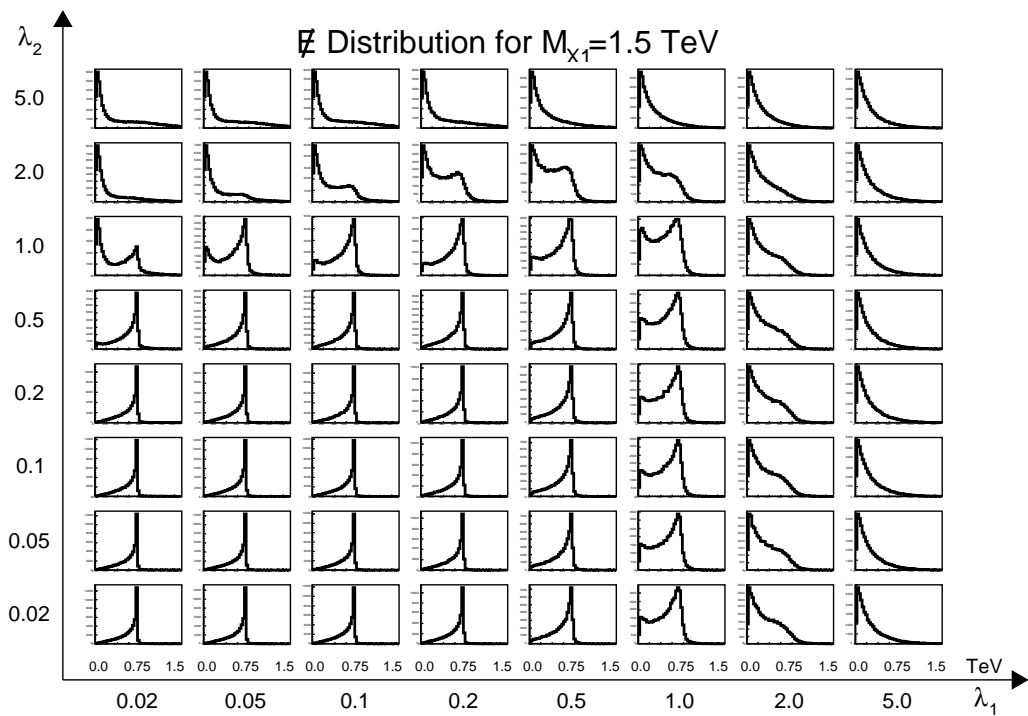
(b)

Figure 4.6: Generator level $\not{E}_T$ for M_{X_1} (a) 1.0 TeV and (b) 1.5 TeV as a function of (λ_1, λ_2). $\not{E}_T$ peaks at half of the mediator mass.   50
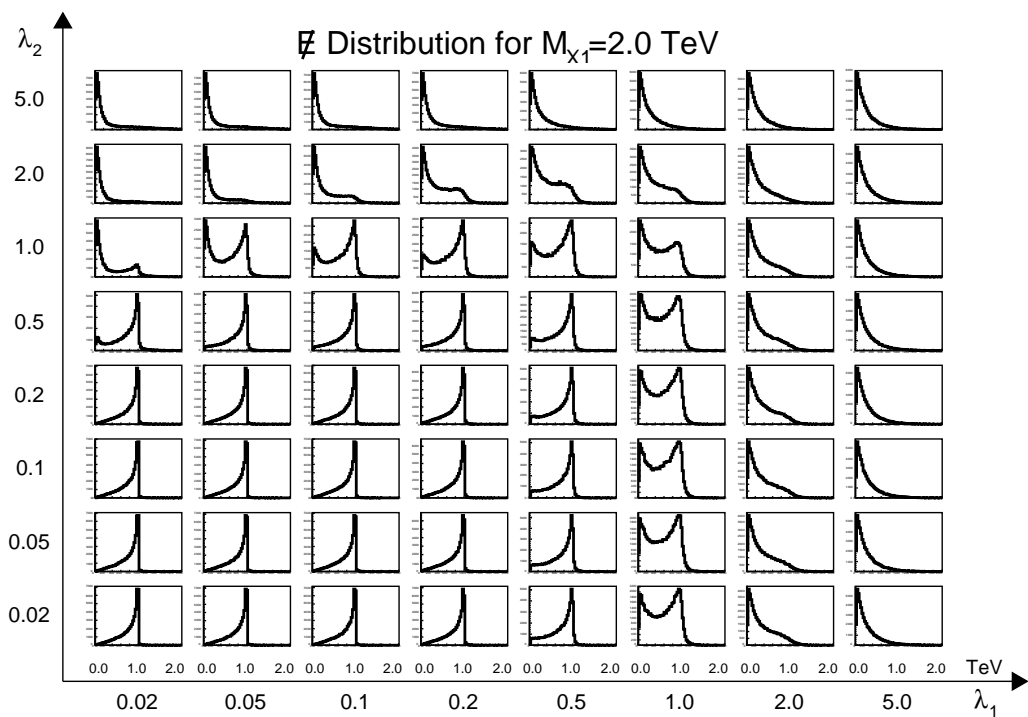
(a)
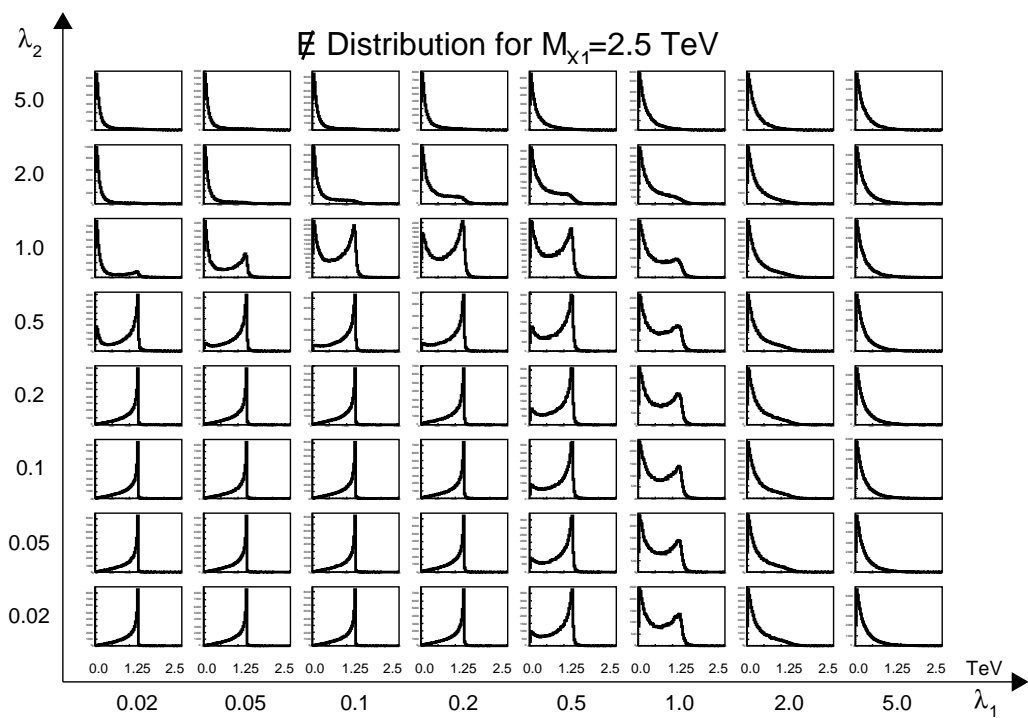
(b)

Figure 4.7: Generator level $\not{E}_T$ for M_{X_1} (a) 2.0 TeV and (b) 2.5 TeV as a function of (λ_1, λ_2). $\not{E}_T$ peaks at half of the mediator mass.   51

λ_1	M_{X_1} Width (Γ) [GeV]							
	λ_2=0.02	λ_2=0.05	λ_2=0.10	λ_2=0.20	λ_2=0.50	λ_2=1.00	λ_2=2.00	λ_2=5.00
0.02	0.072	0.322	1.217	4.797	29.86	119.3	477.4	2983
0.05	0.196	0.447	1.342	4.923	29.98	119.5	477.5	2984
0.10	0.644	0.895	1.790	5.370	30.43	119.9	477.9	2984
0.20	2.434	2.685	3.580	7.160	32.22	121.7	479.7	2986
0.50	14.96	15.22	16.11	19.69	44.75	134.2	492.3	2998
1.00	59.72	59.96	60.86	64.44	89.50	179.0	537.0	3043
2.00	238.7	239.0	239.9	243.4	268.5	358.0	716.0	3222
5.00	1492	1492	1493	1496	1522	1611	1969	4475

Table 4.1: Mass width of $M_{X_1} = 1.0$ TeV, for different coupling points in (λ_1, λ_2) parameter grid.

λ_1	M_{X_1} Width (Γ) [GeV]							
	λ_2=0.02	λ_2=0.05	λ_2=0.10	λ_2=0.20	λ_2=0.50	λ_2=1.00	λ_2=2.00	λ_2=5.00
0.02	0.107	0.483	1.826	7.196	44.78	179.0	716.1	4475
0.05	0.295	0.671	2.014	7.384	44.98	179.2	716.3	4475
0.10	0.967	1.343	2.685	8.055	45.65	180.0	717.0	4476
0.20	3.65	4.027	5.370	10.74	48.33	182.6	719.6	4479
0.50	22.4	22.82	24.17	29.54	67.12	201.4	738.4	4498
1.00	89.6	89.9	91.29	96.67	134.2	268.5	805.5	4565
2.00	358.	358.5	359.8	365.2	402.8	537.0	1074	4833
5.00	2238	2238	2239	2245	2282	2417	2954	6713

Table 4.2: Mass width of $M_{X_1} = 1.5$ TeV, for different coupling points in (λ_1, λ_2) parameter grid.

λ_1	M_{X_1} Width (Γ) [GeV]							
	λ_2=0.02	λ_2=0.05	λ_2=0.10	λ_2=0.20	λ_2=0.50	λ_2=1.00	λ_2=2.00	λ_2=5.00
0.02	0.143	0.3938	1.289	4.869	29.93	119.4	477.4	2983
0.05	0.644	0.895	1.790	5.370	30.43	119.9	477.9	2984
0.10	2.434	2.685	3.580	7.160	32.22	121.7	479.7	2986
0.20	9.594	9.845	10.74	14.32	39.38	128.9	486.9	2993
0.50	59.71	59.96	60.86	64.44	89.50	179.0	537.0	3043
1.00	238.7	238.9	239.9	243.4	268.5	358.0	716.0	3222
2.00	954.7	955.0	955.9	959.4	984.5	1074	1432	3938
5.00	5967	5967	5968	5971	5996	6086	6444	8950

Table 4.3: Mass width of $M_{X_1} = 2.0$ TeV, for different coupling points in (λ_1, λ_2) parameter grid.

λ_1	M_{X_1} Width (Γ) [GeV]							
	λ_2=0.02	λ_2=0.05	λ_2=0.10	λ_2=0.20	λ_2=0.50	λ_2=1.00	λ_2=2.00	λ_2=5.00
0.02	0.179	0.4922	1.611	6.086	37.41	149.2	596.8	3729
0.05	0.805	1.118	2.237	6.712	38.03	149.9	597.4	3730
0.10	3.043	3.356	4.475	8.950	40.27	152.1	599.6	3732
0.20	11.99	12.30	13.42	17.90	49.22	161.1	608.6	3741
0.50	74.64	74.96	76.07	80.55	111.8	223.7	671.2	3804
1.00	298.4	298.7	299.8	304.3	335.6	447.5	895.0	4028
2.00	1193	1194	1195	1199	1230	1342	1790	4922
5.00	7458	7459	7460	7464	7496	7608	8055	11188

Table 4.4: Mass width of $M_{X_1} = 2.5$ TeV, for different coupling points in (λ_1, λ_2) parameter grid.
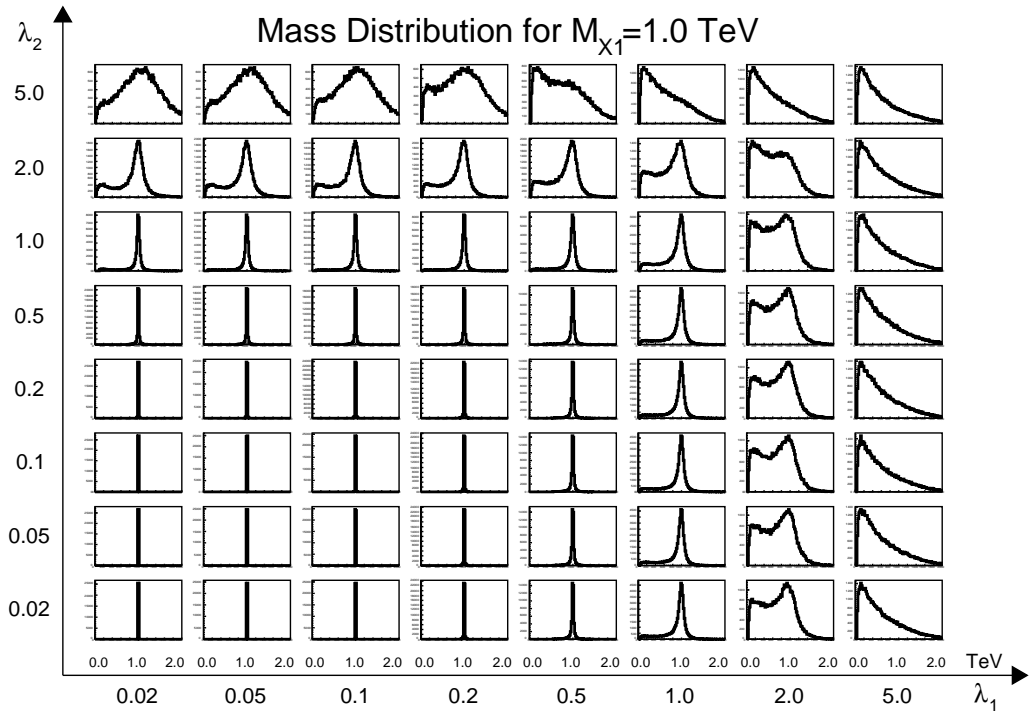
(a)
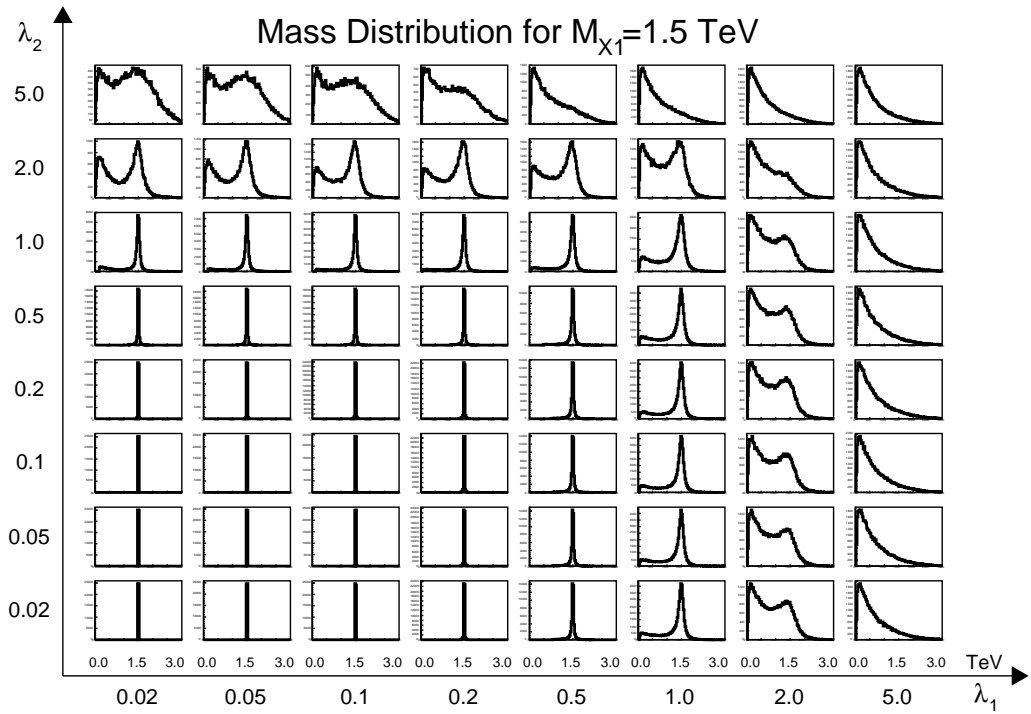
(b)

Figure 4.8: Mass distribution for M_{X_1} (a) 1.0 TeV and (b) 1.5 TeV as a function of (λ_1, λ_2).
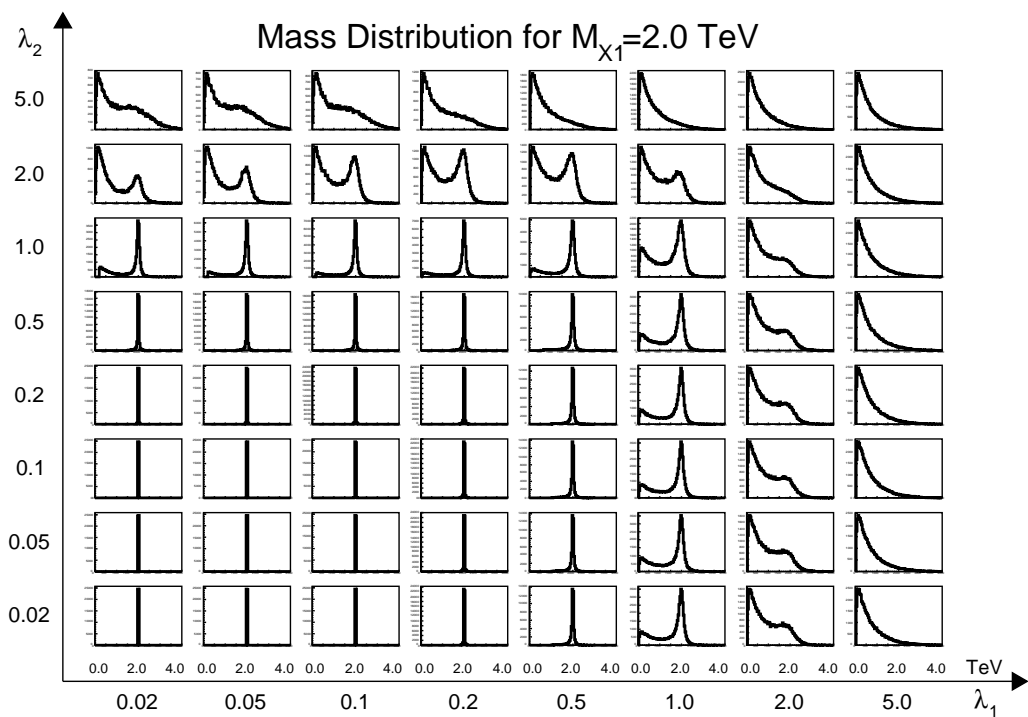
(a)
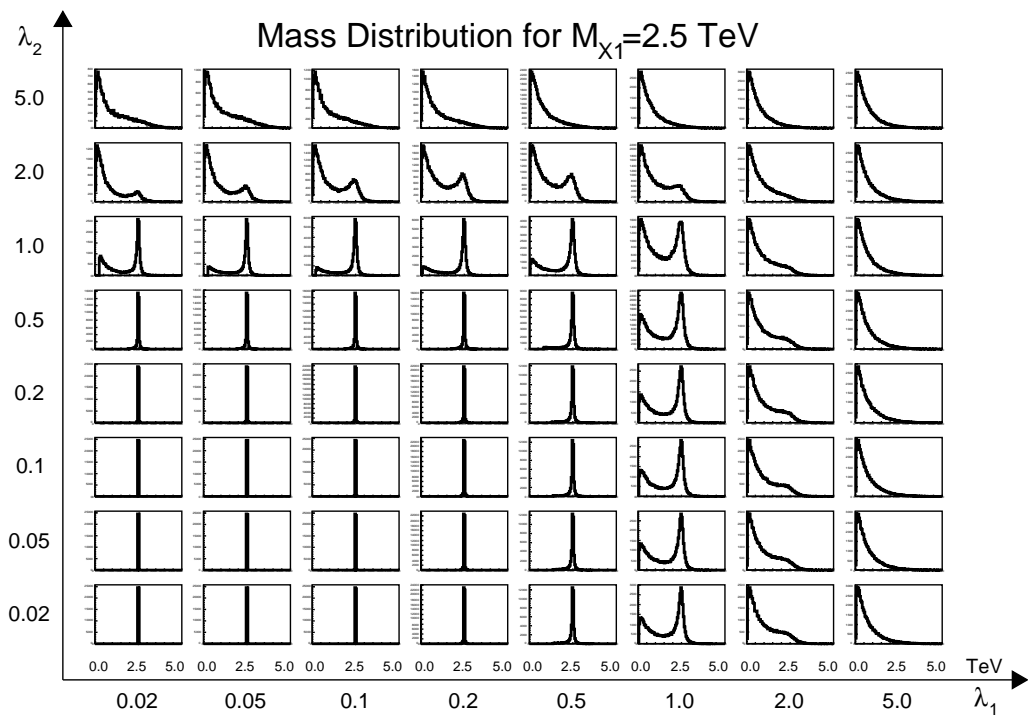
(b)

Figure 4.9: Mass distribution for M_{X_1} (a) 2.0 TeV and (b) 2.5 TeV as a function of (λ_1, λ_2).

(a)

(b)

(c)

(d)

(e)
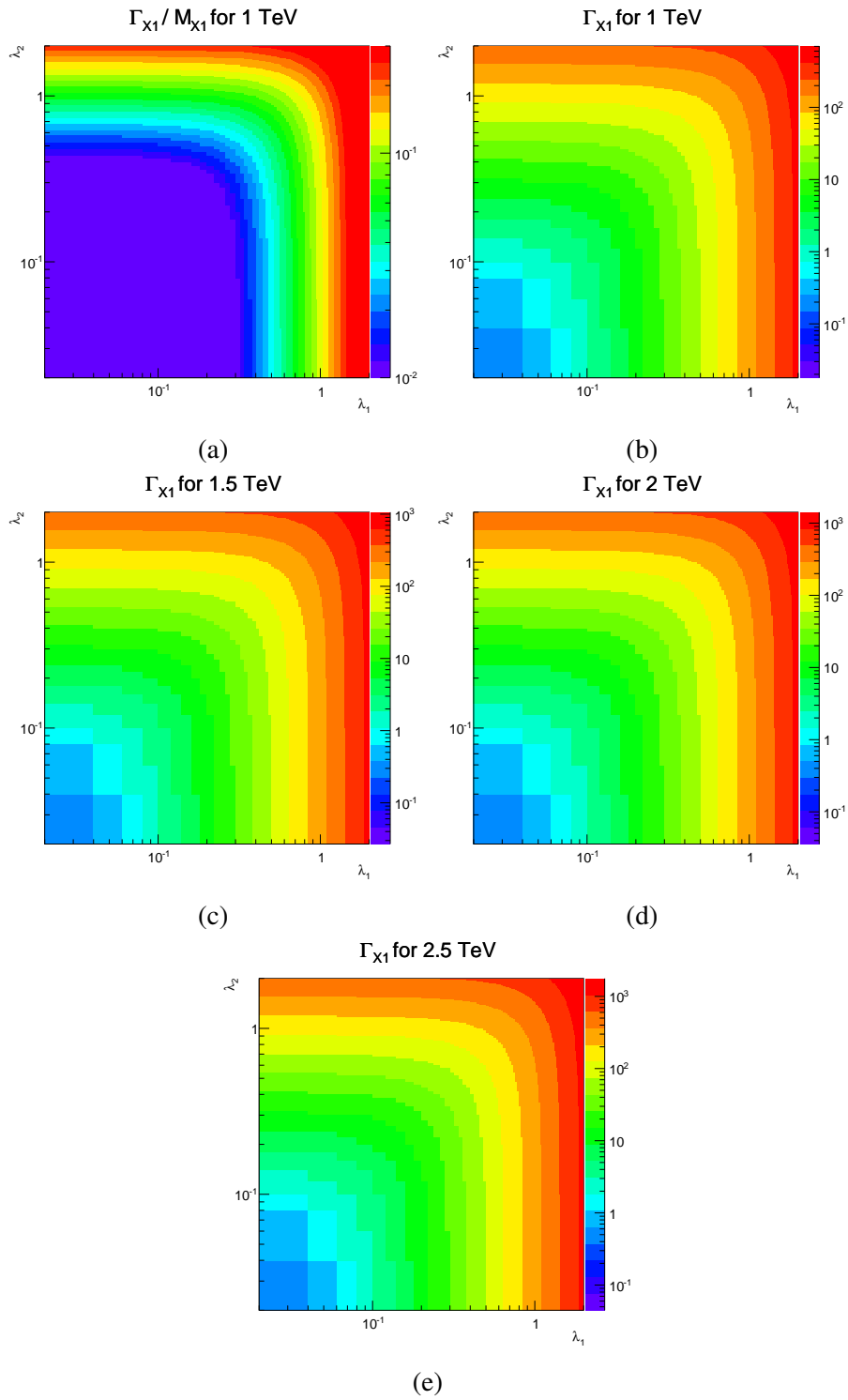
Figure 4.10: Figure shows (a) mass width ratio (Γ/M_{X_1}) for $M_{X_1} = 1.0$ TeV and mass width (Γ) for $M_{X_1} =$ (b) 1.0 TeV, (c) 1.5 TeV, (d) 2.0 TeV and (e) 2.5 TeV as a function of (λ_1, λ_2).

4.2.1 Cross-section vs Coupling and M_{X_1}

This analysis includes monojet and two jets plus $\not{E}_T$ channels. As X_1 gets heavier the cross-section gets smaller. Cross-section is plotted as a function of M_{X_1} for different coupling selections (λ_1, λ_2) in Figure 4.11. Production cross-section σ also depends on coupling constants λ_1 and λ_2. Figure 4.12 shows cross-section for several M_{X_1} as a function of λ_1 while keeping λ_2 fixed. At larger values of λ_1 (i.e. $\lambda_1 > 2$) production cross section starts to drop as dijet channel dominates here.

Table 4.5 represents cross-section σ for various M_{X_1} and coupling parameters (λ_1, λ_2) whereas Table(4.6− 4.9) show variation in cross-section with different λ_1 while λ_2 remains fixed.
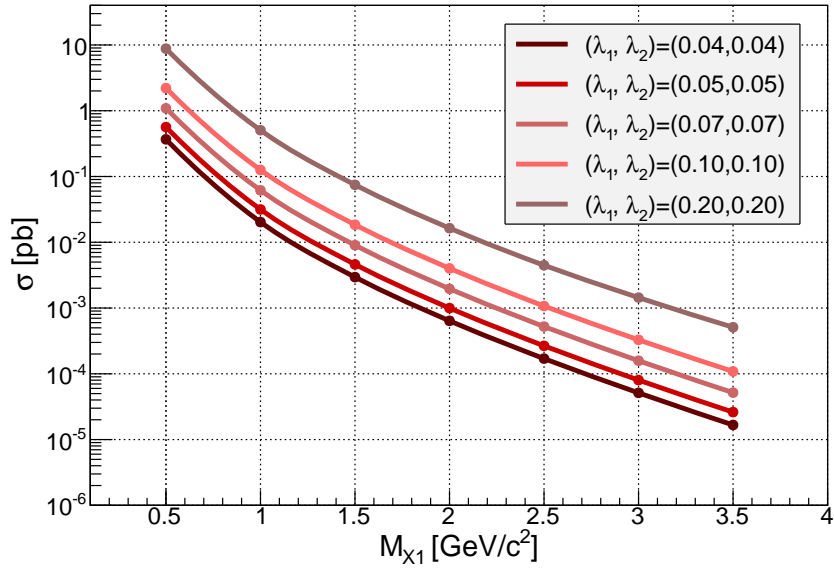
Figure 4.11: Cross-section σ as a function of mediator mass M_{X_1}. Each curve is for a fixed (λ_1, λ_2)

M$_{X_1}$ [GeV]	Cross-Section σ [pb] for (λ_1,λ_2)				
	(0.04,0.04)	(0.05,0.05)	(0.07,0.07)	(0.10,0.10)	(0.20,0.20)
500	0.36723	0.56434	1.08880	2.20590	8.78450
1000	0.02027	0.03154	0.06164	0.12572	0.50543
1500	0.00295	0.00460	0.00903	0.01846	0.07467
2000	0.00064	0.00099	0.00196	0.00401	0.01637
2500	0.00017	0.00027	0.00052	0.00107	0.00447
3000	0.00005	0.00008	0.00015	0.00033	0.00144
3500	0.00002	0.00003	0.00005	0.00011	0.00051

Table 4.5: Non-thermal DM model cross-sections for combined monojet and 2 jets plus $\not{E}_T$ signal for several mediator masses M$_{X_1}$ assuming dark matter mass to be $\sim$ 1 GeV .

λ_1	Cross-Section σ [pb] (M$_{X_1}$ = 1 TeV)			
	λ_2=0.05	λ_2=0.10	λ_2=0.20	λ_2=0.50
0.01	0.00510	0.00556	0.00593	0.00846
0.02	0.01248	0.01559	0.01689	0.01983
0.05	0.03154	0.06354	0.08552	0.09809
0.10	0.04185	0.12572	0.25271	0.35874
0.20	0.04579	0.16804	0.50543	1.16720
0.50	0.04832	0.19036	0.72114	3.28830
1.00	0.05270	0.21001	0.82869	4.74460
2.00	0.05962	0.23813	0.94940	5.78540
5.00	0.02695	0.10790	0.42998	2.66940
10.0	0.00770	0.03088	0.12481	0.77701

Table 4.6: Non-thermal DM model cross-sections for combined monojet and 2 jets plus $\not{E}_T$ signal for various λ_1 with M$_{X_1}$ = 1 TeV while keeping λ_2 fixed.
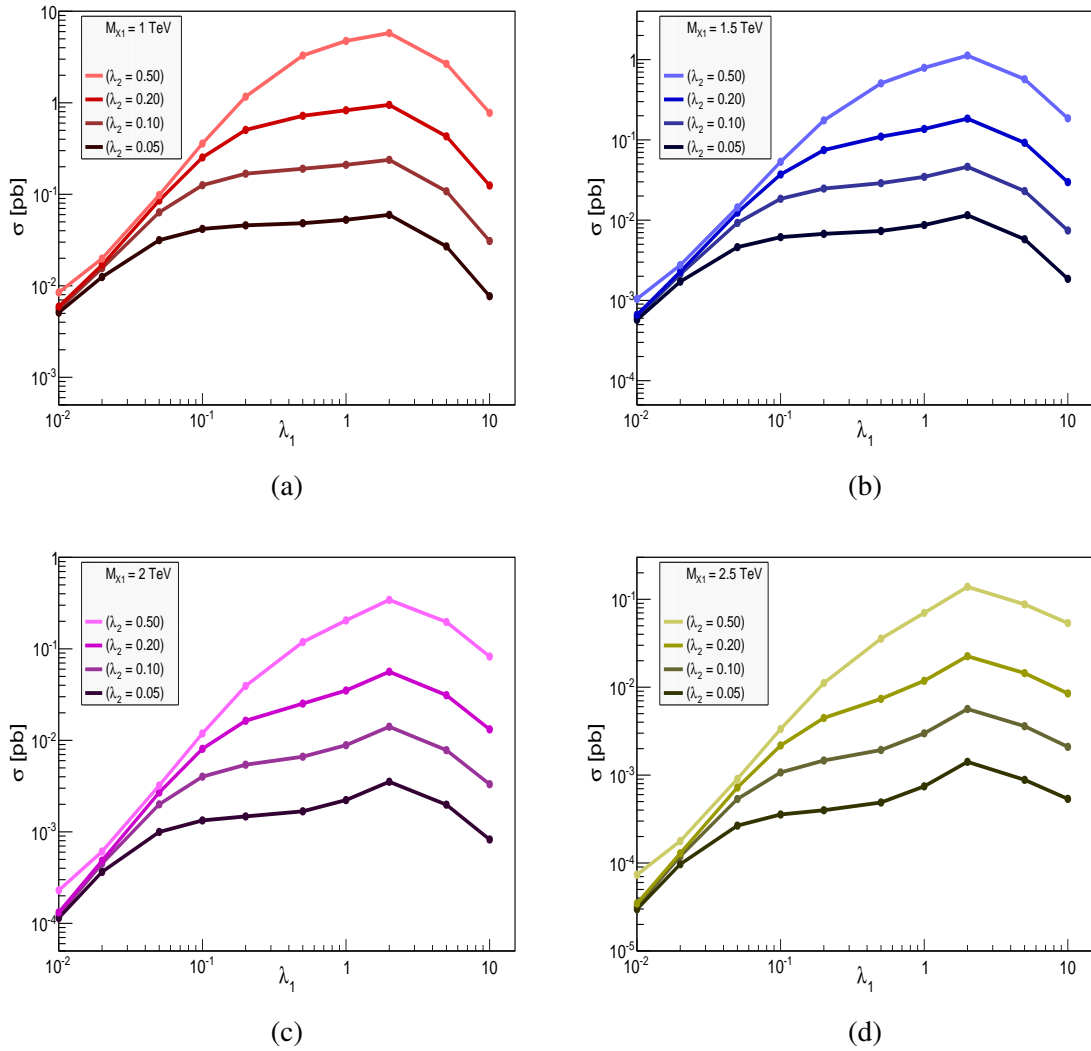
Figure 4.12: Cross-section σ as a function of coupling λ_1 for M_{X_1} = (a) 1.0 TeV, (b) 1.5 TeV, (c) 2.0 TeV and (d) 2.5 TeV.

λ_1	Cross-Section σ [pb] (M_{X_1} = 1.5 TeV)			
	λ_2=0.05	λ_2=0.10	λ_2=0.20	λ_2=0.50
0.01	0.00057	0.00062	0.00066	0.00104
0.02	0.00171	0.00211	0.00228	0.00275
0.05	0.00461	0.00924	0.01241	0.01440
0.10	0.00614	0.01846	0.03710	0.05335
0.20	0.00675	0.02476	0.07466	0.17499
0.50	0.00733	0.02892	0.10977	0.50651
1.00	0.00869	0.03462	0.13680	0.79137
2.00	0.01153	0.04627	0.18402	1.12420
5.00	0.00578	0.02304	0.092047	0.57047
10.0	0.00186	0.00744	0.029771	0.18578

Table 4.7: Non-thermal DM model cross-sections for combined monojet and 2 jets plus $\not{E}_T$ signal for various λ_1 with M_{X_1} = 1.5 TeV while keeping λ_2 fixed.

λ_1	Cross-Section σ [pb] (M_{X_1} = 2 TeV)			
	λ_2=0.05	λ_2=0.10	λ_2=0.20	λ_2=0.50
0.01	0.00011	0.00012	0.00013	0.00023
0.02	0.00036	0.00045	0.00048	0.00061
0.05	0.00099	0.00199	0.00269	0.00321
0.10	0.00133	0.00401	0.00808	0.01190
0.20	0.00147	0.00542	0.01637	0.03932
0.50	0.00167	0.00663	0.02521	0.11871
1.00	0.00222	0.00885	0.03506	0.20461
2.00	0.00353	0.01410	0.05623	0.34284
5.00	0.00198	0.00782	0.03117	0.19673
10.0	0.00082	0.00332	0.01319	0.08251

Table 4.8: Non-thermal DM model cross-sections for combined monojet and 2 jets plus $\not{E}_T$ signal for various λ_1 with M_{X_1} = 2 TeV while keeping λ_2 fixed.

λ_1	Cross-Section σ [pb] (M_{X_1} = 2.5 TeV)			
	λ_2=0.05	λ_2=0.10	λ_2=0.20	λ_2=0.50
0.01	0.000029	0.000031	0.000034	0.00007
0.02	0.00009	0.00012	0.00013	0.00017
0.05	0.00027	0.00053	0.00072	0.00090
0.10	0.00035	0.00107	0.00217	0.00334
0.20	0.00039	0.00147	0.00446	0.01115
0.50	0.00049	0.00192	0.00737	0.03565
1.00	0.00074	0.00298	0.01183	0.07005
2.00	0.00141	0.00564	0.02254	0.13871
5.00	0.00088	0.00360	0.01445	0.08758
10.0	0.00054	0.00210	0.00849	0.05362

Table 4.9: Non-thermal DM model cross-sections for combined monojet and 2 jets plus $\not{E}_T$ signal for various λ_1 with M_{X_1} = 2.5 TeV while keeping λ_2 fixed.

4.2.2 Generator Level Cuts

The signal events are generated in $Madgraph5$ with jet $p_T > 20$ GeV. A study is carried out with different jet p_T cut for various resonance masses M_{X_1}. The percentage increase in cross-section (for jet p_T = 20-0 GeV) is less than 2% , as shown in Table 4.10. The generator level cut does not affect the efficiency of the signal much.
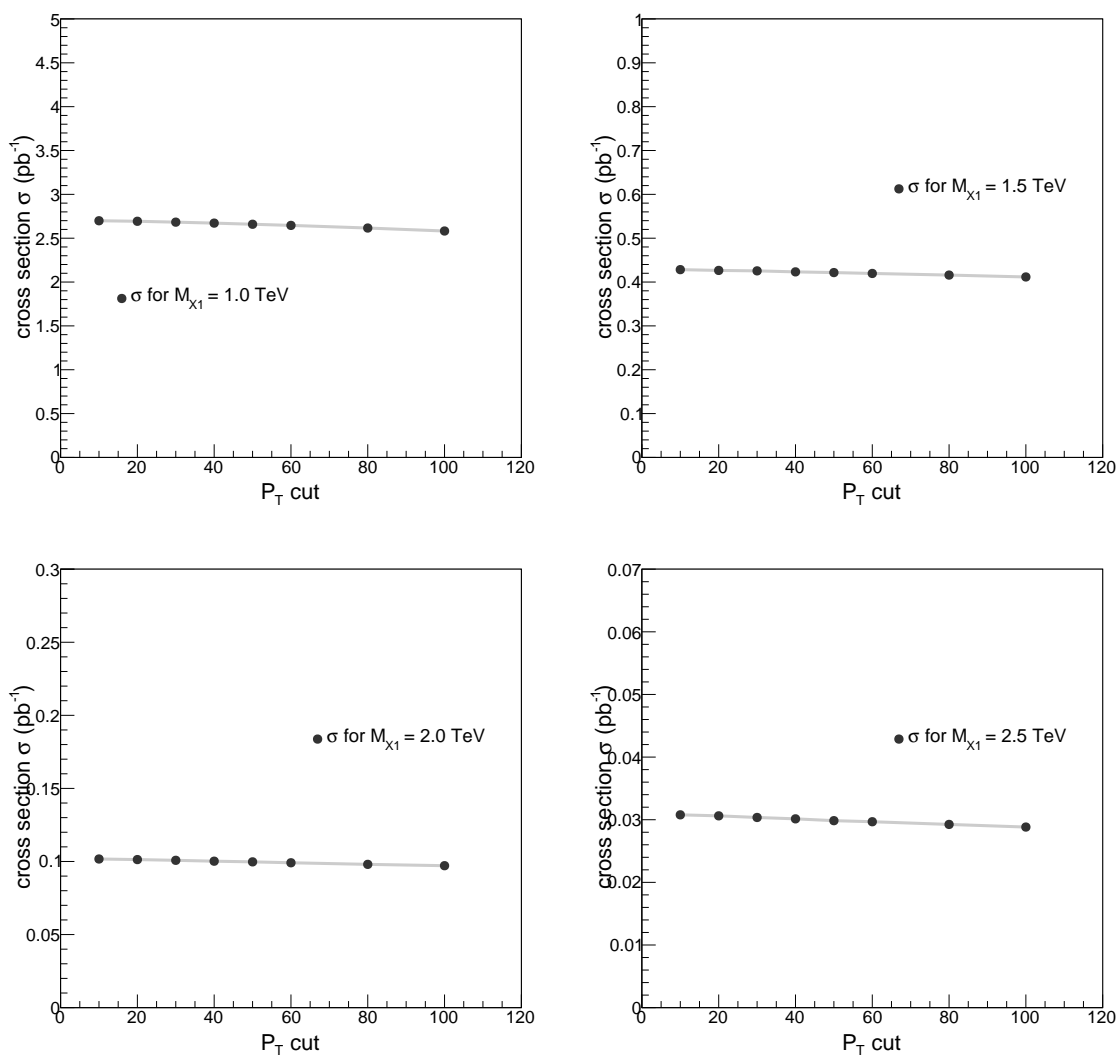
Figure 4.13: Cross section variation as a function of generator level cut on jet p_T is shown for various resonance masses M_{X_1} is plotted.

M_{X_1}	1.0 TeV	1.5 TeV	2.0 TeV	2.5 TeV
Increase in σ	0.26 %	0.82 %	0.69 %	1.24 %

Table 4.10: The percentage increase in cross-section for 20 GeV to 0 GeV generator level jet p_T cut.

4.2.3 Signal Acceptance vs Resonance Mass M_{X_1}

Acceptance of non-thermal DM signal is calculated as follows:

$$\frac{\text{events passing selection cuts}}{\text{total number of events}} \tag{4.6}$$

Signal acceptance gradually increases with the increase in resonance mass but this increase is slight and almost constant within the monojet channel dominant region of the coupling parameter space i.e. for the range $\lambda_1 = [0.01-0.5]$ and $\lambda_2 = [0.01-0.5]$. Figure 4.14 shows acceptance as a function of mediator mass M_{X_1}.
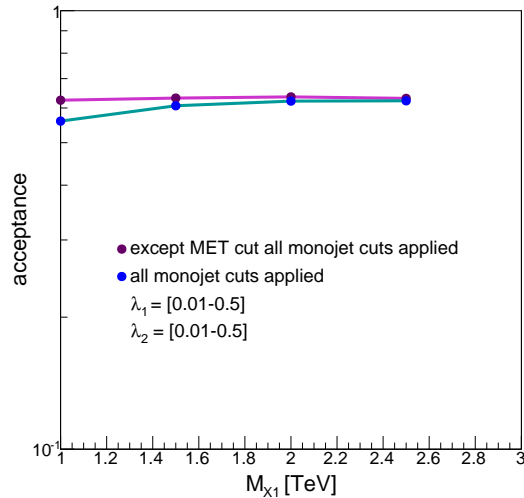
Figure 4.14: Acceptance as a function of resonance mass. The pink plot is after all monojet cuts applied (except $\not{E}_T$ cut), whereas blue is for all monojet selections applied including $\not{E}_T > 250$ GeV. The acceptance shows almost constant behavior with increasing resonance mass.

4.3   Run 1 Limit on Non-thermal Dark Matter Model

4.3.1   Pheno Recast

Pheno recast collider constraints for all previously discussed channels, are shown in this section. Two benchmark mediator masses $(M_{X_1} = 500$ GeV and 1.0 TeV$)$ are considered to calculate the signal cross-section and compare with new physics bounds in each production channel [128]. Non-thermal DM signal samples are generated at parton level through *MadGraph5*.

Monojet events are selected with jets in the central region of detector with pseudorapidity $|\eta| < 2.4$, moreover several $\not{E}_T$ thresholds are considered as listed in [131] for CMS Run-1 data at center of mass energy 8 TeV and total integrated luminosity of 20 fb^{-1}.

The 95% C.L. limits for most stringent cuts are plotted on the $\lambda_1 - \lambda_2$ coupling parameter space for both benchmarks, as shown in Figure 4.15 (blue). If $\lambda_1 >> \lambda_2$ or $\lambda_2 >> \lambda_1$, the monojet channel cross-section depends on smaller of the two couplings and from Figure 4.15, the smaller coupling is roughly of the order of 0.1.

Dijet limit is produced by using CDF results from [132] with $\sqrt{s} = 1.96$ TeV and integrated luminosity 1.13 fb^{-1}. Figure 4.15 (red) shows the 95% C.L. bound on dijet channel which depends only on λ_1.

Two jets plus $\not{E}_T$ limit is computed by considering the contribution from ISGS (Figure 4.3) and X pair production (Figure 4.4). The event selection criteria is taken from ATLAS's multijet $+\not{E}_T$ study [133] and corresponding 95% C.L. bounds are shown in Figure 4.15 (orange).

Finally paired dijets limit is calculated for X pair production processes where each X decays to dijet. The results are produced by using CMS data analysis from [134] with total integrated luminosity 2.2 fb^{-1} at $\sqrt{s} = 7$ TeV. Figure 4.15 (black) shows 95 % C.L. limits for paired dijet channel.

Comparison of all the collider bounds reveal that monojet channel poses the most significant constraint on coupling parameters, considering only one X contribution.
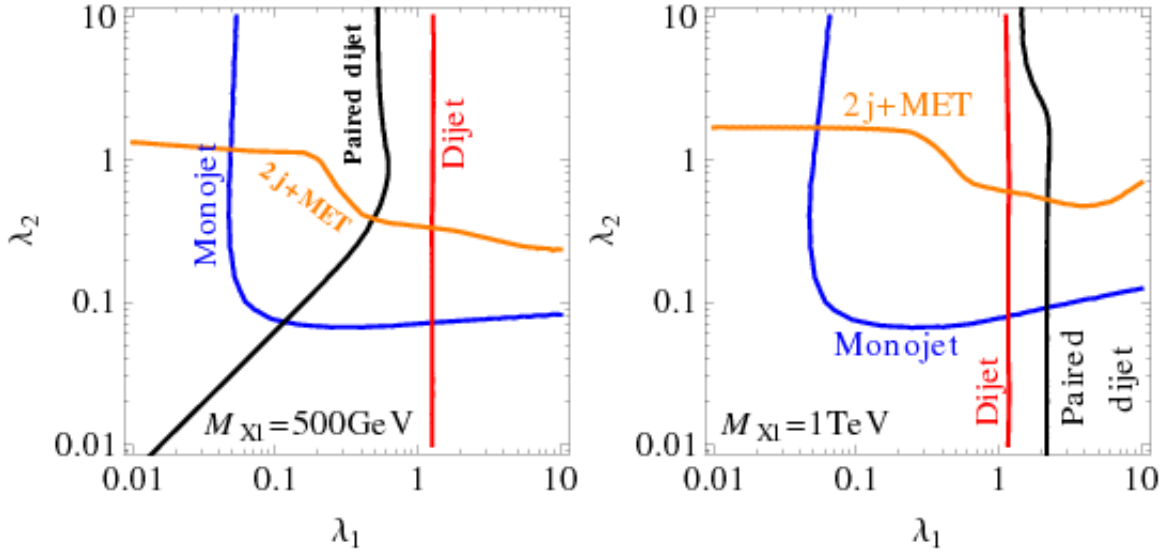
Figure 4.15: A collection of exclusions for mediator benchmarks $M_{X_1} = 500$ GeV (left) and $M_{X_1} = 1$ TeV (right) from run 1 collider results [128].

4.3.2 Our Preliminary Study with Run-1 Data

This preliminary study is conducted to compare our results with pheno-recast theoretical results by using the Run 1, 8 TeV data. The analysis is performed for monojet and 2-jets plus $\not{E}_T$ channels. The Non-thermal DM samples are generated in *MadGraph5* and simulated through Fast Simulation technique. A 10×10 coupling parameter space (λ_1, λ_2) is considered as follows:

$$\lambda_1 = \{0.01, 0.02, 0.05, 0.1, 0.2, 0.5, 1.0, 2.0, 5.0, 10.0\}$$
$$\lambda_2 = \{0.01, 0.02, 0.05, 0.1, 0.2, 0.5, 1.0, 2.0, 5.0, 10.0\}$$

The analysis includes three M_{X_1} benchmark values, i.e. $\{1000, 1500, 2000\}$ GeV and M_{X_2} is fixed at 4000 GeV for all M_{X_1}.

4.3.2.1   Event Selection

Events are selected according to EXO-12-048 [131].

Triggers:

The data for this search was collected using the following high $\not{E}_T$ triggers:

- `HLT_MET120_HBHENoiseCleaned`

- `MonoCentralPFJet80_PFMETnoMu95_NHEF0p95`

- `MonoCentralPFJet80_PFMETnoMu105_NHEF0p95`

Baseline Selection:

The data events are collected by the triggers mentioned above and required to pass a set of event cleaning criteria.

- There should be at least one primary vertex associated to the event.

- Jet cleaning cut i.e. charged hadronic energy fraction > 0.2 (to reject beam halo and cosmic muons), neutral EM energy fraction < 0.7 and neutral hadronic energy fraction < 0.7 (To reject high p_T photons and electrons misidentified as hadronic jets).

- The jets are reconstructed using anti-k_T algorithm with a distance parameter 0.5 and required to have $p_T > 30$ GeV and $| \eta | < 4.5$.

- $\not{E}_T > 200$ GeV (consistent with trigger turn-on).

- Jet multiplicity cut: i.e. events with number of jets > 2 are rejected.

- Events with leading jet $p_T > 110$ GeV are accepted and the jet should be in the central region of detector i.e. $| \eta | < 2.4$.

- $\Delta\phi(jet_1, jet_2) < 2.5$ (to suppress the QCD background).

- The analysis is carried out in seven regions of $\not{E}_T$, i.e. $\not{E}_T > 250, 300, 350, 400, 450, 500$ and 550 GeV.

4.3.2.2   SM Background Predictions and Uncertainties

Standard Model background yields and their uncertainties are taken from AN-12-421 [130] and are given in Table 4.11. Figure 4.16 shows 95% CL expected limit for nonthermal DM model ($M_{X_1} = 1$ TeV) using Run 1 data. Pheno recast bounds from [128] are also shown for $\not{E}_T + 2$ jets (red) and $\not{E}_T + 1$ jet (blue) channels. Run-1 result shows weaker limit as compared to pheno recast one because of different event selections. In later case no cut was applied on jet multiplicity whereas in Run-1 analysis maximum number of accepted jets are 2. Due to this difference in selection criteria ,the cross-section limit is off by a factor of two and by using the relation between cross-section and couplings in Eq. 4.7, we translated Run-1limit to one corresponding to theory results. Orange scattered points in Figure 4.16 show good agreement between translated and pheno recast limits.

$$\sigma \propto \frac{|\lambda_1|^4}{(2|\lambda_1|^2 + |\lambda_2|^2)} \tag{4.7}$$
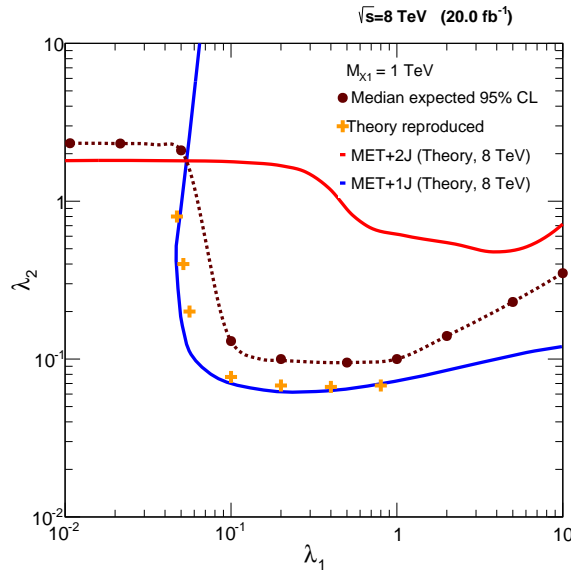
Figure 4.16: 95 % CL expected limit contour and the pheno recast curves from [128] are shown for $M_{X_1} = 1$ TeV in (λ_1, λ_2) parameter space. In order to show consistency with the theory limit [128], translated points (orange) are shown.

$\slashed{E}_T >$	250	300	350	400	450	500	550
$Z(\nu\nu)$+jets	32097 ± 1649	12734 ± 719	5452 ± 359	2735 ± 216	1463 ± 144	747 ± 96	362 ± 64
W+jets	17403 ± 887	5986 ± 319	2363 ± 134	1026 ± 65	508 ± 37	255 ± 23	124 ± 13
$t\bar{t}$	446 ± 223	167 ± 84	69 ± 35	31 ± 16	15 ± 7.7	6.6 ± 3.3	2.8 ± 1.4
$Z(\ell\ell)$+jets	139 ± 70	44 ± 22	18 ± 9.0	8.9 ± 4.4	5.2 ± 2.6	2.3 ± 1.2	1.0 ± 0.5
Single top	155 ± 77	53 ± 26	18 ± 9.1	6.1 ± 3.1	0.9 ± 0.4	0.0 ± 0.0	0.0 ± 0.0
QCD Multijets	443 ± 267	94 ± 57	29 ± 18	4.9 ± 3.0	2.0 ± 1.2	1.0 ± 0.6	0.5 ± 0.3
DiBoson	980 ± 490	440 ± 220	220 ± 110	118 ± 59	65 ± 33	36 ± 18	20 ± 10
Total SM	51664 ± 1970	19518 ± 824	8170 ± 401	3930 ± 234	2060 ± 153	1048 ± 100	510 ± 66
Data	52157	19783	8324	3825	1828	934	519

Table 4.11: Run 1 summary of the SM background predictions and their corresponding uncertainties compared to the data [130].

68

CHAPTER 5

DATASETS AND TRIGGER

This analysis is carried out by using datasets collected in the 2016 by CMS data taking campaign at 13 TeV with an integrated luminosity of 35.9 fb^{-1}. The Monte Carlo background and signal processes are simulated in "Summer16" MC campaign.

5.1 Data

The events are selected in data and five control regions (CR). CR are essential to estimate the potential background processes. For Run2016B to run2016G era of the data taking, 23rd September re-reco has been used, whereas prompt reconstruction is considered for Run2016H. The list of all datasets used in this analysis is shown in Table 5.1.

Dataset	Region Study
MET-Run2016*-23Sep2016 MET-Run2016H-PromptReco-v*	Signal region, Single Muon and Double Muon control regions
/SingleElectron/Run2016*-23Sep2016 /SingleElectron/Run2016H-PromptReco-v*	Single Electron and Double Electron control regions
/SinglePhoton/Run2016*-23Sep2016 /SinglePhoton/Run2016H-PromptReco-v*	γ + jets control region
/JetHT/Run2016*-23Sep2016 /JetHT/Run2016H-PromptReco-v*	Single Electron, Double Electron and γ + jets control regions

Table 5.1: Datasets used in the analysis.

5.2 Background Simulation

There are a number of standard model processes which mimic the dark matter signal and hence are required to be identified and removed from the signal region. These processes are simulated and are shown in the Tables 5.2 and 5.3. Following is a brief description of these background processes:

- $Z(\nu\nu)$ + jets : The main contribution comes from this background as neutrinos go undetected and hence produce real $\not{E}_T$. The Monte Carlo samples for $Z(\nu\nu)$ + jets have been generated through MadGraph at leading order (LO) in QCD in binned hadronic transverse energy sum (H_T).

- $W(l\nu)$ + jets : This is the second largest background in our monojet analysis. The lepton veto is applied to reduce contribution from this process but many times leptons are not detected (produced at large angles in detector or simply are not reconstructed). This situation makes this background process unavoidable. The Monte Carlo samples for $W(l\nu)$ + jets have been generated through MadGraph at leading order (LO) in QCD in several H_T bins.

- $Z(ll)$ + jets : This process poses as background when the leptons pass unseen and contribute to the signal like events. Monte Carlo samples for this background have been generated through MadGraph at leading order (LO) in QCD in several H_T bins.

- γ + jets : This process is not a real background rather it is used to estimate the irreducible $Z(\nu\nu)$ + jets background and hence serves as a control region in this analysis. Monte Carlo samples for γ + jets process have been generated through MadGraph at leading order (LO) in QCD in several H_T bins.

- Diboson (WW, WZ & ZZ) : Each of these processes usually results in leptonic decay of one boson (mimics signal like events), whereas the other boson decays in hadrons (jets). The resulting final state of such processes consist of $\not{E}_T$ and hadronic jets, therefore contributes as a background. Monte Carlo samples for WZ & ZZ have been generated through Pythia 8 at leading order (LO) while Powheg-box at NLO-QCD have been used to generate WW samples.

- Top : Top quark decays into $W + b$ (jets), followed by leptonic decay of W boson. This produces $\not{E}_T$ in the final state. Single top and top pair production are two process

which contribute as the background to monojet dark matter signal. MC samples for $t\bar{t}$ have been generated using aMC@NLO and Powheg generators at next-to-leading order (NLO) whereas single-top events have been produced with the Powheg generator at NLO.

- QCD : QCD events are abundantly produced in the proton-proton collision. Although typically these events do not contribute to large $\not{E}_T$ but since the production rate is high, even a smaller number of events with undetected high transverse momentum jet can behave as a background. QCD Monte Carlo samples have been generated using the MadGraph at leading order (LO) in QCD in several H_T bins.

Process	Dataset Name	σ (pb)	σ Order in QCD
$Z(\nu\nu)$ + jets	/ZJetsToNuNu_HT-100To200_13TeV-madgraph	280.5	LO
	/ZJetsToNuNu_HT-200To400_13TeV-madgraph	77.7	LO
	/ZJetsToNuNu_HT-400To600_13TeV-madgraph	10.71	LO
	/ZJetsToNuNu_HT-600To800_13TeV-madgraph	2.562	LO
	/ZJetsToNuNu_HT-800To1200_13TeV-madgraph	1.183	LO
	/ZJetsToNuNu_HT-1200To2500_13TeV-madgraph	0.286	LO
	/ZJetsToNuNu_HT-2500ToInf_13TeV-madgraph	6.976×10^{-4}	LO
$W(l\nu)$ + jets	/WJetsToLNu_HT-100To200_TuneCUETP8M1_13TeV-madgraphMLM-pythia8	1343	LO
	/WJetsToLNu_HT-200To400_TuneCUETP8M1_13TeV-madgraphMLM-pythia8	359.6	LO
	/WJetsToLNu_HT-400To600_TuneCUETP8M1_13TeV-madgraphMLM-pythia8	48.85	LO
	/WJetsToLNu_HT-600To800_TuneCUETP8M1_13TeV-madgraphMLM-pythia8	12.05	LO
	/WJetsToLNu_HT-800To1200_TuneCUETP8M1_13TeV-madgraphMLM-pythia8	5.501	LO
	/WJetsToLNu_HT-1200To2500_TuneCUETP8M1_13TeV-madgraphMLM-pythia8	1.329	LO
	/WJetsToLNu_HT-2500ToInf_TuneCUETP8M1_13TeV-madgraphMLM-pythia8	0.03216	LO
$Z(ll)$ + jets	/DYJetsToLL_M-50_HT-100to200_TuneCUETP8M1_13TeV-madgraphMLM-pythia8	148	LO
	/DYJetsToLL_M-50_HT-200to400_TuneCUETP8M1_13TeV-madgraphMLM-pythia8	40.94	LO
	/DYJetsToLL_M-50_HT-400to600_TuneCUETP8M1_13TeV-madgraphMLM-pythia8	5.497	LO
	/DYJetsToLL_M-50_HT-600to800_TuneCUETP8M1_13TeV-madgraphMLM-pythia8	1.354	LO
	/DYJetsToLL_M-50_HT-800to1200_TuneCUETP8M1_13TeV-madgraphMLM-pythia8	0.625	LO
	/DYJetsToLL_M-50_HT-1200to2500_TuneCUETP8M1_13TeV-madgraphMLM-pythia8	0.151	LO
	/DYJetsToLL_M-50_HT-2500toInf_TuneCUETP8M1_13TeV-madgraphMLM-pythia8	3.647×10^{-3}	LO
$t\bar{t}$	/TTJets_TuneCUETP8M1_13TeV-amcatnloFXFX-pythia8	831.76	NNLO+NNLL
	/TT_TuneCUETP8M1_13TeV-powheg-pythia8	831.76	NNLO+NNLL

Table 5.2: Monte Carlo datasets for background processes produced in the Spring16 Campaign.

Process	Dataset Name	σ (pb)	σ Order in QCD
γ +jets	/GJets_HT-100To200_TuneCUETP8M1_13TeV-madgraphMLM-pythia8	9235	LO
	/GJets_HT-200To400_TuneCUETP8M1_13TeV-madgraphMLM-pythia8	2298	LO
	/GJets_HT-400To600_TuneCUETP8M1_13TeV-madgraphMLM-pythia8	277.6	LO
	/GJets_HT-600ToInf_TuneCUETP8M1_13TeV-madgraphMLM-pythia8	93.47	LO
Single Top	/ST_s-channel_4f_leptonDecays_13TeV-amcatnlo-pythia8_TuneCUETP8M1	3.4	NLO
	/ST_t-channel_top_4f_leptonDecays_13TeV-powheg-pythia8_TuneCUETP8M1	44.1	NLO
	/ST_t-channel_antitop_4f_leptonDecays_13TeV-powheg-pythia8_TuneCUETP8M1	26.2	NLO
	/ST_tW_top_5f_inclusiveDecays_13TeV-powheg-pythia8_TuneCUETP8M1	35.6	NNLO
	/ST_tW_antitop_5f_inclusiveDecays_13TeV-powheg-pythia8_TuneCUETP8M1	35.6	NNLO
Diboson	/WWTo2L2Nu_13TeV-powheg	12.18	NLO
	/WWTo4Q_13TeV-powheg	49.99	NLO
	/WWToLNuQQ_13TeV-powheg	51.72	NLO
	/WW_TuneCUETP8M1_13TeV-pythia8	118.7	NNLO
	/WZ_TuneCUETP8M1_13TeV-pythia8	47.2	NLO
	/ZZ_TuneCUETP8M1_13TeV-pythia8	16.6	NLO
QCD	/QCD_HT100to200_TuneCUETP8M1_13TeV-madgraphMLM-pythia8	2.75×10^7	LO
	/QCD_HT200to300_TuneCUETP8M1_13TeV-madgraphMLM-pythia8	1.735×10^6	LO
	/QCD_HT300to500_TuneCUETP8M1_13TeV-madgraphMLM-pythia8	3.67×10^5	LO
	/QCD_HT500to700_TuneCUETP8M1_13TeV-madgraphMLM-pythia8	2.937×10^4	LO
	/QCD_HT700to1000_TuneCUETP8M1_13TeV-madgraphMLM-pythia8	6524	LO
	/QCD_HT1000to1500_TuneCUETP8M1_13TeV-madgraphMLM-pythia8	1064	LO
	/QCD_HT1500to2000_TuneCUETP8M1_13TeV-madgraphMLM-pythia8	121.5	LO
	/QCD_HT2000toInf_TuneCUETP8M1_13TeV-madgraphMLM-pythia8	25.42	LO

Table 5.3: Monte Carlo datasets for background processes produced in the Spring16 Campaign.

5.3 Triggers

This analysis contains data from several triggers. For signal region events are selected through large $\not{E}_T$ and large $\not{H}_T$ triggers. These triggers rely on the online version of particle flow algorithm. PF muons are removed from the $\not{E}_T$ and large $\not{H}_T$ calculations and hence the same triggers can be used for dimuon ($Z \to \mu\mu$) and single-muon ($W \to \mu\nu$) control region studies. Events for single and double electron control region are selected by single electron triggers, whereas γ+jet control region events are selected by single photon triggers. Table 5.4 shows a complete list of all the triggers used in this analysis with corresponding L1 seed and associated primary datasets.

Dataset	HLT path	L1 seed
MET	HLT_PFMET170_*	L1_ETM70 or L1_ETM100
MET	HLT_PFMETNoMu[90]_PFMHTNoMu[90]_IDTight HLT_PFMETNoMu[100]_PFMHTNoMu[100]_IDTight HLT_PFMETNoMu[110]_PFMHTNoMu[110]_IDTight HLT_PFMETNoMu[120]_PFMHTNoMu[120]_IDTight	L1_ETM70 or L1_ETM100 L1_ETM60_NotJet52WdPhi2
Single Electron	HLT_Ele27_WPTight	L1_SingleEG20 L1_SingleIsoEG18er L1_SingleIsoEG20
Single Electron	HLT_Ele105_CaloIdVT_GsfTrkIdT	L1_SingleEG40 L1_SingleJet200
Single Photon	HLT_Photon165_HE10	L1_SingleEG40 L1_SingleJet200
Single Photon	HLT_Photon175	L1_SingleEG40 L1_SingleJet200
Jet HT	HLT_EcalHT800	L1_ETM70

Table 5.4: HLT paths and corresponding L1 seeds used to collect data for primary datasets.

5.3.1 $\not{E}_T$ Trigger Performance

$\not{E}_T$ trigger performance is measured after monojet selection is carried out in single electron ($W \to e\nu$) as well as single muon ($W \to \mu\nu$) events. Single electron events are selected form SingleElectron dataset and electrons are subjected to certain tight identification criteria with $p_T > 40$ GeV. On the other hand single muon events are selected from SingleMuon dataset with p_T threshold 20 GeV and tight selection requirement. In addition

to above mentioned requirement for two cases, leading jet is required to have large transverse momentum i.e. $p_T > 100$ GeV. In single electron case trigger efficiency is plotted as a function of $\not{E}_T$ whereas for single muon events, trigger efficiency is computed with respect to $\not{E}_T$ recoil i.e. by removing muon contribution from $\not{E}_T$ calculation. $\not{E}_T$ trigger turn-on curves are shown in the Figure 5.1 and are found to agree very well in the plateau region, differing by at most 1-2% for $\not{E}_T$(or recoil) greater than 200 GeV.

(a)   (b)
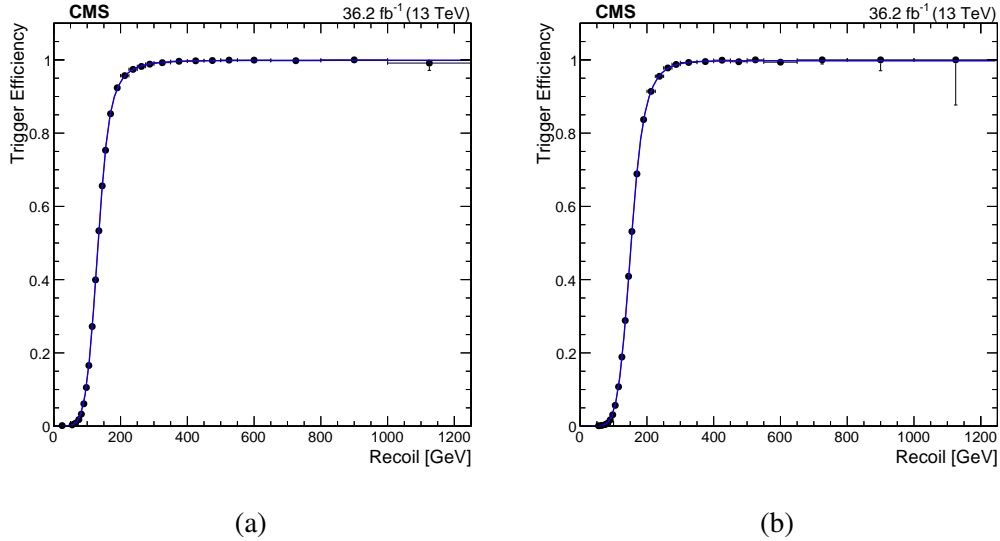
Figure 5.1: $\not{E}_T$ trigger efficiency computed as a function of recoil in single muon events (a) whereas in single electron events it is plotted as a function of $\not{E}_T$ (b) [146].

5.3.2 Electron Trigger Performance

Events passing from a logical OR of Ele27 and Ele105 triggers are selected for single electron and double electron control regions. The Ele27 trigger has tight identification and isolation requirements whereas the Ele105 trigger has just a loose identification and no isolation requirements. In case of boosted Z boson ($Z \rightarrow e^+e^-$) two electron can spoil each others isolation and in turn the Ele27 trigger efficiency is affected. Ele105 trigger has no isolation requirement and therefore helps in improving the trigger efficiency. Two approaches are followed to compute trigger efficiency i.e.

(i) Tag-and-probe method is used for low electron p_T, where one electron is needed to fire single electron trigger and pass certain tight selection (tag). The second electron is also required to be in event and subjected to pass tight identification criteria as well (probe). Finally two tag and probe electrons must have invariant mass consistent to Z peak. Efficiency is given by fraction of events in which probe successfully fires the electron trigger. Trigger efficiency is computed as a function of electron p_T and η. However this method is not effective due to small number of Z events at high electrons p_T.

(ii) For high p_T electron events, trigger efficiency is measured from JetHT passing the PFHT800 trigger.

Electron trigger efficiencies are shown in Figure 5.3. For electron $p_T < 100$ GeV, trigger efficiency is computed by tag and probe method in Z events whereas trigger efficiency is taken from JetHT data when p_T of electron is greater than 100 GeV.

5.3.3 Photon Trigger Performance

In γ+jets control region events are selected by single photon trigger. A logical OR of two triggers Photon165 and Photon175 (p_T threshold 165 and 175 respectively) is considered. Both triggers have a loose requirement on photon H/E ratio. Trigger performance is measured in events passing the PFHT650 trigger. Further requirements include presence of a single photon in the barrel ($|\eta| <$1.4442), which passes certain identification criteria and a high p_T central jet with $p_T > 100$ GeV. Figure 5.2 shows single photon triggers efficiency as a function of hadronic recoil. A logical OR of single photon triggers with the lowest un-prescale HT trigger (EcalHT800) provides small recovery in efficiency at high recoil. The efficiency curve rises to unity except for recoil 300-600 GeV where 2-3% of loss in efficiency is observed.
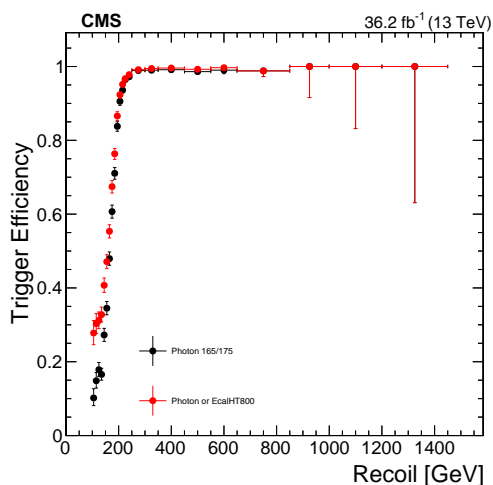
Figure 5.2: Single photon trigger efficiency computed as a function of photon p_T in single photon events. Black curve corresponds to single photon triggers, whereas red is for the combination of the single photon and EcalHT800 triggers [146].
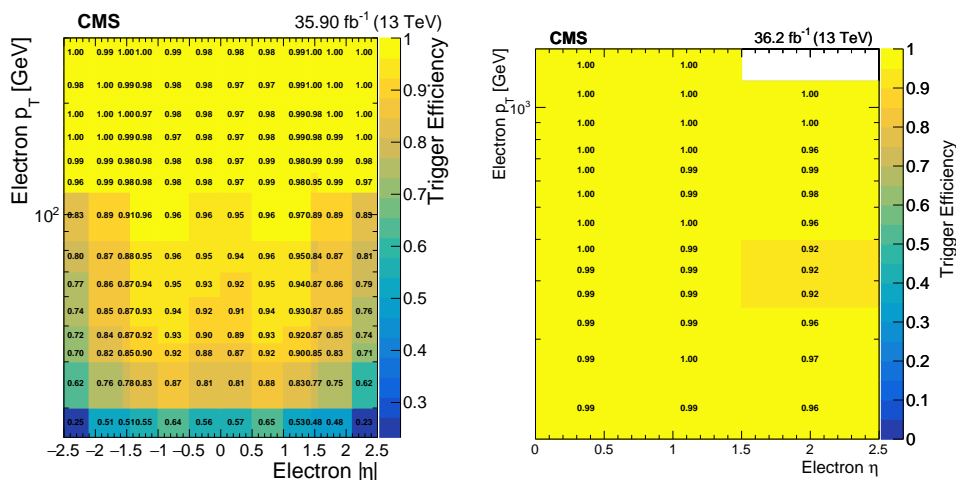
Figure 5.3: Single electron trigger efficiency as a function of electron p_T and η. The left plot shows the trigger efficiencies measured using Z tag-n-probe starting with electron p_T of 20 GeV. The right plot shows the electron trigger efficiency measured in the JetHT dataset using events passing the PFHT650 or PFHT800 trigger, starting at electron p_T of 100 GeV [146].

CHAPTER 6
PHYSICS OBJECTS

This chapter includes detailed information about all major physics objects used in current analysis. The Physics Object Group (POG) recommendations are followed mostly but for the sake of this particular analysis few selection variations are also considered. All main physics objects and corresponding selection requirements are described as follows:

6.1   Primary Vertex and Pile-up Reweighting

Generally there are several interactions appear inside the same bunch crossing, this condition is referred to as pile-up. Typically this can affect or bias the analysis results therefore pile-up reweighting is performed in order to reweight the true number of pile up interactions in MonteCarlo to match the data ones. Well-constructed events are selected by applying loose selection cuts and vertex associated to largest p_T sum of member tracks is chosen.

6.2   Jets

This analysis includes AK4 jets. The reconstruction of jets is preformed by clustering the PF candidates in an event using the anti-kt algorithm and a distance parameter of 0.4. For jet clustering, only those charged particle flow candidates are chosen which are associated with a good primary vertex. Moreover the jets are corrected with L1, L2 and L3 corrections. L1 correction is related to event-by-event energy density estimation of neutral particle from pile-up interactions. L2 corrections are applied as a function of η to equalize the jet energy response with respect to the central barrel region. L3 corrections are applied as function of transverse momentum to equalize central jet response with respect to reference objects. Lastly to match the response of jets with simulation, residual jet energy corrections are applied to jets in data.

Spring16 MC truth JECs are used to calibrate jets in simulation events and for data Sept23

re-reco residual corrections are applied.

In order to avoid soft jets the ak4 jets are required to be in central region of detector ($|\eta| < 2.5$) with $p_T > 30$ GeV. Loose jet identification recommendations are used from jet-met POG. Moreover detector noise and beam halo cleaning requirements are applied to leading ak4 jet i.e.

Charged hadronic fraction (CHF) > 0.1

Neutral hadonic fraction (NHF) < 0.8

6.3 B-tagged Jets

The identification of b jets is important to suppress the top background (both $t\bar{t}$ and single top production). The b jets are tagged using BTV POG recommended medium working point for CombinedSecondaryVertexv2 (CSVv2) tagger (> 0.80) [136]. The b jet are selected with $p_T > 20$ GeV with $|\eta| < 2.4$. b jet tagging scale factors are also applied on MonteCarlo processes as measured and recommended by the BTV group. In signal region, top background is reduced by a factor of 3.

6.4 Muons

Leading backgrounds are electroweak processes involving muons as the outgoing particles. It is crucial to veto muons in the signal region to eliminate the background contribution. Muon identification and reconstruction criteria are discussed in this section.

6.4.1 Muon Identification

Muons are required to have $p_T > 10$ GeV and $\eta < 2.4$. Real muons are identified in an event by applying certain loose selection requirements, recommended by Muon-POG [137] as follows:

- Muon reconstructed as a global or tracker muon. For global reconstruction the tracker-track is found for each standalone-muon track and combined fit is performed for

muon-detector hits and tracker. On the other hand, tracker muon reconstruction cor-
responds to tracker-track extrapolation and matching to reconstructed segments in
muon detector.

- Muon reconstructed as a particle flow muon.

- Relative isolation $\Delta\beta < 0.25$.

The isolation is calculated in a cone of radius $\Delta R = 0.4$, around the muon track while
considering the transverse momentum p_T sum of particle-flow candidates in that cone i.e.
neutral hadrons, PF photons and charged hadrons associated to the primary vertex.

Muons are subject to the tight selections in certain control regions, which are eventu-
ally used to estimate the major background in the data-driven manner. The selections are
recommended by muon-POG [138] and are listed in Table 6.1.

Object	Selection
Muon	Muon reconstructed as a global muon
	Muon reconstructed as a particle flow muon
	Normalised χ^2 of the global track less than 10
	Muon segments in at least two muon stations
	At least one muon chamber hit included in the global track fit
	Transverse impact parameter with respect to the primary vertex < 2 mm.
	Longitudinal impact parameter with respect to the primary vertex < 5 mm.
	At least one pixel hit
	Hits on at least 5 tracker layers
	Relative isolation $\Delta\beta < 0.15$

Table 6.1: Identification criteria for tight muon selection.

It is important to study how efficient the selection is and in particular to compare this
value for data and simulation. Tag and probe method is one of the common methods for
this study. In this method a well known resonance i.e. Z peak is considered and invariant
mass of an oppositely charged pair of leptons (muons in this case) is plotted. One of the
lepton is $'tag'$ while the other is $'probe'$. Tag lepton is subjected to pass tight selection to
ensure a presence of real lepton, whereas probe is selected through loose selection criteria.

Since this pair of leptons is forced to have invariant mass within Z mass window, it ensures that probe is indeed a real lepton. Then several selections are applied to probe and number of probes passing and failing gives the efficiency of the selection to find true leptons. The mass distribution of the tag-probe (passing and failing) pair in data is done separately and is subject to fit simultaneously to the Z peak. This, in turn, helps to determine the efficiency of the lepton selection which is measured for different ranges of lepton p_T, muon η and number of vertices in the event (N_{PV}). The muon selection efficiency in simulation can be obtained directly from the generator-level information. The efficiency of the selection is given by:

$$\epsilon = \frac{N_{pass}}{N_{pass} + N_{fail}} \tag{6.1}$$

here N_{pass} and N_{fail} are number of events with passing and failing probes respectively. Finally the scale factors are applied to the simulation and an overall 1% uncertainty is assigned on these scale factors. Data-to-MC scale factors for loose muon identification criteria are shown in Figure 6.1, whereas Figure 6.2 shows the tight muon identification scale factors.

6.4.2 Muon Reconstruction

During the first 21 fb^{-1} data, the tracking efficiency was highly affected by deadtime in the silicon strip sensors due to Highly Ionized Particles (HIPs), whose effect was increased by the large number of colliding bunches during 2016 data-taking. This problem has been solved for the later part of the data-taking (from Run2016G onward). HIPs are known to lower the reconstruction efficiency for both electrons and muons, as well as the b-tagging efficiency. Tag and probe technique is used to measure muon tracking efficiency in $Z(\mu\mu)$ separately for data and simulation. The efficiency is found to be reduced for low p_T muons, barrel region muons ($|\eta| < 1.5$) and muons in events with high pileup. Muon reconstruction scale factors in low and high pileup events are represented in Figure 6.3. A systematic
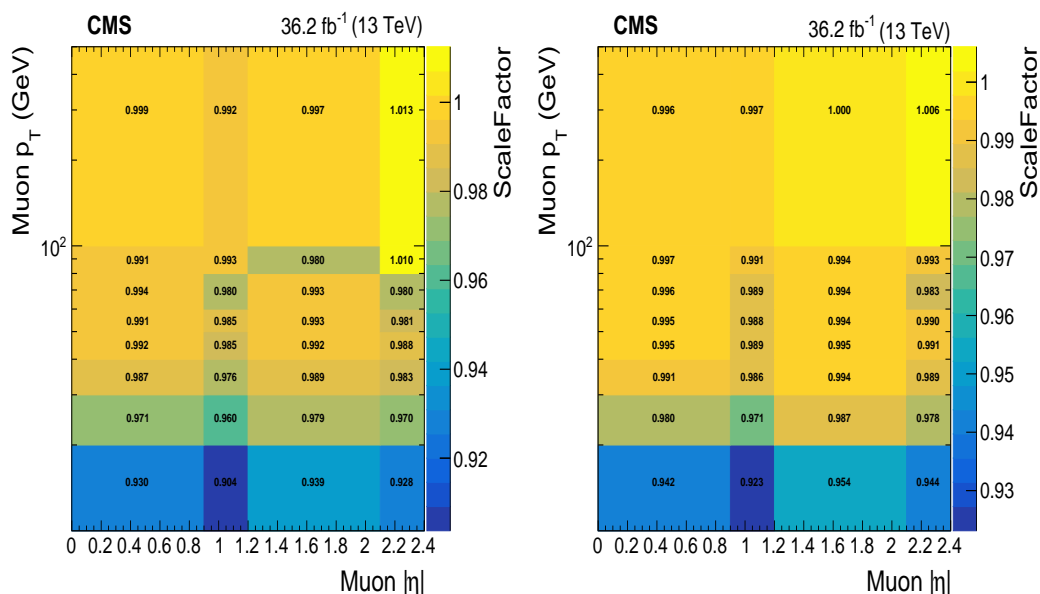
Figure 6.1: Data-MC scale factors for loose muon selection as a function of muon p_T and η with number of vertices $N_{PV} > 17$ (left) and $N_{PV} \leq 17$ (right) [137].
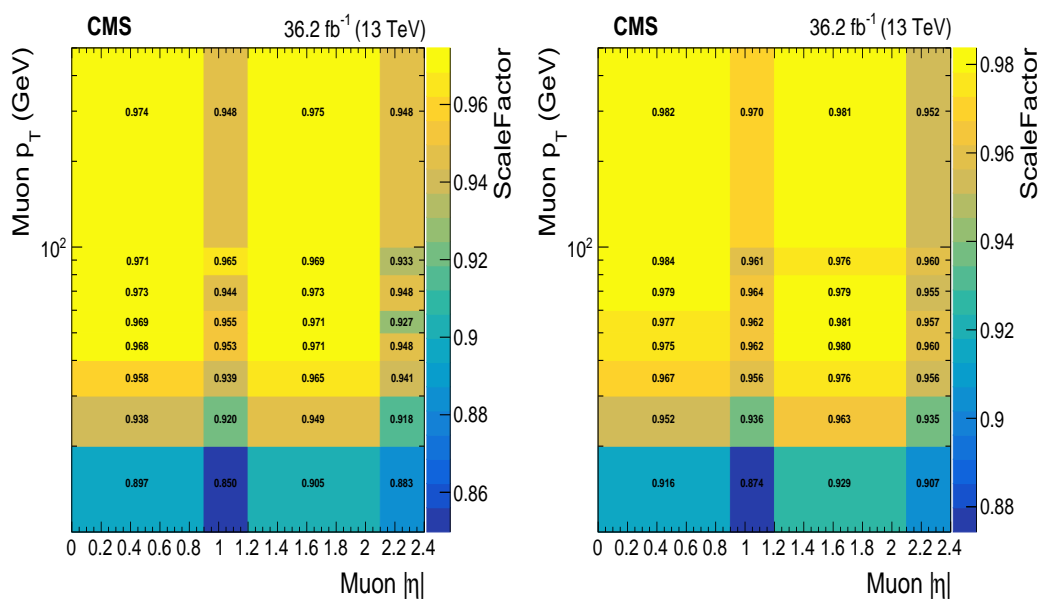
Figure 6.2: Data-MC scale factors for tight muon selection as a function of muon p_T and η with number of vertices $N_{PV} > 17$ (left) and $N_{PV} \leq 17$ (right) [138].

uncertainty of 0.5% is assigned to the scale factors.
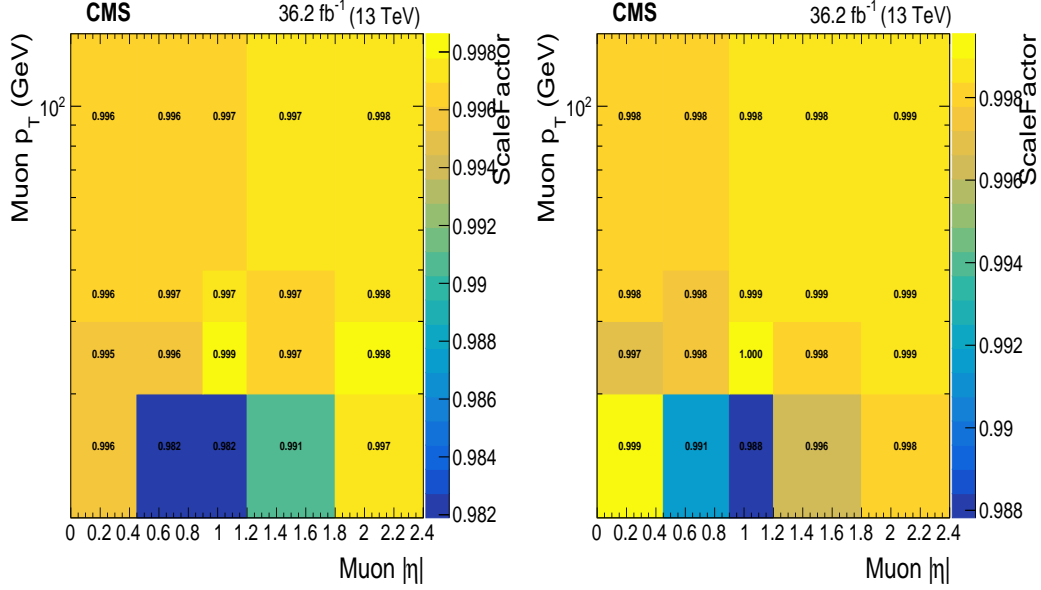
Figure 6.3: Data-MC scale factors for muon tracking efficiency as a function of muon p_T and η with number of vertices $N_{PV} > 17$ (left) and $N_{PV} \leq 17$ (right) [138].

6.5 Electrons

Electrons reconstruction and identification efficiencies are measured to study signal and control regions.

6.5.1 Electron Identification

Electrons are vetoed to suppress the $Z(\nu\nu)$+jets and $W(l\nu)$ background processes. The selection requirements are as follows:

- Electron $p_T > 10$ GeV and $|\eta| < 2.5$.

- In order to identify real electrons in an event, electrons must pass loose identification and isolation criteria, as listed in Table 6.2.

Variable	Selection in Barrel	Selection in Endcaps
Full 5x5 $\sigma_{i\eta i\eta}$	< 0.0115	< 0.0370
$|\Delta\eta_{i\eta}|$	< 0.0749	< 0.0089
$|\Delta\eta_{i\phi}|$	< 0.228	< 0.213
H/E	< 0.356	< 0.211
Relative isolation (ρ correction)	< 0.175	< 0.159
1/E - 1/p	< 0.229	< 0.150
$|d_{xy}(\text{vtx})|$	< 0.050	< 0.100
$|d_z(\text{vtx})|$	< 0.100	< 0.200
Expected Inner Missing Hits	<= 2	<= 3
Pass conversion veto	Yes	Yes

Table 6.2: Identification criteria for loose electron selection.

Electron based control regions, i.e. $W(e\nu)$ and $Z(ee)$, play crucial role in estimation of leading electroweak background processes. Such electrons are required to pass a tighter identification and isolation selection as provided in Table 6.3.

Variable	Selection in Barrel	Selection in Endcaps
Full 5x5 $\sigma_{i\eta i\eta}$	< 0.00998	< 0.0292
$|\Delta\eta_{i\eta}|$	< 0.00308	< 0.00605
$|\Delta\eta_{i\phi}|$	< 0.0816	< 0.0394
H/E	< 0.0414	< 0.0641
Relative isolation (ρ correction)	< 0.0588	< 0.0571
1/E - 1/p	< 0.0129	< 0.0129
$|d_{xy}(\text{vtx})|$	< 0.050	< 0.100
$|d_z(\text{vtx})|$	< 0.100	< 0.200
Expected Inner Missing Hits	<= 2	<= 1
Pass conversion veto	Yes	Yes
Ecal PF cluster isolation	-	-
Hcal PF cluster isolation	-	-
Tracker isolation	-	-
χ^2/ndf	-	-

Table 6.3: Identification criteria for tight electron selection.

Tag and probe method is used to find electron selection efficiency in $Z(ee)$ events. The respective scale factors are taken from e-gamma POG covering the whole 2016 data taking period and defined with respect to Summer-16 MC [139]. The scale factors for loose (left) and tight (right) electron ID in probe electron transverse momentum p_T - η plane are shown in Figure 6.4.
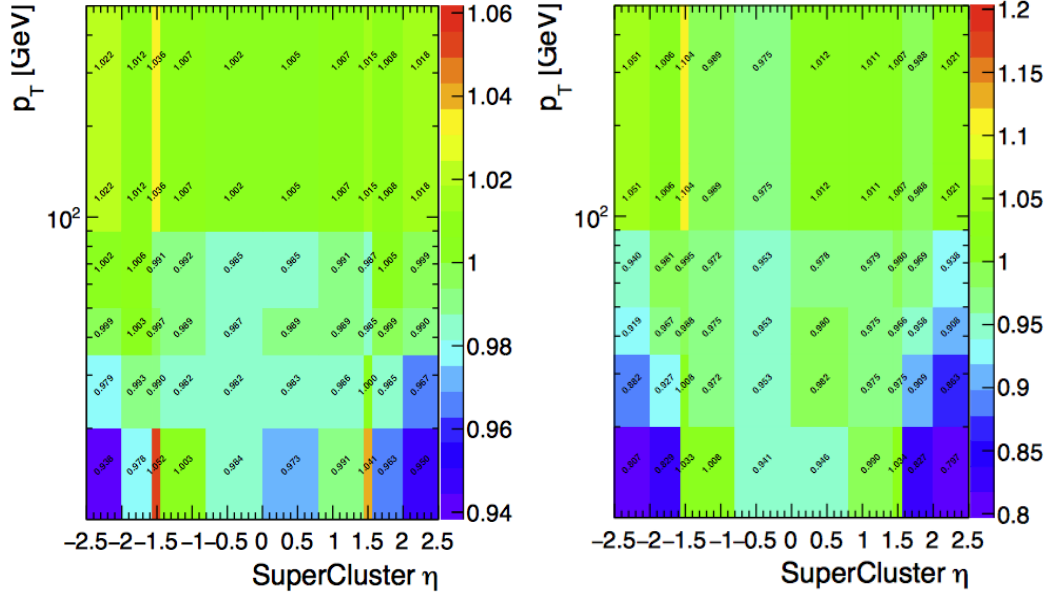
Figure 6.4: E-Gamma POG recommended data-MC scale factors for electron loose (left) and tight (right) identification criteria . [139]

6.5.2 Electron Reconstruction

Electron reconstruction scale factors are computed using tag and probe technique and are shown as a function of probe p_T and η in Figure 6.5. A 1% systematic uncertainty is assigned on the electron selection efficiency as recommended by POG.

6.6 Tau

Tau leptons are vetoed in this analysis to reject the electroweak background. Following loose selection criteria is used to identify taus.

- Transverse momentum p_T of tau should be greater than 18 GeV and $|\eta| < 2.3$.

- New DecayModeFinding.

- To identify the tau leptons, MVA based tau isolation discriminator is recommended by TAU POG . This discriminator is a very loose MVA isolation working point labelled as "byVLooseIsolationMVArun2v1DBnewDMwLT" [140].

Sometimes electrons and muons can be misidentified as taus, in order to minimize such fake contribution, electron and muon rejection vetos are applied. Since the leptons veto is already applied as a baseline selection in our analysis therefore these vetos are removed from the tau-id.
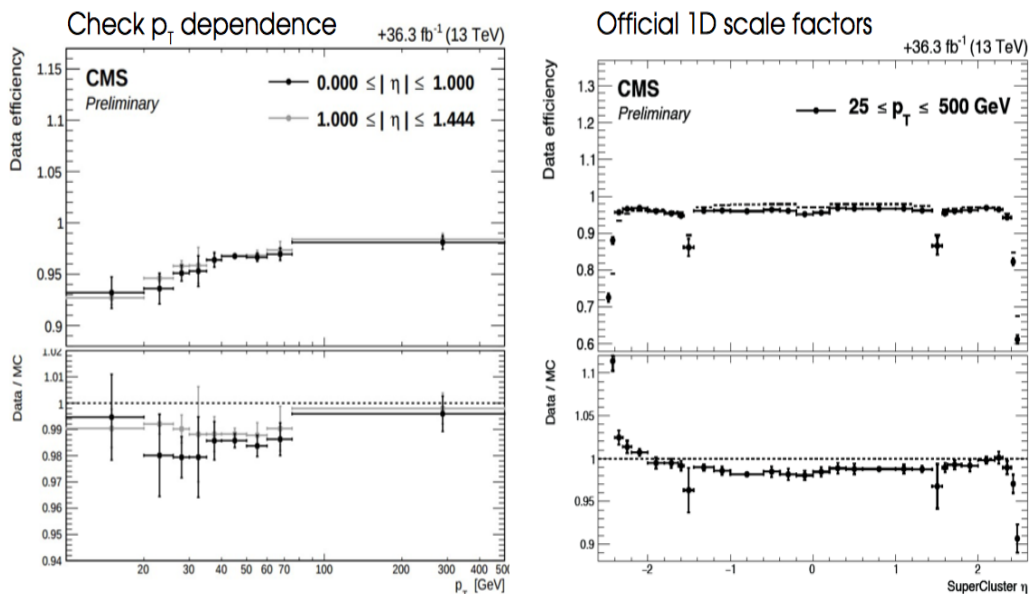
Figure 6.5: E-Gamma POG recommended data-MC scale factors for electron loose (left) and tight (right) identification criteria . [139]

6.7 Photons

Mono-photon is a search for missing transverse energy plus a photon jet in final state. Our analysis requires photon veto to seperate monojet search from mono-photon and also to suppress $Z(\nu\nu) + \gamma + jets$ and $W(\mu\nu) + \gamma + jets$ backgrounds. Following are the requirements for photon veto:

- Photon $p_T > 15$ GeV and $|\eta| < 2.5$.

- photons must pass loose identification criteria as listed in Table 6.4.

Variable	Selection in Barrel	Selection in Endcaps
Full 5x5 $\sigma_{i\eta i\eta}$	< 0.0103	< 0.0301
H/E	< 0.0597	< 0.0481
charged hadron isolation	< 1.295	< 1.011
neutral hadron isolation	$< 10.92 + 0.0148 \times p_T + 1.7 \times 10^{-5} \times p_T^2$	$< 5.931 + 0.0163 \times p_T + 1.4 \times 10^{-5} \times p_T^2$
photon isolation	$< 3.630 + 0.0053 \times p_T$	$< 6.541 + 0.0034 \times p_T$
Conversion safe electron veto	Yes	Yes

Table 6.4: Identification criteria for loose photon selection.

Following are the requirements for photon selection in $\gamma+$ jets control region (to estimate electroweak contribution).

- Photon $p_T > 175$ GeV and $|\eta| < 2.5$ (to maintain high purity of $\gamma+$jets sample).

- photons must pass tighter identification criteria as listed in Table 6.5.

Variable	Selection (Barrel)
Full 5x5 $\sigma_{i\eta i\eta}$	< 0.0102
H/E	< 0.0396
charged hadron isolation	< 0.441
neutral hadron isolation	$5.931 + 0.0163 \times p_T + 1.4 \times 10^{-5} \times p_T^2$
photon isolation	$2.571 + 0.0034 \times p_T$
Conversion safe electron veto	Yes

Table 6.5: Identification criteria for tight photon selection.

Tag and probe method is used to calculate photon selection efficiency in Z boson decay. The electrons are treated as photon, by ignoring the matching requirements between the ECAL supercluster and the track. Data-MC scale factors for photon identification and isolation are measured by E-Gamma POG and are given as a function of probe photon p_T and η in Figure 6.6. A 2% systematic uncertainty is assigned on the photon selection efficiency.
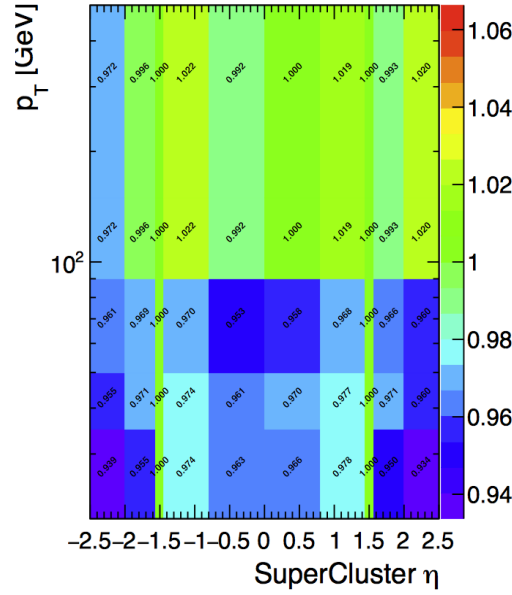
Figure 6.6: E-Gamma POG recommended data-MC scale factors for photon identification and isolation. [141]

6.8 Missing Transverse Energy

Missing transverse energy is the energy imbalance in the plane transverse to the colliding proton beams. This imbalance can be caused by several reasons as follows:

- particles escape through the detector unnoticed.

- detector effects can cause noise.

- effect of beam halo, cosmics and pile-up.

Missing transverse energy is calculated as a negative vector sum of p_T of all reconstructed particle flow candidates in an event i.e. of

$$\not{E}_T = \sum_i p_T^i$$

Type-1 $\not{E}_T$ corrections are carried out as projection of jet energy correction. Control regions are backgrounds to estimate the leading electroweak contribution ($W(l\nu)$+jets and

$Z(\nu\nu)$+jets), which are constructed by selecting either a lepton, pair of leptons or a single photon. The hadronic recoil against the boson is calculating by excluding the leptons and photons p_T from the missing transverse energy computation for dilepton, single lepton and single photon control regions as follows:

$$\bar{U} = \not{E}_T + \overrightarrow{p}_T^{ll,l,\gamma} \tag{6.2}$$

6.8.1 Noise Filters

There can be various sources for large fake $\not{E}_T$ in an event such as detector noise, cosmic rays, and beam-halo particles which mimic single like events as described earlier in this section. A number of filters are recommended by the JetMet POG [135] to remove such events. Following is the list of these filters.

- Good Vertex Filter, (at least one good primary vertex in the event is required.)

- HBHE Noise Filter.

- HBHEIso Noise Filter.

- EE Bad SC Filter.

- 2016 Global Halo Filter.

- ECAL Dead Cell Trigger Primitive Filter.

- Updated Bad Muon Filter.

- Updated Bad Charged Hadron Filter.

In addition to these filters some other precautions are also carried out to suppress the anomalous $\not{E}_T$ events as follows:

- Since the recoil is computed by removing muon p_T contribution from $\not{E}_T$ therefore the analysis is not directly effected by fake $\not{E}_T$ events induced by extra or fake muons.

- further cleaning is done by applying loose muon veto in signal and control regions.

- Difference between calorimeter $\not{E}_T$ and PF $\not{E}_T$ is computed relative to recoil. For mismeasured PF $\not{E}_T$, this ratio has large value (close to 1) and by applying a cut on this variable, we can reduce the fake tracks events i.e. $|\not{E}_T^{calo} - \not{E}_T^{PF}|/U$<0.5.

CHAPTER 7

ANALYSIS

7.1 Monte Carlo Reweighting

In order to match its predictions to data, Monte Carlo simulation is corrected by applying a number of weights and corrections.

7.1.1 Pileup Reweighting

Generally MC simulation has different pile-up conditions than data and to match generic MC distribution to one specific to data pile-up reweighting is applied. The scale factors are measured by matching the observed number of reconstructed vertices in $Z(\mu\mu)$ events.

7.1.2 Trigger Efficiency

MC simulation is corrected with respect to L1+HLT trigger efficiency. Trigger efficiency is computed for several triggers directly in data. Several triggers are used in this analysis and respective efficiencies are described in Section 5.3. The measured efficiency is applied as a weight per event in MC simulation.

7.1.3 Lepton and Photon Efficiency and Reconstruction Scale Factors

Five control regions are defined in this analysis namely dimuon, dielectron, single muon, single electron and single photon CR. Data-to-MC scale factors are calculated as a ratio of lepton(photon) selection efficiency in several control region. These scale factors are then applied to correct the MC yield.

7.1.4 NLO Corrections

More than 90% background contribution comes from electroweak processes (W+jets and Z+jets). These processes along with (γ+jets) serve as control regions for this analysis.

These MC samples are produced at Leading Order (LO) in H_T bins. We apply Next to Leading Order (NLO) corrections to these background processes as event-by-event weights to LO samples. The key factor is to match generator level p_T distribution of Z, W and γ to the corresponding NLO predictions.

- For W and Z cases large simulation samples are generated by employing aMC@NLO. The number of partons are varied between 0-2 at NLO in QCD and matched to PYTHIA 8.2 parton shower through FxFx algorithm [142].

- For $\gamma+1$ jets , sample is generated with aMC@NLO followed by PHYTHIA 8.2 showering. In this case no additional parton is generated at born level [143].

- NNPDF 3.0 in 5-flavor scheme has been used as the parton distribution function (PDF) set for all samples.

Basic monojet selection are applied to generator level objects and and post shower p_T distributions for NLO and LO Monte Carlo samples are compared. This NLO to LO ratio is used as k-factor as a function of p_T and is applied to LO MC simulations. Further electroweak k-factors are also applied to incorporate the decrease in the cross section at high p_T due to higher order electroweak effects [144] [145]. Base MC, QCD NLO and QCD+EW NLO comparison, in terms of p_T distribution, is shown in Figure 7.1.
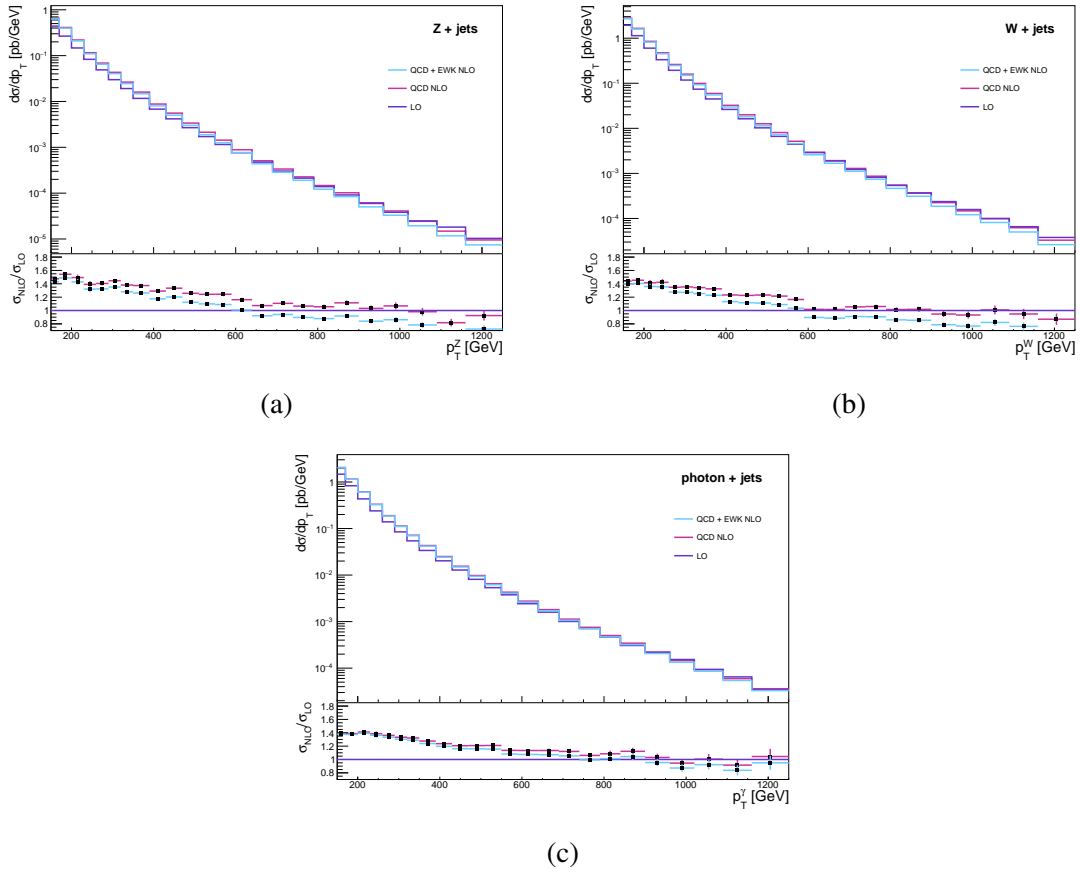
Figure 7.1: NLO Higher-order corrections on the Z (a), W (b), and γ (c) p_{T} distributions [146].

7.2 Event Selection

This section includes the set of criteria, used to select events in signal region and CR. There are five CR in this analysis, which are used to estimate the main electroweak background processes and are listed in Table 7.1. The data events are required to pass the respective triggers in all the regions as described in the Table 5.4. In oder to reduce events with fake $\not{E}_T$ due to detector noise and beam halo background, the events must pass several $\not{E}_T$ filters as mentioned in section 6.8.1.

A base-line set of selections is applied to signal and all the CR regions e.g. selections for primary vertex, noise cleaning and leading jet p_T and η. In order to avoid QCD background,

a cut on $\Delta\phi$ between leading jet and $\not{E}_T$ is applied, moreover fake track events cleaning is also carried out. The base-line criteria is followed by the specific selection requirements, depending on each individual region. Table 7.2 represents a summary of the event selection used in this analysis.

CR	Estimated Background
Single Muon	$W(l\nu)$ + jets
Single Electron	
Double Muon	
Double Electron	$Z(\nu\nu)$ + jets
Single Photon	

Table 7.1: List of all Control Regions to estimate the irreducible electroweak background.

Section 7.2.1 shows comparison between data and MC for hadronic recoil distribution in all the regions. For signal region, recoil is just the $\not{E}_T$ whereas for control regions, lepton(s)/photon p_T is removed from the $\not{E}_T$ computation. An overall good agreement is seen for all the regions.

Several kinematic distributions like jet multiplicity, leading jet and leptons/photon p_T and η are shown in Appendix B.

dataset name		Signal	μμCR	μCR	eeCR	eCR	γCR
		MET	MET	MET	single-e	single-e	single-γ
primary vertex		apply	apply	apply	apply	apply	apply
noise cleaning		apply	apply	apply	apply	apply	apply
leading jet	$P_T > 100$ GeV, $|\eta| < 2.5$	apply	apply	apply	apply	apply	apply
$\Delta\phi$ (Jet,E_T^{miss})	$\Delta\phi > 0.5$	apply	apply	apply	apply	apply	apply
Fake track events cleaning	$|\not{E}_T^{calo} - \not{E}_T^{PF}|/U < 0.5$	apply	apply	apply	apply	apply	apply
photon (tight)	$P_T > 175$ GeV, $|\eta| < 2.5$	veto	-	-	-	-	apply
photon (loose)	$P_T > 15$ GeV, $|\eta| < 2.5$	veto	-	-	-	-	-
electron (tight)	$P_T > 40$ GeV, $|\eta| < 2.5$	veto	-	-	apply	apply	-
electron (loose)	$P_T > 10$ GeV, $|\eta| < 2.5$	veto	-	-	apply	-	-
muon (tight)	$P_T > 10$ GeV, $|\eta| < 2.5$	veto	apply	apply	-	-	-
muon (loose)	$P_T > 10$ GeV, $|\eta| < 2.5$	veto	apply	-	-	-	-
tau	$P_T > 18$ GeV, $|\eta| < 2.3$	veto	veto	veto	veto	veto	veto
b-jet	$P_T > 20$ GeV, $|\eta| < 2.4$	veto	veto	veto	veto	veto	veto
M(μμ) or M(ee)	$60 < \text{M} < 120$ GeV	-	apply	-	apply	-	-
$M_T(\mu\nu)$, $M_T(e\nu)$	$M_T < 160$ GeV	-	-	apply	-	apply	-
$\not{E}_T$	$\not{E}_T > 50$ GeV	-	-	-	-	apply	-
Recoil(U)	$U > 250$ GeV	apply	apply	apply	apply	apply	apply

Table 7.2: Summary of the events' selection in signal region and all CR, used in this analysis.

95

7.2.1   Recoil Distribution in Signal and Control Regions
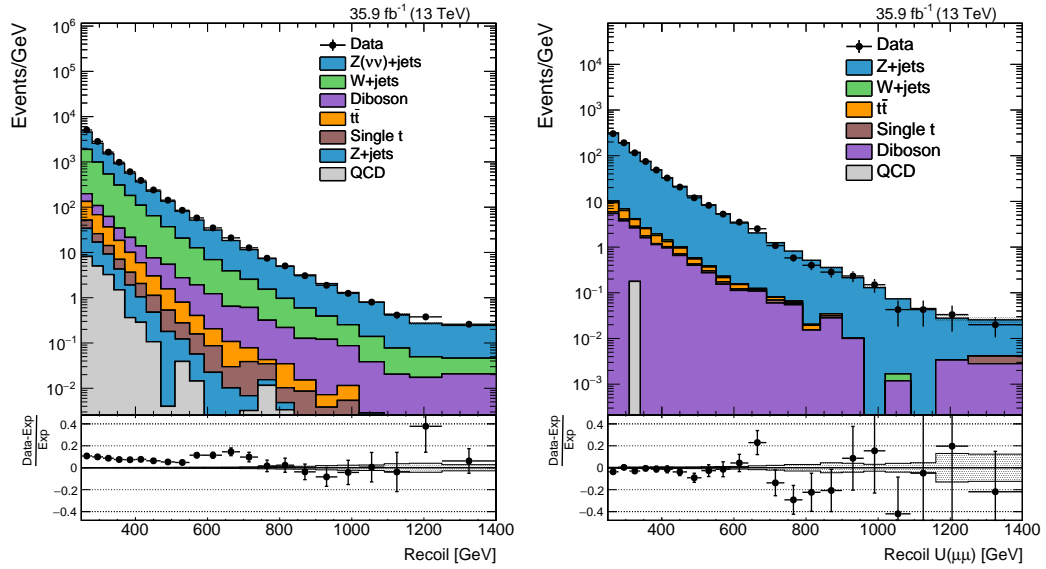
(a)

(b)
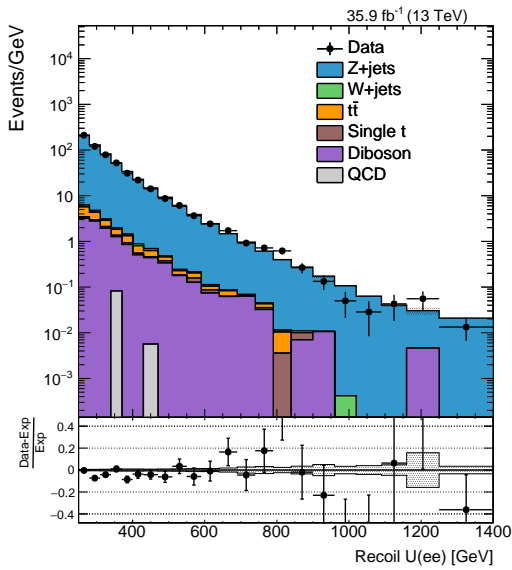
(c)

Figure 7.2: Comparison between data and Monte Carlo simulation for recoil distribution in the (a) signal region, (b) dimuon CR and (c) double electron CR. Overall good agreement is observed.
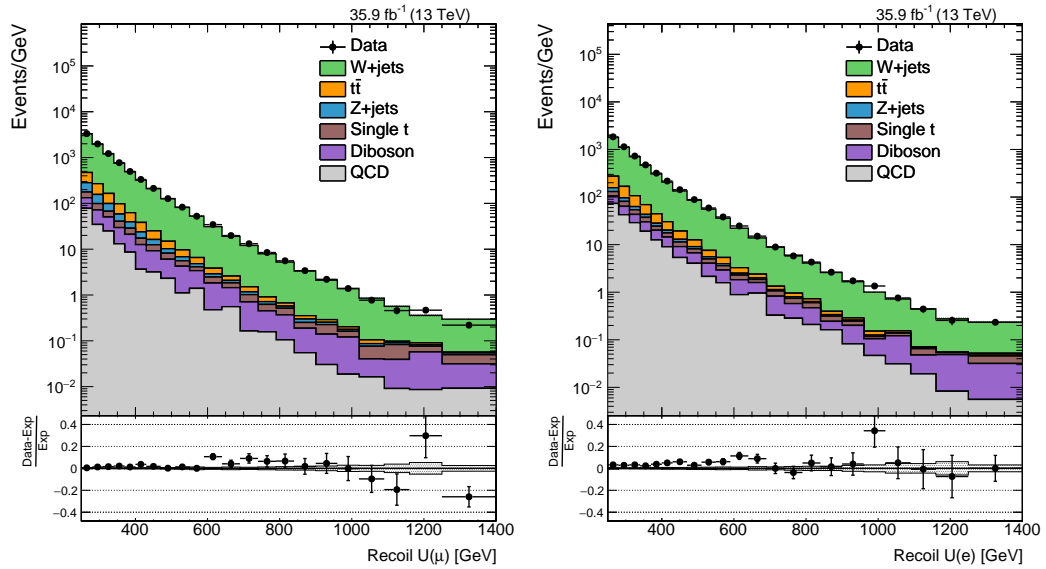
(a)

(b)
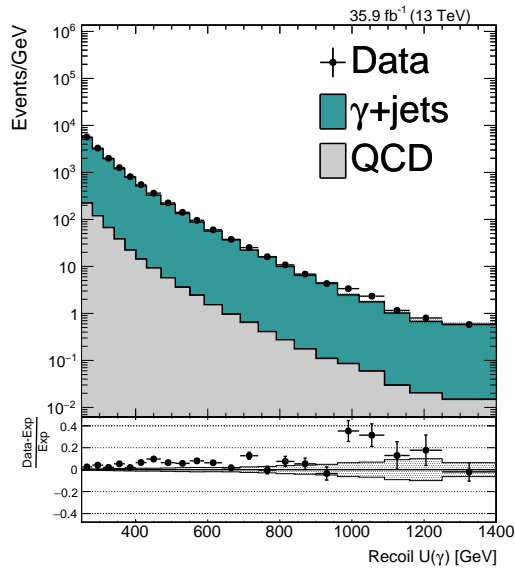
(c)

Figure 7.3: Comparison between data and Monte Carlo simulation for recoil distribution in the (a) single muon CR, (b) single electron CR and (c) single photon CR. Overall good agreement is observed.

7.3   Electroweak Background Estimation

A combined maximum likelihood fit of the signal region and five control regions is used to estimate $Z \to \nu\nu$+jets and $W \to l\nu$+jets rate in each $\not{E}_T$ bin. Table 7.3 shows several CR and respective backgrounds to be estimated. Various uncertainties are used in this fit.

- Systematic uncertainties

- Shape uncertainties: theory uncertainties (e.g. QCD scale, PDF, NLO-EW k-factor) on the cross section estimation. Uncertainties due to reconstructed objects such as jets energy scale and resolution.

- Normalized uncertainties: leptons and photon reconstruction uncertainties in control regions as well as uncertainty on b-jet veto. Luminosity and cross-section uncertainties for MC-driven backgrounds.

7.3.1   Combined Maximum Likelihood Fit Procedure

First step is to compute the recoil U in all the control regions by removing either the photon, the muons or electrons from the $\not{E}_T$ calculation. Next step is to calculate the transfer factors (R), which are derived from simulation and used to link the yields of the $Z \to ll$+jets, $W \to l\nu$+jets and γ+jets processes in the control regions with the $Z \to \nu\nu$+jets and $W \to l\nu$+jets background estimates in the signal region. These transfer factors are defined as the ratio of expected yields of the target process in the signal region and the process being measured in the control sample. Following is the expression for transfer factor computed as ratio of yields in dimuon $Z(\mu\mu)$ CR to $Z(\nu\nu)$ background.

$$R_i^Z = \frac{Z \to \mu^+\mu^- \ events \ in \ i^{th} \ bin \ of \ recoil}{Z \to \nu\nu \ events \ in \ i^{th} \ bin \ of \ recoil} \tag{7.1}$$

Other transfer factors are calculated in the similar manner. The expected number of $Z \to \nu\nu$+jets events in each bin of $\not{E}_T$ are the free parameters of the fit. For better estimation,

$Z \rightarrow \nu\nu$ in the signal region is also connected to the $W \rightarrow l\nu$ in the same region. Maximum likelihood function is given is equation 7.2.

CR	Estimated Background
Dimuon ($Z \rightarrow \mu^+\mu^-$)	$Z \rightarrow \nu\nu$
Dielectron ($Z \rightarrow e^+e^-$)	$Z \rightarrow \nu\nu$
Single Photon (γ+jets)	$Z \rightarrow \nu\nu$
Single Muon ($W \rightarrow \mu^+\nu^-$)	$W \rightarrow l\nu$
Double Muon ($W \rightarrow e^+\nu^-$)	$W \rightarrow l\nu$

Table 7.3: List of CR to estimate major electroweak backgrounds

$$
\begin{aligned}
\mathcal{L}_c(\beta^{Z \rightarrow \nu\nu}, \beta, \theta) = & \prod_i \text{Poisson}\left(d_i^\gamma | B_i^\gamma(\theta) + \frac{\beta_i^{Z \rightarrow \nu\nu}}{R_i^\gamma(\theta)} \right) \\
& \times \prod_i \text{Poisson}\left(d_i^Z | B_i^Z(\theta) + \frac{\beta_i^{Z \rightarrow \nu\nu}}{R_i^Z(\theta)} \right) \\
& \times \prod_i \text{Poisson}\left(d_i^W | B_i^W(\theta) + \frac{f_i(\theta)\beta_i^{Z \rightarrow \nu\nu}}{R_i^W(\theta)} \right) \\
& \times \prod_i \text{Poisson}\left(d_i | B_i(\theta) + (1 + f_i(\theta))\beta_i^{Z \rightarrow \nu\nu} + \beta S_i(\theta) \right) \quad (7.2)
\end{aligned}
$$

where, $d_i^{\gamma/Z/W}$ = number of events observed in i bin of recoil in each of the CR i.e. photon, dimuon(dielectron) and single-muon(single-electron) CR.

$B_i^{\gamma/Z/W}$ = number of events for background processes in the respective CR.

$\beta_i^{Z \rightarrow \nu\nu}$ = a freely floating parameter and corresponds to the $Z \rightarrow \nu\nu$ background yield in i recoil bin in the signal region.

$R_i^{\gamma/Z/W}(\theta)$ = transfer factor for each CR and θ represents systematic uncertainties appearing as additive perturbations to the transfer factors.

$f_i(\theta)$ = transfer factor between $Z \rightarrow \nu\nu$ and $W \rightarrow l\nu$ in the signal region.

$B_i(\theta)$ = all backgrounds in signal region.

$S_i(\theta)$ = nominal signal predictions.

β = signal strength, a freely floating parameter in fit.

7.3.2   Transfer Factors

The dominant background in the monojet final state comes from the $Z \to \nu\nu$ production. This background is analogous to the dark matter final state when a boson decays into invisible particles. The only means we have of discriminating against this particle is to identify characteristic features of the initial state radiation, that are different between the boson and the dark matter production.

To model the Z boson background, three control regions (dimuon, double electron and single photon) are used as listed in table 7.3. The background prediction in the signal region is associated to the dimuon and double electron control regions in data through transfer factors defined in regions of recoil, and computed using simulation that account for the difference in $Z \to \nu\nu$ and $Z \to ll$ branching ratios and also the effect of lepton acceptance and selection efficiency. The dimuon control region contains a clean Z boson signature with similar acceptances to the $Z \to \nu\nu$ background, the production mode and kinematics in the control region are very similar to the signal region. However, the dimuon control region contains roughly 1/10 the number of Z boson events in the signal region. This limited knowledge of statistics is not sufficient to estimate the Z background in signal region properly therefore dielectron CR, which is analogous to dimuon CR, is used in the estimation process. Dimuon transfer factor is of the order of 9 (Figure 7.4(a)), implying that with the dimuon control region alone, the analysis is systematically limited to an uncertainty 3 times worse than the statistical precision of the analysis. The transfer factor for double electron CR varies from 13 to 9 for low to high recoil as shown in Figure 7.4(b). In this case, transfer factors also account for the difference in efficiencies of the electron and $\not{E}_T$ triggers.

To improve the small constraining power of the dilepton control regions, single lepton (mainly $W \to l\nu$) and γ+jets events are used to further restrict the $Z \to \nu\nu$ background. The production cross-section of $W \to l\nu$ is about the same as of $Z \to \nu\nu$ and adding these two control regions reduces the impact of the limited statistical power of dilepton events. However, additional theoretical systematic uncertainties are introduced while extrapolating

from the single lepton and γ+jets control regions to the signal region.

Single photon CR provides the dominant constraint on the high p_T $Z \rightarrow \nu\nu$ due to its large yield even at high boson p_T. The respective transfer factor takes into account the difference in the cross sections of the γ+jets and $Z \rightarrow \nu\nu$ processes, the effect of photon acceptance and efficiency, and the difference in the efficiencies of the photon and $\not{E}_T$ triggers. Since the production cross-section of γ+jets is roughly 2 times that of the $Z \rightarrow \nu\nu$ therefore transfer factor is about double of the $Z \rightarrow \nu\nu$ yield in this case (Figure 7.4(c)).

The $W \rightarrow l\nu$ process is second largest background which results from leptonically decaying W bosons where the lepton either falls out of the acceptance or is not reconstructed. This background is estimated by single-muon and single-electron control regions when lepton doesn't pass the lepton selection or gets lost in the detector. In both single-muon and single-electron cases, the transfer factor is less than 1 for $U > 300$ GeV as shown in Figure 7.5(a)(b).

$W \rightarrow \mu\nu$ background is also used to estimate the irreducible $Z \rightarrow \nu\nu$ background in the signal region and respective transfer factor is shown in Figure 7.5(c). Larger statistical power of $W \rightarrow l\nu$ background makes it possible to experimentally constrain $Z \rightarrow \nu\nu$ production at high $\not{E}_T$.

(a)

(b)

(c)
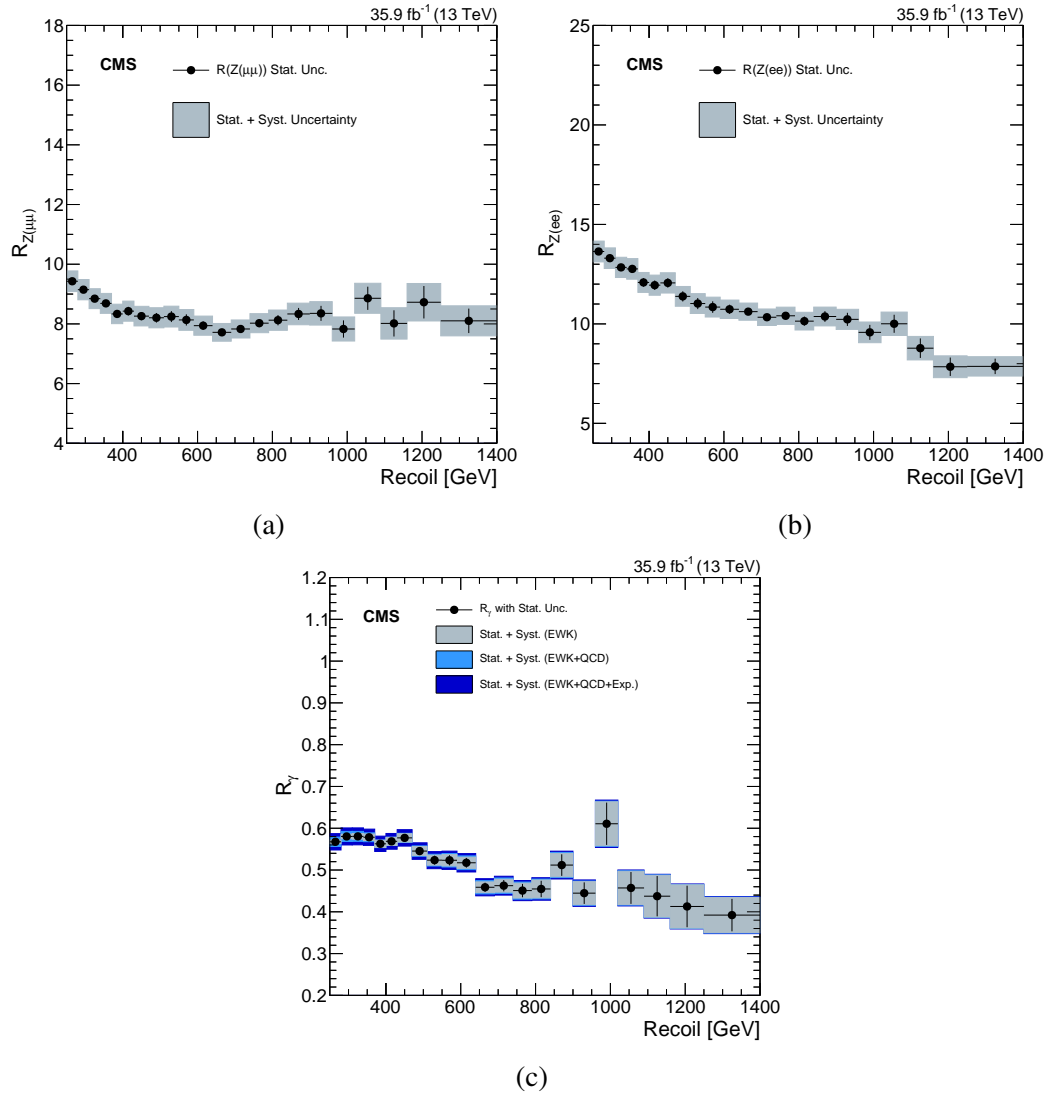
Figure 7.4: Transfer factors as a function of recoil U for $Z \to \nu\nu$ background estimation in dimuon (a), dielectron (b) and single photon (c) CR [146].

(a)

(b)

(c)
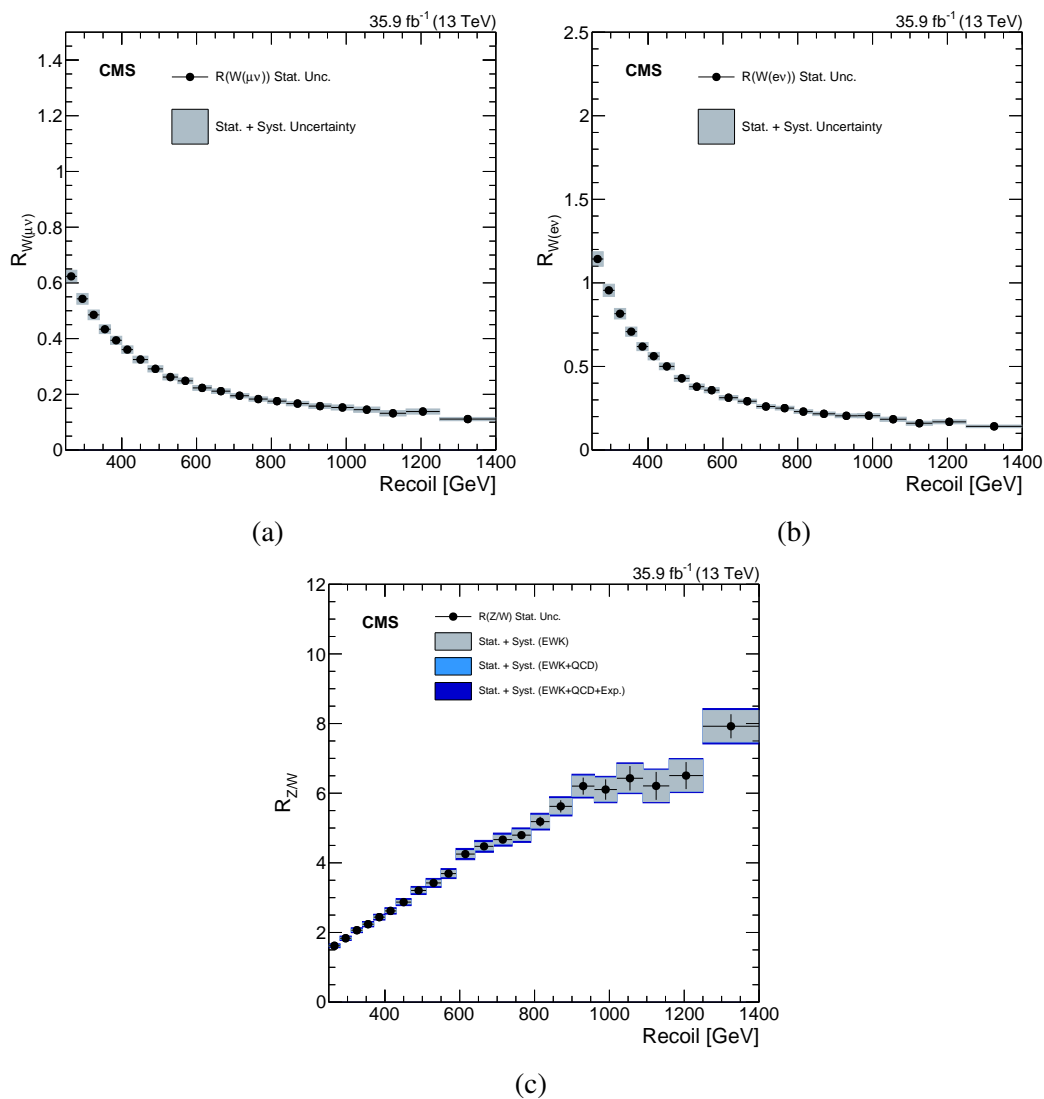
Figure 7.5: Transfer factors as a function of recoil U for $Z \to \nu\nu$ background estimation in single-muon (a) and single-electron (b) CR. Transfer factors from $W \to \mu\nu$ is shown in (c) [146].

7.3.3 Experimental Uncertainties on TFs

Uncertainty coming from lepton veto is the only experimental uncertainty on Z/W ratio in signal region. Transfer factors are not affected by systematics due to jet energy scale and jet energy resolution as the hadronic content of event is almost same for signal and control regions and eventually get cancelled in ratio calculations of electroweak processes. Experimetal uncertainties are given in Table 7.4. Since there was some inefficiency noticed at the HLT-level in the PF-muon assignment therefore a conservative systematic uncertainty is assigned to all transfer factors, computed by taking full difference between $\not{E}_T$ trigger turn-ons measured in double and single muon events. The variation in uncertainty is found to be 2% at $\not{E}_T = 250$ GeV to few per-mille for $\not{E}_T > 500$ GeV.

Source	Process	Uncertainty
$\not{E}_T$ trigger	$W_{SR}/W_{e\nu}, W_{SR}/W_{\mu\nu}, Z_{\nu\nu}/Z_{ee}, Z_{\nu\nu}/Z_{\mu\mu}, Z_{\nu\nu}/\gamma$	shape vs $\not{E}_T$
Electron trigger	$W_{SR}/W_{e\nu}, Z_{\nu\nu}/Z_{ee}$	1 %
Photon trigger	$Z_{\nu\nu}/\gamma$	1 %
μ reconstruction efficiency	$W_{SR}/W_{\mu\nu}, Z_{\nu\nu}/Z_{\mu\mu}$	1 % (per leg)
μ identification efficiency	$W_{SR}/W_{\mu\nu}, Z_{\nu\nu}/Z_{\mu\mu}$	1 % (per leg)
e reconstruction efficiency	$W_{SR}/W_{e\nu}, Z_{\nu\nu}/Z_{ee}$	1 % (per leg)
e identification efficiency	$W_{SR}/W_{e\nu}, Z_{\nu\nu}/Z_{ee}$	2 % (per leg)
γ identification efficiency	$Z_{\nu\nu}/\gamma$	2%
μ veto	$W_{SR}/W_{e\nu}, W_{SR}/W_{e\nu}, Z/W$	shape vs $\not{E}_T$
e veto	$W_{SR}/W_{e\nu}, W_{SR}/W_{e\nu}, Z/W$	shape vs $\not{E}_T$
τ veto	$W_{SR}/W_{e\nu}, W_{SR}/W_{e\nu}, Z/W$	shape vs $\not{E}_T$

Table 7.4: Experimental uncertainties on transfer factors to estimate major electroweak background in signal region [146].

7.3.4 Theoretical Uncertainties on TFs

QCD higher order corrections and electroweak (EW) corrections appear as additive perturbation to all the transfer factors. PDF uncertainty is evaluated from re-weighted NLO QCD samples, where weights are calculated at generation level with each one unit of variation of the eigenvectors of the PDF fit. Reweighted p_T distributions and thus the transfer factors are produced for each eigenvector variation, the RMS of the transfer factor variation is taken as the PDF uncertainty. NLO reweighting is done using following formula.

$$\frac{d\sigma_{\text{NLO}}}{dp_{\text{T}}^V}(\vec{\varepsilon}_{\text{QCD}}, \varepsilon_{mix}, \vec{\varepsilon}_{\text{EW}}) = [\kappa_{\text{NLO,QCD}}(\vec{\varepsilon}_{\text{QCD}}) \cdot (1 + \kappa_{\text{EW}}(\vec{\varepsilon}_{\text{EW}})) + \varepsilon_{mix} \cdot \delta\kappa_{mix}] \times \frac{d\sigma_{\text{LO}}}{dp_{\text{T}}^V}(\vec{\mu_0})$$

(7.3)

where

- $\kappa_{\text{NLO,QCD}}(\vec{\varepsilon}_{\text{QCD}})$ = NLO-QCD k-factor as a function of nuisances parameters ($\vec{\varepsilon}_{\text{QCD}}$). It includes:

  - renormalization and factorization uncertainties.

  - QCD shape uncertainty.

  - process dependent uncertainty given as a difference between the NLO k-factor of each of Z+jets, W+jets and γ+jets processes with respect to NLO k-factor of $Z \rightarrow ll$+jets.

  All these nuisance parameters must be considered as fully correlated across $\not{E}_T$ bins, as well as across different processes (Z, W, g).

- $\kappa_{\text{EW}}(\vec{\varepsilon}_{\text{EW}})$ = NLO-EW corrections parameterized as:

  - corrections for virtual production and photon and quark bremsstrahlung.

  - NNLO Sudakov corrections for missing NNLO effects (which are not absorbed in NLL) and unknown Sudakov logs in the perturbation expansion beyond NNLO. It also includes uncertainty due to the Sudakov approximation calculated as a difference between the NLL Sudakov approximation and full NLO-EW corrections.

- ε_{mix} = combination of NLO-QCD and NLO-EW corrections and $\delta\kappa_{mix}$ = uncertainty due to non factorized EW-QCD effects.

The variation in several uncertainties for W/Z transfer factors as a function of recoil is shown in Appendix C. QCD-NLO process dependent uncertainties have the largest values, varying from 1.5-0.5% while PDF and QCD-EW mixing nuisances show negligible effect. The effect of above mentioned all three Sudakov uncertainties is large at higher values of boson p_T and can reach up to 2% each.

The nuisances on Z/γ ratio are also summarized in Appendix C. Process dependent QCD-NLO uncertainties are dominant, changing from -2% for hadronic recoil < 400 GeV to +2% for larger values. Identical alternate sign of uncertainties is seen for QCD-NLO renormalization and factorization scale and shape nuisances, but the effect is small. QCD-EW mixing is negligible for the whole range of recoil.

7.3.5 Systematic uncertainties on minor backgrounds

Systematic uncertainties considered on minor backgrounds are taken directly from simulation (e.g. single-top, $t\bar{t}$ and dibosons) or from data (e.g. QCD multi-jets). The uncertainty arising from electron and photon triggers is utmost 1% while leptons/photon reconstruction and identification uncertainty is 1-2%. On the other hand, b-jet veto uncertainty is taken as 6% for top in all regions and for remaining backgrounds it is as large as 2%. Normalization uncertainties on sub-dominant processes are within 10-20%. Table 7.5 summarizes all the systematics on minor backgrounds.

7.3.6 Validation in Data

The quality of NLO-QCD and NLO-EW corrections are checked by looking at the pre-fit ratio of the Z+jets events to events in both γ+jets and W+jets datasets. These corrections change the ratio and this cross check is important especially for NLO-EW corrections which are different for bosons (W and Z) and photons. The ratio is compared for MC and data by CMS monojet group and is found to be in a good agreement [146].

Source	Process	Uncertainty
Luminosity	All except for data driven backgrounds	2.6%
Electron trigger	MC bkgs in $W_{e\nu}$ and Z_{ee} CRs	1%
Photon trigger	MC bkgs in γ+jets CR	1%
$E_\mathrm{T}^\mathrm{miss}$ trigger	MC bkgs/signal in SR, $W_{\mu\nu}$ and $Z_{\mu\mu}$ CRs	shape vs $E_\mathrm{T}^\mathrm{miss}$
Jet energy scale	MC bkgs/signal in SR and CRs	5%
Muon-reco efficiency	MC bkgs in $W_{\mu\nu}$ and $Z_{\mu\mu}$ CRs	1%
Muon-ID efficiency	MC bkgs in $W_{\mu\nu}$ and $Z_{\mu\mu}$ CRs	1%
Electron-reco efficiency	MC bkgs in $W_{e\nu}$ and Z_{ee} CRs	1%
Electron-ID efficiency	MC bkgs in $W_{e\nu}$ and Z_{ee} CRs	2%
Photon-ID efficiency	MC bkgs in γ+jets CR	2%
Lepton veto	MC bkgs in SR like $Z_{\ell\ell}$, $t\bar{t}$, VV	shape vs $E_\mathrm{T}^\mathrm{miss}$
Photon purity	QCD in Photon CR	40%
b-jet veto	Top in SR and all CRs	6%
	All remaining in SR and all CRs	2%
Top p_T reweight	Top	10%
Top norm	Top	10%
VV norm	VV	20%
Z_{ll}+jets norm	Z_{ll}+jets (SR)	20%
γ+jets norm	γ+jets (SR)	20%
QCD (shape from DD)	QCD (SR)	$\tilde{}$100%

Table 7.5: List of all systematic uncertainties on minor backgrounds, taken directly from simulation of minor background processes (top, dibosons) or from data (QCD multi-jets) [146].

CHAPTER 8

RESULTS

8.1 Control Region only Fit

Two major electroweak backgrounds ($Z \rightarrow \nu\nu$ and $W \rightarrow l\nu$) are estimated by using maximum likelihood fit procedure as described in Section 7.3. The theoretical uncertainties in γ+jets to Z+jets and W+jets to Z+jets differential cross section ratios are included in the fit. A post-fit distribution for recoil is obtained by applying bin-by-bin reweighting factors on $Z \rightarrow \nu\nu$ and $W \rightarrow l\nu$ MC samples. Fit mainly depends on the control regions which have larger yields. Post-fit recoil plots for dimuon, dielectron, single muon, single electron and single photon CR, considering only data from the control regions, are shown in Appendix C. Experimental and theoretical uncertainties are represented by the gray bands in the ratio plots. All the post-fit control regions plots show a better agreement as compared to pre-fit distributions.

Finally the data and post-fit MC comparison in recoil distribution in signal region is shown in Figure 8.1, while the fit is exclusively control regions based. In this case, the post-fit background prediction is completely oblivious to the data in the signal region. Events with $\not{E}_T > 1250$ GeV are included in the last bin of recoil distribution. Non-thermal DM signals for benchmarks $M_{X_1} =$[1.0, 1.5, 2.0] TeV are shown in black. Each of the signal distribution peaks at half of the M_{X_1} whereas the couplings are chosen as $(\lambda_1, \lambda_2) = (0.07, 0.07)$. Data are found to be in agreement with the SM prediction.

The expected and observed event yields in monojet signal region are reported in Table 8.1.
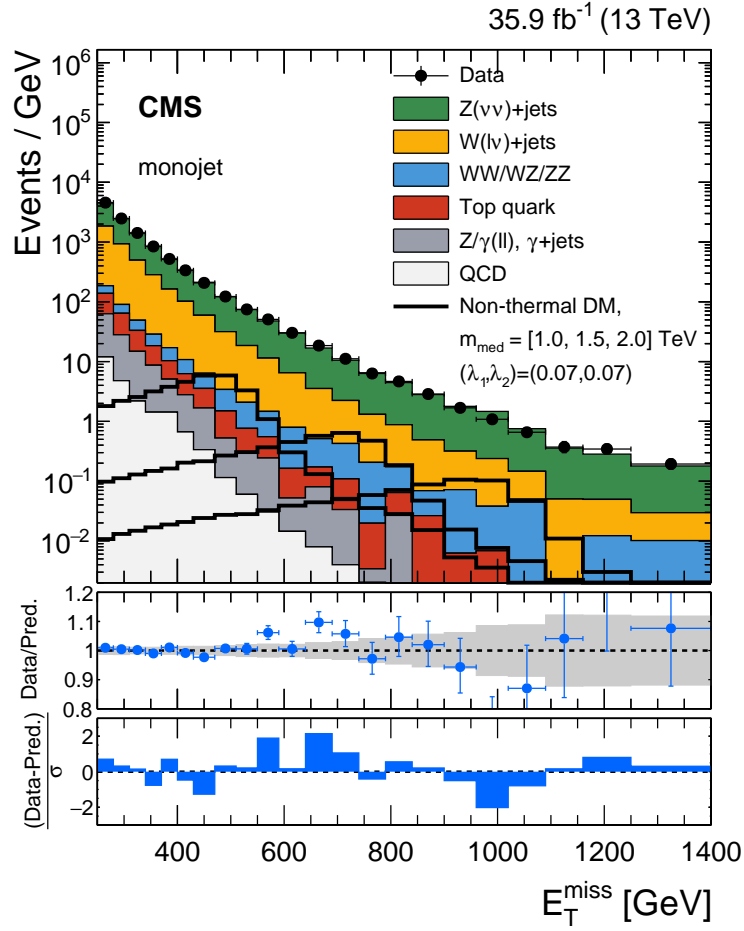
Figure 8.1: $\not{E}_T$ distributions for data and various SM backgrounds in signal region. No excess of data over the SM expectation is observed. The background processes are estimated by performing maximum likelihood fit to the data in all the control regions while signal region is excluded from the fit. Black curves represent $\not{E}_T$ distributions expected from Non-thermal DM model with M_{X_1} =1.0, 1.5 and 2.0 TeV, peaking at 500, 750 and 1000 GeV respectively. Signal curves are plotted for couplings $(\lambda_1, \lambda_2) = (0.07, 0.07)$. Data to predicted MC ratio is shown in the middle panel where gray bands indicate the post-fit uncertainty in the background prediction. Bottom panel shows the distributions of the pulls, defined as the difference between data and the post-fit background prediction relative to sum in quadrature of the post-fit uncertainty in the prediction and the statistical uncertainty on data.

$E\!\!\!/_T$ (GeV)	Observed	$Z \to \nu\nu$+jets	$W \to \ell\nu$+jets	Top	Diboson	Other	Total SM
250-280	136865	79700 ± 2300	49200 ± 1400	2360 ± 200	1380 ± 220	1890 ± 240	134500 ± 3700
280-310	74340	45800 ± 1300	24950 ± 730	1184 ± 99	770 ± 120	840 ± 110	73400 ± 2000
310-340	42540	27480 ± 560	13380 ± 260	551 ± 53	469 ± 77	445 ± 63	42320 ± 810
340-370	25316	17020 ± 350	7610 ± 150	292 ± 28	301 ± 51	260 ± 39	25490 ± 490
370-400	15653	10560 ± 220	4361 ± 91	157 ± 17	198 ± 33	152 ± 26	15430 ± 310
400-430	10092	7110 ± 130	2730 ± 47	104 ± 12	133 ± 23	84 ± 15	10160 ± 170
430-470	8298	6110 ± 100	2123 ± 37	75.2 ± 7.9	110 ± 19	67 ± 11	8480 ± 140
470-510	4906	3601 ± 75	1128 ± 22	38.6 ± 5.3	75 ± 12	21.0 ± 3.9	4865 ± 95
510-550	2987	2229 ± 39	658 ± 12	18.5 ± 3.3	51.7 ± 9.5	12 ± 2.4	2970 ± 49
550-590	2032	1458 ± 27	398 ± 8	12.3 ± 2.6	35.9 ± 7.1	9.7 ± 1.9	1915 ± 33
590-640	1514	1182 ± 26	284 ± 7	5.5 ± 1.4	30.9 ± 5.7	2.6 ± 0.7	1506 ± 32
640-690	926	667 ± 15	151 ± 4	4.6 ± 1.7	16.7 ± 3.9	4.0 ± 0.8	844 ± 18
690-740	557	415 ± 12	90.4 ± 3.0	3.8 ± 1.5	15.6 ± 3.6	1.7 ± 0.4	526 ± 14
740-790	316	259 ± 9.6	55.2 ± 2.3	0.8 ± 0.5	9.14 ± 2.3	0.2 ± 0.1	325 ± 12
790-840	233	178 ± 7.1	35.3 ± 1.7	1.7 ± 0.8	5.35 ± 1.7	1.4 ± 0.3	223 ± 9
840-900	172	139 ± 6.2	25.2 ± 1.3	1.5 ± 1.2	2.52 ± 1.05	0.04 ± 0.03	169 ± 8
900-960	101	88.1 ± 4.9	14.7 ± 0.9	0.3 ± 0.3	3.88 ± 1.42	0.03 ± 0.02	107 ± 6
960-1020	65	73.8 ± 4.7	12.0 ± 0.8	0.4 ± 0.3	1.83 ± 0.92	0.02 ± 0.01	88.1 ± 5.3
1020-1090	46	42.6 ± 3.1	6.7 ± 0.6	0.0 ± 0.0	3.42 ± 1.33	0.01 ± 0.01	52.8 ± 3.9
1090-1160	26	21.5 ± 2.1	3.5 ± 0.4	0.0 ± 0.0	0.00 ± 0.00	0.01 ± 0.00	25.0 ± 2.5
1160-1250	31	21.0 ± 2.2	3.3 ± 0.4	0.0 ± 0.0	1.07 ± 0.69	0.01 ± 0.00	25.5 ± 2.6
1250-1400	29	22.5 ± 2.4	2.9 ± 0.3	0.0 ± 0.0	1.49 ± 0.91	0.01 ± 0.00	26.9 ± 2.8

Table 8.1: The SM background predictions and their corresponding uncertainties compared to the data in each $E\!\!\!/_T$ bin are reported in the monojet signal region. The background yields and the corresponding uncertainties are obtained after performing a combined fit to data in all the control samples while excluding data in the signal region [146].

8.2   Control and Signal Region Background only Fit

In this section post-fit results are shown, which are obtained by performing maximum likelihood fit under the background only hypothesis including data from the signal region. Appendix C represents the post-fit recoil distributions for dimuon, dielectron, single muon, single electron and single photon control regions. The post-fit distributions, in this case are very much similar to what we get after applying CR only fit. Experimental and theoretical uncertainties are represented by the gray bands in the ratio plots.

$E\!\!\!/_T$ distribution in signal region is shown in Figure 8.2 where the fit includes events from signal region in the background estimation procedure. $E\!\!\!/_T$ distribution for Non-thermal DM signals with M_{X_1} = [1.0, 1.5, 2.0] TeV are also shown in black. Each of the signal curves peaks at half of the mediator mass. The coupling to SM and DM are considered as

$(\lambda_1, \lambda_2) = (0.07, 0.07)$. Data are found to be in good agreement with the SM prediction.
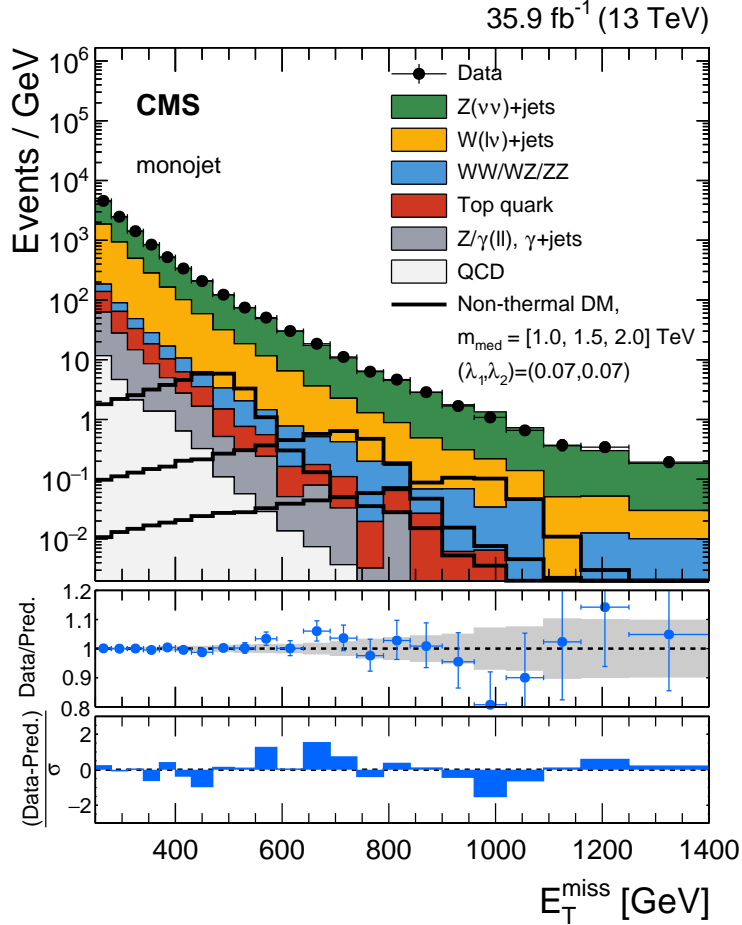
Figure 8.2: $\not{E}_T$ distributions for data and various SM backgrounds in signal region. No excess of data over the SM expectation is observed. The background processes are estimated by performing maximum likelihood fit to the data in all the control regions as well as in the signal region. Black curves represent $\not{E}_T$ distributions from Non-thermal DM model with $M_{X_1} = 1.0$, 1.5 and 2.0 TeV, peaking at 500, 750 and 1000 GeV respectively. Signal curves are plotted for couplings $(\lambda_1, \lambda_2) = (0.07, 0.07)$. Data to predicted MC ratio is shown in the middle panel where gray bands indicate the post-fit uncertainty in the background prediction. Bottom panel shows the distributions of the pulls, defined as the difference between data and the post-fit background prediction relative to sum in quadrature of the post-fit uncertainty in the prediction and the statistical uncertainty on data.

8.3   Nonthermal DM Limit Scan

No excess was observed over the SM background therefore results are interpreted in terms of upper limit on the nonthermal dark matter signal cross-section. Limits are computed using the CLs method [149, 150] with a profile likelihood ratio as the test statistic in which systematic uncertainties are modeled as nuisance parameters. Expected and observed upper limits are computed in a coupling gird of (λ_1, λ_2) where λ_1 and λ_2 ranges are set to $[0.01 - 1.5]$ and $[0.01 - 2.0]$ respectively. The coupling grid is selected in such a way that mediator width to mass ratio is approximately 30%.

The 95% confidence level (C.L.) observed and expected upper limits on $\mu = \sigma/\sigma_{th}$ in the $\lambda_1 - \lambda_2$ plane at the benchmarks $M_{X_1} = 1.0$ TeV, $M_{X_1} = 1.5$ TeV and $M_{X_1} = 2.0$ TeV are presented in Figures 8.3, 8.4 and 8.5 respectively. The uncertainty band around the median expected exclusion limit represents the one standard deviation due to the statistical and experimental systematic uncertainties. For $M_{X_1} = 1.0$ TeV and $M_{X_1} = 2$ .0 TeV, observed limits are stronger than expected and reside within one and two sigma respectively whereas in case of $M_{X_1} = 1.5$ TeV, observed limit is found to be weaker than expected and lies within 2 sigma expected limit standard deviation.

The plots for $\lambda_1 < 0.03 - 0.04$ represent the cross-section upper limits on $\not{E}_T +$ 2 jets channel for all benchmark points as this channel is dominant for smaller values of λ_1.
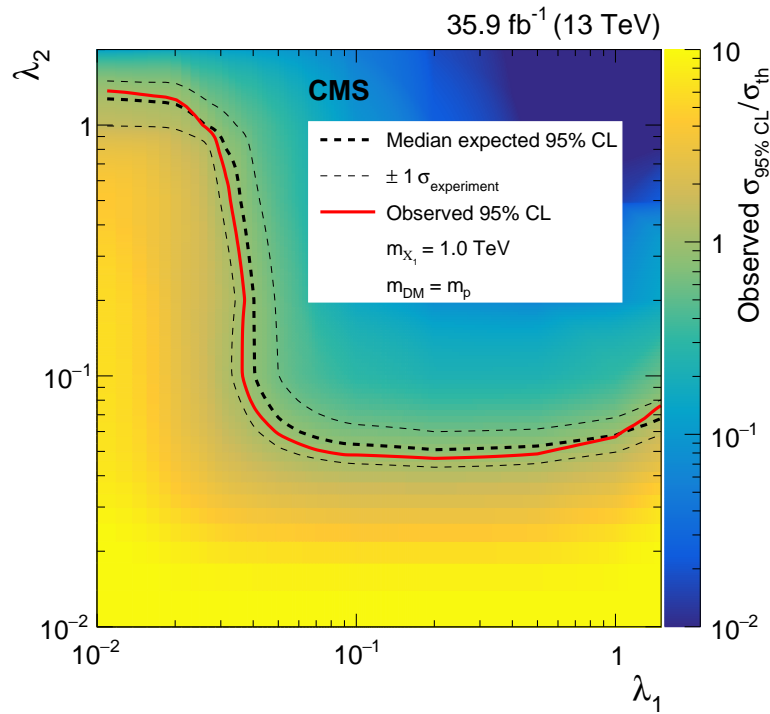
Figure 8.3: 95 % CL median expected and observed limits are shown for $M_{X_1} = 1.0$ TeV. The thick black curve shows the expected exclusion contour for an integrated luminosity of 35.9 fb^{-1}, while the solid red line represents the observed one. In this case observed limit is stronger than expected and lies well within one standard deviation.
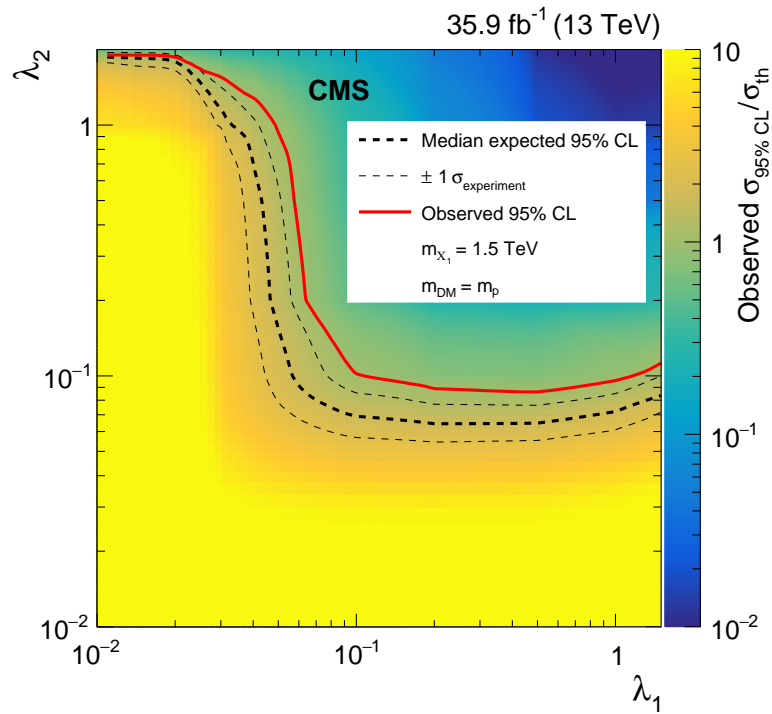
Figure 8.4: 95 % CL median expected and observed limits are shown for $M_{X_1} = 1.5$ TeV. The thick black curve shows the expected exclusion contour for an integrated luminosity of 35.9 fb^{-1}, while the solid red line represents the observed one. In this case observed limit is weaker than expected and lies well within two standard deviation.
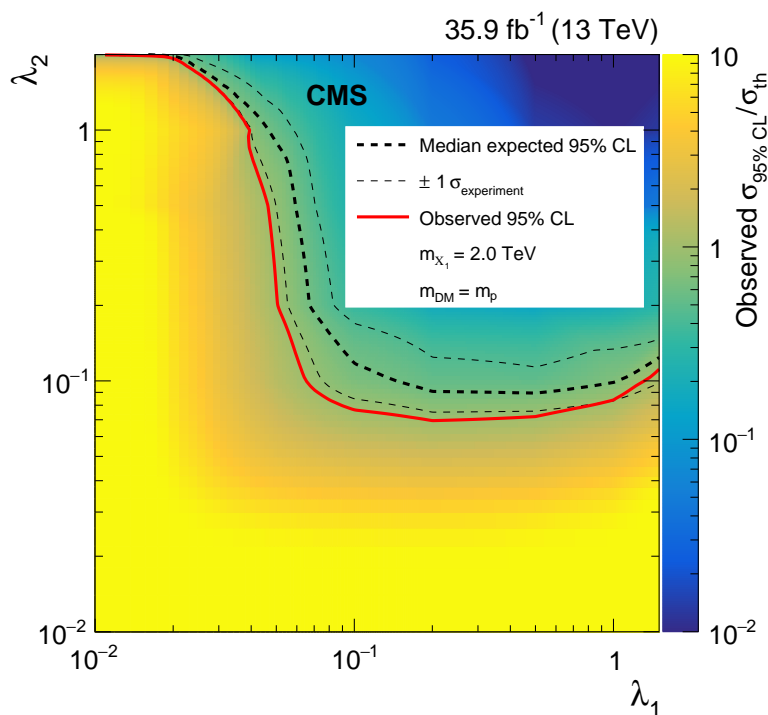
Figure 8.5: 95 % CL median expected and observed limits are shown for $M_{X_1} = 2.0$ TeV. The thick black curve shows the expected exclusion contour for an integrated luminosity of 35.9 fb^{-1}, while the solid red line represents the observed one. In this case observed limit is stronger than expected and lies well within two standard deviation.

8.3.1   Model Independent Interpretation

This section includes model independent interpretation of results in terms of upper limit on the resonance mass M_{X_1}. We are interested in that part of the coupling grid where mono-jet channel dominates or in other words $\not{E}_T$ distribution shows jacobian peak for all mediator masses as well as width of the mediator should be less that 10 GeV (condition for narrow resonance). According to $\not{E}_T$ distribution plots shown in Figures 4.6 and 4.7, the desired range of λ_1 and λ_2 is [0.01-0.5] each, where the mediator width is about 4.5% for all banch-marks (Table $4.1-4.4$). For this particular coupling range signal acceptance remains almost constant with the increase in M_{X_1} (Figure 4.14).

Figure 8.6 shows 95% C.L. expected and observed upper limits on production cross-section for resonance process where the decay products are a light quark jet and a light weakly interacting particle. Production cross section for light nonthermal DM model with $(\lambda_1, \lambda_2) = (0.1, 0.1)$ is also shown in red curve. This plot represents model independent limit for resonant processes when mediator decays to one quark or gluon jet and weakly interacting particle like neutrino or light dark matter.

Figure 8.7 represents 95% C.L. expected and observed upper limits on production cross-section as a function of mediator mass M_{X_1} for $(\lambda_1, \lambda_2) = (1.0, 0.1)$. In this case the limit is not model independent due to the fact that $\not{E}_T$ distribution is no more jacobian shaped due to dominance of other channels e.g. $\not{E}_T+2$ jets or dijet. Nonthermal DM theoretical cross-section is shown in red.
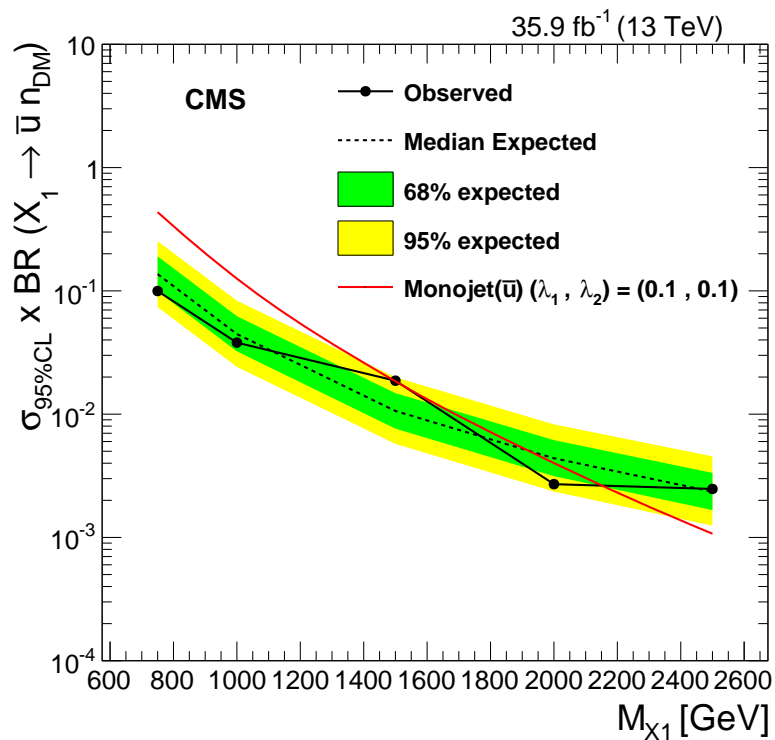
Figure 8.6: 95% C.L. observed and expected upper limits on production cross-section for resonance process are shown where the mediator decays to a light quark jet and a light weakly interacting particle. The expected limit is model independent and holds for the range of 0.01 to 0.5 for each of λ_1 and λ_2. Red curve is for nonthermal DM cross-section for $(\lambda_1, \lambda_2) = (0.1, 0.1)$.
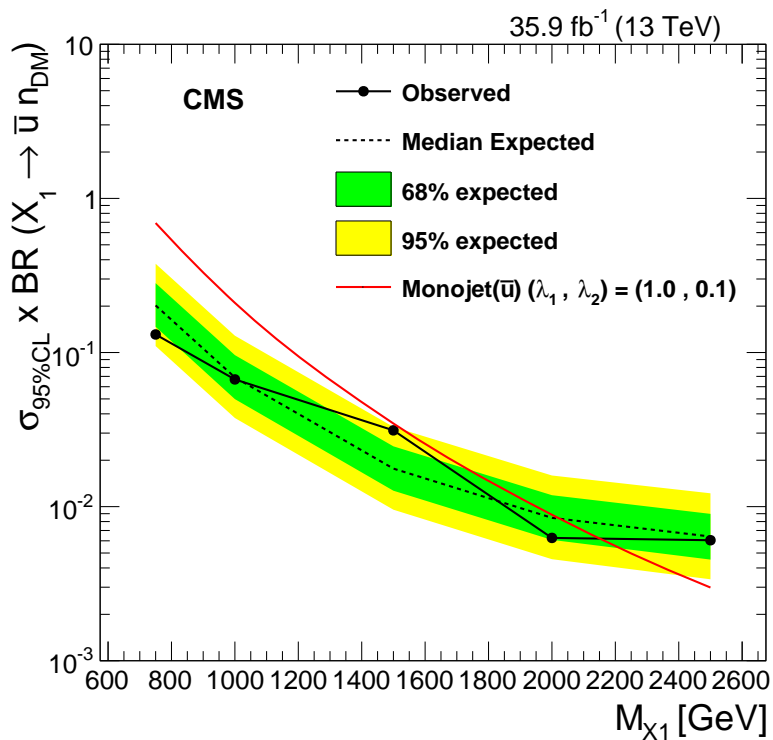
Figure 8.7: 95% C.L. observed and expected upper limits on production cross-section as a function of mediator mass M_{X_1} is shown for $(\lambda_1, \lambda_2) = (1.0, 0.1)$. Nonthermal DM theory cross-section is shown in red curve. The expected limit is model dependent in this case, as signal acceptance varies with coupling parameters and madiator mass M_{X_1} when $(\lambda_1, \lambda_2) > (0.5, 0.5)$.

CHAPTER 9

CONCLUSION

Discovery of Higgs boson, during Run 1 operation of LHC is a great achievement of high energy collider physics. It intrigued experimental and the theoretical particle physics community all over the world to look beyond Standard Model and investigate several unexplained phenomena at LHC. Understanding the existence and characteristics of dark matter is one of the major LHC goals.

For more than three decades, the most motivated candidates for dark matter are the Weakly Interacting Massive Particles (WIMPs), which arise in models beyond the SM. Most theoretical and experimental endeavors have been directed towards discovering WIMPs. However, the latest bounds from dark matter direct, indirect detection and LHC experiments do not provide any convincing signals of such particles so far. It may imply that DM is not made up of traditional WIMP candidate, which motivates the exploration of other interesting, non-WIMP dark matter particles e.g. axions, self-interacting dark matter and strongly-interacting dark matter. Several non-thermal DM scenarios are being explored at LHC.

The DM search at LHC is quite challenging and apparently may seem preposterous as we do not know whether dark matter's interaction with ordinary matter is substantially strong enough to probe such production in SM particles' collision. Nevertheless, dark matter searches at collider experiments have grown interest significantly due to the experimental feasibility of such searches at LHC. Now we have a sufficient knowledge of SM backgrounds processes and their differential distribution, that even a very minor disagreement in the missing transverse energy distribution may provide us a useful new physics signature. Numerous dark matter models has been devised to predict missing transverse energy signal, including so-called mono-X searches which deal with direct production of dark matter in association with SM states. Study of monojet channel is one of such searches, which looks for events

where a high transverse momentum jet is produced along with large missing transverse energy $\not{E}_T$, which is the topic of this dissertation as well.

I performed this analysis by studying and analyzing monojet (one or more jets plus $\not{E}_T$) events in proton-proton collisions at center of mass energy $\sqrt{s}$ =13 TeV. The data for this study is taken from CMS detector at LHC, collected during Run 2 operation in 2016, with an integrated luminosity of 35.9 fb^{-1}. I interpreted the results in terms of Light Non-thermal DM model, which explains existence of dark matter as well as baryon asymmetry in the universe. The main features of this model are: its jacobian peak in the $\not{E}_T$ distribution, peaking at approximately half of the mediator mass and a very light dark matter candidate whose stability is ensured by fixing its mass equal to that of the proton. For model, monojet and 2-jets plus $\not{E}_T$ events are selected. Various mediator masses are considered for this study, e.g. {1.0, 1.5, 2.0, 2.5} TeV. The final $\not{E}_T$ distribution shows excess of events within 2σ, over the SM backgrounds for $M_{X_1} = 1.5$ TeV. This is not enough to call it a discovery, but requires to check in future data. No significant excess of events is observed for other mediator masses. I have also set model independent limit on the mediator mass, by constraining the coupling parameter space to exclusively monojet channel i.e. each coupling ranges as $[0.01-0.5]$. It provides expected upper limit on narrow resonance, decaying to a light quark jet and a light weakly interacting particle.

There is a strong motivation for the existence of dark matter and with today's constant advancement of technology and analysis techniques, it is hoped to observe such signature in near future.

BIBLIOGRAPHY

[1] H. Murayama, "Physics Beyond the Standard Model and Dark Matter", Lectures at Les Houches Summer School, Session 86, Particle Physics and Cosmology: the Fabric of Spacetime, July 31- August 25, 2006 , arXiv:0704.2276.

[2] P. S. B. Dev, A. Mazumdar, S. Qutub, "Constraining Non-thermal and Thermal properties of Dark Matter", *Physics* **2** (2014) 26, arXiv:1311.5297.

[3] H. Baer, K.Y. Choi, J. E. Kim, L. Roszkowski, "Dark matter production in the early Universe: beyond the thermal WIMP paradigm", *Phys. Rep.* **555** (2015) 1, arXiv:1407.0017.

[4] G. Bertone, D. Hooper and J. Silk, "Dark matter production in the early Universe: beyond the thermal WIMP paradigm", *Phys.Rep.* **555** (2015) 1, arXiv:1407.0017.

[5] S.M. Boucenna and S. Morisi, "Theories relating baryon asymmetry and dark matter: A mini review", *Front. Phys.* **1** (2013) 33, arXiv:1310.1904v3.

[6] H. Okada, Y. Orikasa, T. Toma, "Nonthermal dark matter models and signals", *Phys. Rev. D.* **93** (2016) 055007, arXiv:1511.01018v3.

[7] H.Baer, K.-Y. Choi, J. E. Kim, L. Roszkowski, "Dark matter production in the early Universe: beyond the thermal WIMP paradigm", *Phys. Rep.* **555** (2015) 1, arXiv:1407.0017v3.

[8] R. Oerter. "The Theory of Almost Everything: The Standard Model, the Unsung Triumph of Modern Physics" (Kindle ed.), Penguin Group p. 2. ISBN 0-13-236678-9.

[9] CDF Collaboration, "Observation of Top quark production in $p\bar{p}$ collisions with the collider detector at Fermilab", *Physical Review Letters* **74** (1995) 2626.

[10] DONUT Collaboration, "Observation of tau neutrino interactions", *Physics Letters B* **504** (2001) 218.

[11] CMS Collaboration, "Observation of a new boson at a mass of 125 GeV with the CMS experiment at the LHC", *Physics Letters B* **716** (2012) 30.

[12] ATLAS Collaboration, "Observation of a new particle in the search for the Standard Model Higgs boson with the ATLAS detector at the LHC", *Physics Letters B* **716** (2012) 1.

[13] D. Griffiths, "Introduction to Elementary Particles", John Wiley & Sons, New York, USA (2008).

[14] F. Halzen and A. Martin, "Quarks and Leptons:An Introductory Course In Modern Particle Physics", Wiley (2008).

[15] Lillian Hoddeson, "The Rise of the Standard Model: A History of Particle Physics from 1964 to 1979", Cambridge University Press (1997).

[16] M. K. Gaillard, P. D. Grannis, and F. J. Sciulli, "The standard model of particle physics", *Rev. Mod. Phys.* **71** (1999) 96.

[17] W. N. Cottingham, D. A. Greenwood, "An Introduction to the Standard Model of Particle Physics", Cambridge University Press, (2007)

[18] S. Weinberg, "A Model of Leptons", *Phys. Rev. Lett.* **19** (1967) 1264.

[19] A. Salam, "Electromagnetic and Weak Interactions", *Physics Letters* **13** (1964) 168.

[20] P. W. Higgs, "Electromagnetic and Weak Interactions", *Phys. Rev. Lett.* **13** (1964) 508.

[21] G. Bernardi, M. Carena, and T. Junk, "Higgs bosons: theory and searches", Reviews of Particle Data Group: Hypothetical particles and Concepts, `http://pdg.lbl.gov/2008/reviews/higgs_s055.pdf` (2007).

[22] P. W. Anderson, "Gauge Invariance and Mass", *Phys. Rev.* **125** (1962) 397.

[23] P. W. Anderson, "Plasmons, Gauge Invariance, and Mass", *Phys. Rev.* **130** (1963) 439.

[24] G. S. Guralnik, C. R. Hagen, and T. W. B. Kibble, "Global Conservation Laws and Massless Particles", *Phys. Rev. Lett.* **13** (1964) 585.

[25] J. Ellis. "Outstanding questions: physics beyond the Standard Model", *Phil. Trans. Roy. Soc. Lond.* **370** (2012) 818.

[26] B. Gripaios, "Lectures on Physics Beyond the Standard Model", (2015), arXiv:1503.02636.

[27] M. M. Nojiri, "Beyond the Standard Model", CERN Yellow Report CERN, (2014), arXiv:1406.1410 [hep-ph].

[28] G. Bertone, D. Hooper and J. Silk, "Particle Dark Matter: Evidence, Candidates and Constraints", *Phys.Rept* **405** (2005) 279, arXiv:hep-ph/0404175.

[29] P. A. R. Ade et al., Planck Collaboration, *astro-ph.CO* (2014), arXiv:1303.5076v3.

[30] L. V. Koopmans and T. Treu, "The Structure and Dynamics of Luminous and Dark Matter in the Early-Type Lens Galaxy of 0047-281 at z=0.485", *Astrophys.J.* **583** (2003) 606, arXiv:astro-ph/0205281.

[31] R.B. Metcalf, L.A. Moustakas, A.J. Bunker, I.R. Parry, "Spectroscopic Gravitational Lensing and Limits on the Dark Matter Substructure in Q2237+0305", *Astrophys.J.* (2004), arXiv:astro-ph/0309738.

[32] L. A. Moustakas and R. B. Metcalf, "Detecting dark matter substructure spectroscopically in strong gravitational lenses", *Mon.Not.Roy.Astron.Soc.* **339** (2003) 607, arXiv:astro-ph/0206176.

[33] J. N. Bahcall, C. Flynn, and A. Gould, "Local dark matter from a carefully selected sample", *Astrophysical J.* **389** (1992) 234.

[34] H. Hoekstra, H. Yee and M. Gladders, "Detecting dark matter substructure spectroscopically in strong gravitational lenses", *New Astron.Rev.* **46** (2002) 767, arXiv:astro-ph/0205205.

[35] S. S. Vogt, M. Mateo, E. W. Olszewski and M. J. Keane, "Internal kinematics of the Leo II dwarf spherodial galaxy", *Astron. Journal* **109** (1995) 151, arXiv:astro-ph/0205205.

[36] M. Mateo, "Dwarf Galaxies of the Local Group", *Ann. Rev. Astron. Astrophys.* **36** (1998) 435, arXiv:astro-ph/9810070.

[37] D. Zaritsky, R. Smith, C. Frenk and S. D. M. White, "More Satellites of Spiral Galaxies", *Astrophys. J.* **478** (1997).

[38] M. Azzaro, F. Prada and C. M. Gutierrez, "Motion properties of satellites around external spiral galaxies", (2003), arXiv:astro-ph/0310487.

[39] F. Zwicky, "Die Rotverschiebung von extragalaktischen Nebeln", *Helv. Phys. Acta* **6** (1933) 110.

[40] N. Bahcall and X. Fan, "The Most Massive Distant Clusters: Determining Ω and σ_8", *Astrophys. J.* **504** (1998) 1.

[41] A. Kashlinsky, "Determining Ω from the cluster correlation function", *Phys. Rep.* **307** (1998) 67.

[42] K. G. Begeman, A. H. Broeils and R. H. Sanders, "Extended rotation curves of spiral galaxies: dark haloes and modified dynamics", Monthly Notices of the Royal Astronomical Society. **249** (1991).

[43] R. G. Carlberg et al., "The$\Omega_M - \Omega_\Lambda$ Dependence of the Apparent Cluster Ω", *Astrophys. J.* **516** (1999) 552.

[44] G. Servant and T. M. Tait, "Elastic Scattering and Direct Detection of Kaluza-Klein Dark Matter", *New J. Phys.* **4**, 99 (2002) 552, arXiv:hep-ph/0209262.

[45] W. Hu and S. Dodelson, "Cosmic Microwave Background Anisotropies", *Ann. Rev. Astron. Astrophys.* **40**, 171 (2002), arXiv:astro-ph/0110414.

[46] W. Hu, N. Sugiyama and J. Silk, "The Physics of Microwave Background Anisotropies", *Nature* **386**, 37 (1997), arXiv:astroph/9604166.

[47] M. Tegmark et al., "Cosmological parameters from SDSS and WMAP", *Phys.Rev.D* **69** (2004), arXiv:astro-ph/0310723.

[48] C. l. Kuo et al., "High Resolution Observations of the CMB Power Spectrum with ACBAR", *Astrophys. J* **600** (2004) 32, arXiv:astroph/0212289.

[49] T. J. Pearson et al., "The Anisotropy of the Microwave Background to l = 3500: Mosaic Observations with the Cosmic Background Imager", *Astrophys. J* **591** (2003) 556, arXiv:astro-ph/0205388.

[50] K. A. Olive, "TASI Lectures on Dark Matter", (2002), arXiv:astro-ph/0301505.

[51] Smile, and the Universe Smiles With You, (2015, February 10). `https://www.jpl.nasa.gov/spaceimages/details.php?id=pia18794`.

[52] G. Steigman and M. S. Turner, "Cosmological constraints on the properties of weakly interacting massive particles", *Nucl. Phys. B* **253** (1985) 375.

[53] K. Griest, "Cross sections, relic abundance, and detection rates for neutralino dark matter", *Phys. Rev. D* **38**, 2357 (1988).

[54] H.-C. Cheng, J. L. Feng, and K. T. Matchev, "Kaluza-Klein Dark Matter", *Phys. Rev. Lett.* **89**, 211301 (2002).

[55] S. A. Bonometto, F. Gabbiani and A. Masiero, "Possible Evidence For Axino Dark Matter In The Galactic Bulge", *Phys. Rev. D* **49**, 3918 (1994), arXiv:hep-ph/9305237.

[56] T. Goto and M. Yamaguchi, "Is axino dark matter possible in supergravity?", *Phys. Lett. B* **276** (1992) 103, arXiv:hep-ph/9305237.

[57] L. Covi, J. E. Kim and L. Roszkowski, "Axinos as Cold Dark Matter", *Phys. Rev. Lett.* **82**, 4180 (1999), arXiv:hep-ph/9905212.

[58] L. Covi, H. B. Kim, J. E. Kim and L. Roszkowski, "Axinos as Dark Matter", *JHEP* **0105**, 033 (2001), arXiv:hep-ph/0101009.

[59] L. Covi, L. Roszkowski, R. R. de Austri and M. Small, "Axino Dark Matter and the CMSSM", *JHEP* **0406**, 003 (2004), arXiv:hep-ph/0402240.

[60] J. L. Feng, A. Rajaraman and F. Takayama, "Superweakly Interacting Massive Particles", *Phys. Rev. Lett.* **91** (2003) 011302, arXiv:hep-ph/0302215.

[61] K. Abazajian, "Linear cosmological structure limits on warm dark matter", *Phys. Rev. D* **73** (2006) 063513.

[62] M. Viel et al., "Can Sterile Neutrinos Be Ruled Out as Warm Dark Matter Candidates?", *Phys. Rev. D* **97**, 071301 (2006).

[63] A. Birkedal-Hansen and J. G. Wacker, "Scalar Dark Matter From Theory Space", *Phys. Rev. D* **69**, 065022 (2003), arXiv:hep-ph/0306161.

[64] H. C. Cheng and I. Low, "TeV Symmetry and the Little Hierarchy Problem", *JHEP* **0309**, 051 (2003), arXiv:hep-ph/0308199.

[65] H. M. Hodges, "Mirror baryons as the dark matter", *Phys. Rev. D* **47**, 456 (1993).

[66] R. Foot, "Implications of the DAMA and CRESST experiments for mirror matter-type dark matter", *Phys. Rev. D* **69**, 036001 (2004), arXiv:hep-ph/0308254.

[67] A. Y. Ignatiev and R. R. Volkas, "Mirror dark matter and large scale structure", *Phys. Rev. D* **68** (2003) 023518, arXiv:hep-ph/0304260.

[68] R. N. Mohapatra, S. Nussinov and V. L. Teplitz, "Mirror Matter as Self Interacting Dark Matter", *Phys. Rev. D* **66** (2002) 063002, arXiv:hep-ph/0111381.

[69] A. De Rujula, S. L. Glashow and U. Sarid, "Charged Dark Matter", *Nucl. Phys. B* **333** (1990) 173.

[70] R. Dave, D. N. Spergel, P. J. Steinhardt and B. D. Wandelt, "Halo Properties in Cosmological Simulations of Self-Interacting Cold Dark Matter", *Astrophys. J.* **547** (2001) 574, arXiv:astro-ph/0006218.

[71] D. N. Spergel and P. J. Steinhardt, "Observational evidence for self-interacting cold dark matter", *Phys. Rev. Lett.* **84**, 3760 (2000), arXiv:astro-ph/9909386.

[72] G. Shiu and L. T. Wang, "D-Matter", *Phys.Rev. D* **69**, 126007 (2004), arXiv:hep-ph/0311228.

[73] J. A. R. Cembranos, A. Dobado and A. L. Maroto, "Brane-world dark matter", *Phys. Rev. Lett.* **90**, 241301 (2003) , arXiv:hep-ph/0302041.

[74] J. R. Ellis, G. B. Gelmini, J. L. Lopez, D. V. Nanopoulos and S. Sarkar, "Astrophysical constraints on massive unstable neutral relic particles", *Nucl. Phys. B* **373**, 399 (1992).

[75] A. Drukier and L. Stodolsky, "Principles and applications of a neutral-current detector for neutrino physics and astronomy", *Phys. Rev. D* **30**, 2295 (1984).

[76] M. W. Goodman and E. Witten, "Detectability of Certain Dark Matter Candidates", *Phys. Rev. D* **31**, 3059 (1985).

[77] I. Wasserman, "Possibility of detecting heavy neutral fermions in the Galaxy", *Phys. Rev. D.* **33** (1986) 2071.

[78] G. Jungman, M. Kamionkowski and K. Griest, "Supersymmetric Dark Matter", *Phys. Rept.* **267** (1996) 195, arXiv:hep-ph/9506380.

[79] R. Bernabei et al., Talk at the 10th International Workshop on Neutrino Telescopes, Venice, Italy, (2003), arXiv:hep-ph/9506380.

[80] D. S. Akerib et al, CDMS Collaboration, "New Results from the Cryogenic Dark Matter Search Experiment", *Phys. Rev. D* **68** (2003) 082002, arXiv:hep-ex/0306001.

[81] A. Benoit et al., "Improved Exclusion Limits from the EDELWEISS WIMP Search", *Phys. Lett. B* **545** (2002) 43, arXiv:astro-ph/0206271.

[82] D. S. Akerib et al., "Results on the Spin-Dependent Scattering ofWeakly Interacting Massive Particles on Nucleons from the Run 3 Data of the LUX Experiment.", *Phys. Rev. Lett.* **116**, 161302 (2016), arXiv:1602.03489.

[83] O. Adriani et al., "An anomalous positron abundance in cosmic rays with energies 1.5-100 GeV", *Nature* **458**, 607 (2009).

[84] A. A. Abdo et al., "Measurement of the Cosmic Ray $e^+ + e^-$ Spectrum from 20 GeV to 1 TeV with the Fermi Large Area Telescope", *Phys. Rev. Lett.* **102**, 181101 (2009).

[85] R. Abbasi et al., "Search for dark matter from the Galactic halo with the IceCube Neutrino Telescope", *Phys. Rev. D* **84**, 022004 (2011).

[86] K. N. Abazajian et al., "Conservative constraints on dark matter from the Fermi-LAT isotropic diffuse gamma-ray background spectrum", *JCAP* **11** (2010) 041.

[87] A. Gould, "Weakly interacting massive particle distribution in and evaporation from the sun", *Astrophys. J.* **321** 560 (1987).

[88] The IceCube Collaboration, "Multi-year search for dark matter annihilations in the Sun with the AMANDA-II and IceCube detectors", *Phys. Rev. D* **85**, 042002 (2012) .

[89] M. Ackermann et al., The Fermi LAT Collaboration, "Constraining Dark Matter Models from a Combined Analysis of Milky Way Satellites with the Fermi Large Area Telescope", *Phys. Rev. Lett.* **107**, 241302 (2011) .

[90] M. et al. Aartsen, The IceCube Collaboration, "Search for dark matter annihilations in the sun with the 79-string IceCube detector", *Phys. Rev. Lett.* **110**, 131302 (2013).

[91] T. Tanaka et al., The Super-Kamiokande Collaboration, "An Indirect Search for WIMPs in the Sun using 3109.6 days of upward-going muons in Super-Kamiokande", *Astrophys. J.* **742** (2011) 78, arXiv:1108.3384.

[92] O. Buchmueller, C. Doglioni and L.-T. Wang, "Search for dark matter at colliders", *Nature* **13** (2017) 217.

[93] G. Aad et al., ATLAS Collaboration, "Search for new phenomena in final states with an energetic jet and large missing transverse momentum in pp collisions at $\sqrt{s}=$8 TeV with the ATLAS detector", *Eur. Phys. J. C* **75**,299 (2015), arXiv:1502.01518.

[94] V. Khachatryan et al., "Search for dark matter, extra dimensions, and unparticles in monojet events in proton proton collisions at $\sqrt{s}=$8 TeV", *Eur. Phys. J. C* **75**,235 (2015), arXiv:1408.3583.

[95] V. Khachatryan et al. "Search for physics beyond the standard model in final states with a lepton and missing transverse energy in proton-proton collisions at $\sqrt{s}=$8 TeV", *Phys. Rev., D* **91**,092005 (2015), arXiv:1408.2745.

[96] G. Aad et al., ATLAS Collaboration, "Search for new particles in events with one lepton and missing transverse momentum in pp collisions at $\sqrt{s}=$8 TeV with the ATLAS detector", *JHEP* **09**,037 (2014), arXiv:1407.7494.

[97] G. Aad et al., ATLAS Collaboration, "Search for new phenomena in events with a photon and missing transverse momentum in pp collisions at $\sqrt{s}=$8 TeV with the ATLAS detector", *Phys. Rev. D* **91**,012008 (2015), arXiv:1411.1559.

[98] S. Chatrchyan et al., "Search for Dark Matter and Large Extra Dimensions in pp Collisions Yielding a Photon and Missing Transverse Energy", *Phys. Rev. Lett.* **108**, 261803 (2016), arXiv:1204.0821.

[99] V. Khachatryan et al., ATLAS Collaboration, "Search for new phenomena in monophoton final states in proton-proton collisions at $\sqrt{s}=$8 TeV with the ATLAS detector", *Phys. Lett., B* **755** (2012) 102, arXiv:1410.8812.

[100] G. Aad et al., ATLAS Collaboration, "Search for dark matter in events with a Z boson and missing transverse momentum in pp collisions at $\sqrt{s}$ =8 TeV with the ATLAS detector", *Phys. Rev. D* **90**, 012004 (2014), arXiv:1404.0051.

[101] G. Aad et al., ATLAS Collaboration, "Search for dark matter in events with a hadronically decaying W or Z boson and missing transverse momentum in pp collisions at $\sqrt{s}$ =8 TeV with the ATLAS detector", *Phys. Rev. D* **112**, 041802 (2014), arXiv:1309.4017.

[102] G. Aad et al., ATLAS Collaboration, "Search for dark matter in events with heavy quarks and missing transverse momentum in pp collisions with the ATLAS detector", *Eur. Phys. J. C* **75**, 92 (2015), arXiv:1410.4031.

[103] V. Khachatryan et al., "Search for Monotop Signatures in Proton-Proton Collisions at $\sqrt{s}$ =8 TeV", *Phys. Rev. Lett.* **114**, 101801 (2015), arXiv:1410.1149.

[104] V. Khachatryan et al., "Search for the production of dark matter in association with top-quark pairs in the single-lepton final state in proton-proton collisions at $\sqrt{s} = 8$ TeV", *JHEP* **06** (2015) 121, arXiv:1504.03198.

[105] A. Berlin, T. Lin, and L.-T. Wang, "Mono-Higgs Detection of Dark Matter at the LHC", *JHEP* **06**, 078 (2014), arXiv:1402.7074.

[106] L. Carpenter, A. DiFranzo, M. Mulhearn, C. Shimmin, S. Tulin, and D. Whiteson, "Mono-Higgs-boson: A new collider probe of dark matter", *Phys. Rev. D* **89** (2014) 075017, arXiv:1312.2592.

[107] A. Askew, S. Chauhan, B. Penning, W. Shepherd, and M.Tripathi, "Searching for Dark Matter at Hadron Colliders", *Int. J. Mod. Phys.* **29** (2014) 1430041, arXiv:1406.5662.

[108] L. Evans and P. Bryant, "LHC machine", *JINST* **3** (2008) S08001.

[109] Updates: February 2013, `http://home.cern/about/updates/2013/02/long-shutdown-1-exciting-times-ahead.`.

[110] Restarting the LHC: Why 13 Tev?, `http://home.cern/about/engineering/restarting-lhc-why-13-tev.`.

[111] The CMS Collaboration, "The CMS experiment at the CERN LHC", *JINST* **3** (2008) S08004.

[112] Serguei Chatrchyan et al., "Description and performance of track and primary-vertex reconstruction with the CMS tracker", *JINST* **9** (2014) P10009, arXiv:1405.6569.

[113] T. Sjostrand, S. Mrenna and P. Skands, "PYTHIA 6.4 physics and manual", *JHEP* **0605**, 026 (2006), arXiv:hep-ph/0603175.

[114] J. Alwall, M. Herquet, F. Maltoni, O. Mattelaer, and T. Stelzer, "Madgraph 5: going beyond", *JHEP* **1106** (2011) 128, arXiv:1106.0522.

[115] C. F. Berger, Z. Bern, L. J. Dixon, F. F. Cordero, D. Forde, T. Gleisberg, H. Ita, D. A. Kosower, and D. Maitre, "Multi-jet cross sections at NLO with Black-Hat and Sherpa", March 14-21, 2009, pages 265?268, (2009). `http://www-public.slac.stanford.edu/sciDoc/docMeta.aspx?slacPubNumber=slac-pub-13630,arXiv:0905.2735`.

[116] S. Alioli, "NLO and Parton Showers: The POWHEG-BOX", In Physics at the LHC2010. Proceedings, 5th Conference, PLHC2010, Hamburg, Germany, June 7-12, 2010, pages 204?208, (2010). `https://inspirehep.net/record/867509/files/arXiv:1009.2348.pdf,arXiv:1009.2348`.

[117] Geant4 user?s documents, CERN, Geneva, 1998. `https://cds.cern.ch/record/998155`.

[118] CMS Luminosity-Public Results, `https://twiki.cern.ch/twiki/bin/view/CMSPublic/LumiPublicResults#Multi_year_Collisions_Plots`.

[119] CMS Hadron Calorimeter Main Links, (2016, January 06), `http://cmshcal.web.cern.ch/cmshcal/`.

[120] CMS Detector Slice, (2016, January 15), `https://cds.cern.ch/record/2120661`.

[121] T. lenzi, "Development and Study of Different Muon Track Reconstruction Algorithms for the Level-1 Trigger for the CMS Muon Upgrade with GEM Detectors", CERN-THESIS-2013-042, arXiv:1306.0858, `https://inspirehep.net/record/1236817/files/img_cms_coordinates.png`.

[122] L.Taylor, (2011, November 23), Silicon Strips, `http://cms.web.cern.ch/news/silicon-strips`.

[123] The CMS Collaboration, "The CMS experiment at the CERN LHC. The Compact Muon Solenoid experiment", *J. Instrum.* **3**,S08004 (2008).

[124] A. Bartoloni et al., "The CMS ECAL barrel HV system", *J. Instrum.* **8**,C02039 (2013).

[125] CMS Detector Layout, `http://www.hephy.at/user/friedl/diss/html/node8.html`.

[126] P. Paolucci et al., "CMS Resistive Plate Chamber overview, from the present system to the upgrade phase I", *J. Instrum.* **8**,P04005 (2013).

[127] M. Felcini, "The Trigger System of the CMS Experiment", *Nucl.Instrum.Meth.A* **598** (2009) 312, arXiv:0806.2540.

[128] B. Dutta, Y. Gao, and T. Kamon, "Probing Light Nonthermal Dark Matter at the LHC", In QCD and high energy interactions. Proceedings, 44th Rencontres de Moriond, La Thuile, Italy, *Phys. Rev. D* **89** (2014) 096009, arXiv:hep-ph/1401.1825.

[129] R. Allahverdi and B. Dutta, "Natural GeV Dark Matter and the Baryon-Dark Matter Coincidence Puzzle", *Phys. Rev. D* **88** (2013) 023525, arXiv:hep-ph/1304.0711.

[130] A.Bhatti et al., "Search for New Physics in the Monojet final state at CMS", Technical Report, CERN, 2014. CMS Analysis Note : AN-12-421.

[131] CMS Collaboration, "Search for new physics in monojet events in pp collisions at $\sqrt{s} = 8$ TeV", Technical Report, CMS-PAS-EXO-12-048, CERN, Geneva, 2013.

[132] T. Aaltonen, et al., "Search for new particles decaying into dijets in proton-antiproton collisions at $\sqrt{s} = 1.96$ TeV", *Phys. Rev. D* **79** (2009) 112002, arXiv:0812.4036 [hep-ex].

[133] ATLAS Collaboration , "Search for squarks and gluinos with the ATLAS detector in final states with jets and missing transverse momentum and 20.3 fb^{-1} of $\sqrt{s} = 8$ TeV proton-proton collision data", Technical Report, ATLAS-CONF-2013-047, CERN, Geneva, 2013.

[134] S. Chatrchyan et al., "Search for pair-produced dijet resonances in four-jet final states in pp collisions at $\sqrt{s} = 7$ TeV", *Phys. Rev. Lett.* **110** (2013) 141802.

[135] CMS Jet/MET POG. `https://twiki.cern.ch/twiki/bin/viewauth/CMS/MissingETOptionalFiltersRun2`.

[136] CMS BTV POG. `https://twiki.cern.ch/twiki/bin/viewauth/CMS/BtagRecommendation74X`.

[137] CMS Muon POG. `https://twiki.cern.ch/twiki/bin/view/CMSPublic/SWGuideMuonIdRun2#Loose_Muon`.

[138] CMS Muon POG. `https://twiki.cern.ch/twiki/bin/view/CMSPublic/SWGuideMuonIdRun2#Tight_Muon`.

[139] CMS EGamma POG. `https://twiki.cern.ch/twiki/bin/viewauth/CMS/CutBasedElectronIdentificationRun2#Spring15_selection_25ns`.

[140] tau-POG. `https://twiki.cern.ch/twiki/bin/view/CMS/TauIDRecommendation13TeV`.

[141] CMS EGamma POG. `https://twiki.cern.ch/twiki/bin/view/CMS/EgammaIDRecipesRun2#Photon_efficiencies_and_scale_fa`.

[142] R. Frederix and S. Frixione, "Merging meets matching in MC@NLO" *JHEP* **12** (2012) 061, arXiv:1209.6215.

[143] S. Frixione, "Isolated photons in perturbative QCD" *Phys. Lett.* **B429** (1998) 369, arXiv:hep-ph/9801442.

[144] S. Kallweit et al., "NLO electroweak automation and precise predictions for W+multijet production at the LHC" *JHEP* **04** (2015) 012, arXiv:1412.5157.

[145] S. Kallweit et al., "NLO QCD+EW automation and precise predictions for V+multijet production" in Proceedings, 50th Rencontres de Moriond, QCD and high energy interactions, pp. 121-124. 2015. arXiv:1505.05704.

[146] N. Daci et al., "Search for dark matter produced with an energetic jet or a hadronically decaying W or Z boson at $\sqrt{s}$ =13 TeV with the full 2016 dataset", Technical Report, CERN, 2016. CMS Analysis Note : AN-16-473.

[147] CMS Collaboration, "Search for dark matter produced with an energetic jet, or a hadronically decaying W or Z boson, at $\sqrt{s}$ =13 TeV", *JHEP* **07** (2017) 014, arXiv:1703.01651.

[148] CMS Collaboration, "Search for dark matter produced with an energetic jet, or a hadronically decaying W or Z boson using 12.9 fb^{-1} data at $\sqrt{s}$ =13 TeV", Technical Report,CERN, Geneva, 2016. CMS-PAS-EXO-16-037.

[149] T. Junk, "Confidence level computation for combining searches with small statistics" *Nucl. Instrum. Meth. A* **434** (1999) 435, arXiv:hep-ex/9902006.

[150] A. L. Read, "Presentation of search results: the CLs technique" *J. Phys. G* **28** (2002).

APPENDIX A: GENERATOR LEVEL PLOTS FOR HIGHER M$_{X1}$

$\not{E}_T$ **Distribution**

This section includes generator level studies for higher mediator masses e.g. M$_{X_1}$ =3.0 and 3.5 TeV. These mass points are not incorporated in analysis part of this dissertation but this study may prove helpful for future analysis, with more data in hand.
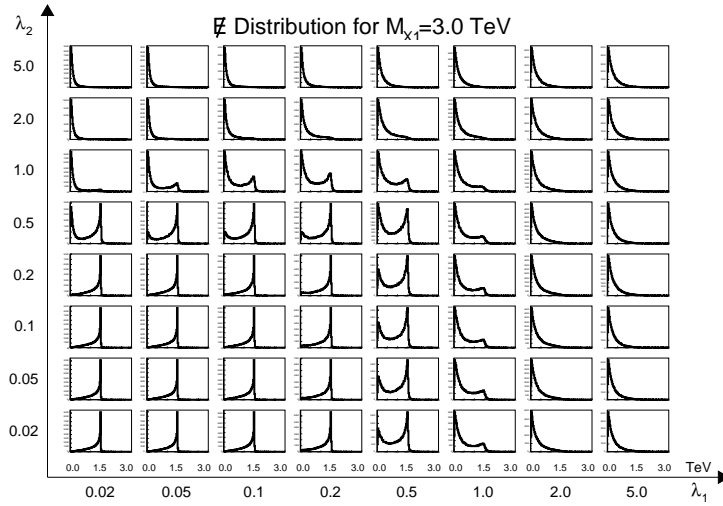
(a)
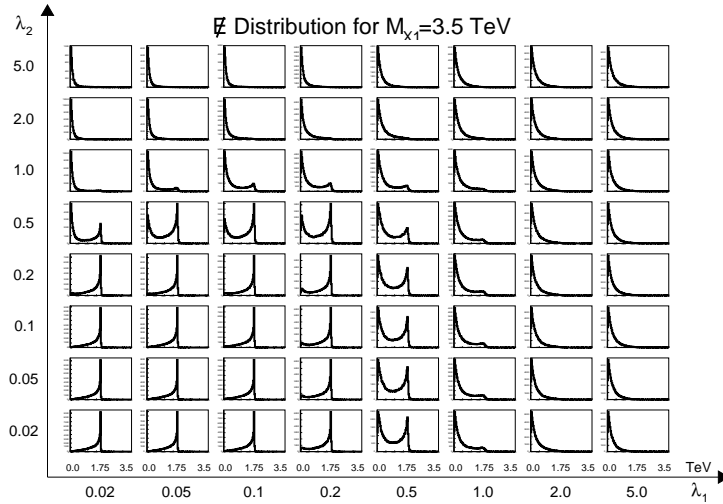
(b)

Figure 9.1: Generator level $\not{E}_T$ for M$_{X_1}$ (a) 3.0 TeV and (b) 3.5 TeV as a function of (λ_1, λ_2).

Mass Distribution M$_{\text{X1}}$ and Mass Width Γ

λ_1	M$_{\text{X}_1}$ Width (Γ) [GeV]							
	λ_2=0.02	λ_2=0.05	λ_2=0.10	λ_2=0.20	λ_2=0.50	λ_2=1.00	λ_2=2.00	λ_2=5.00
0.02	0.215	0.591	1.93	7.303	44.89	179.1	716.1	4475
0.05	0.967	1.342	2.685	8.055	45.64	179.9	716.9	4476
0.10	3.652	4.027	5.370	10.74	48.33	182.6	719.6	4478
0.20	14.39	14.77	16.11	21.48	59.07	193.3	730.3	4490
0.50	89.58	89.95	91.29	96.66	134.2	268.5	805.5	4564
1.00	358.0	358.4	359.8	365.2	402.7	537.0	1074	4833
2.00	1432	1433	1434	1439	1477	1611	2148	5907
5.00	8950	8951	8952	8958	8995	9129	9666	13425

Table 9.1: Mass width of M$_{\text{X}_1}$ = 3.0 TeV for different coupling points in (λ_1, λ_2) parameter grid.

λ_1	M$_{\text{X}_1}$ Width (Γ) [GeV]							
	λ_2=0.02	λ_2=0.05	λ_2=0.10	λ_2=0.20	λ_2=0.50	λ_2=1.00	λ_2=2.00	λ_2=5.00
0.02	0.251	0.6891	2.255	8.520	52.37	209.0	835.5	5221
0.05	1.127	1.566	3.1326	9.398	53.26	209.9	836.4	5222
0.10	4.260	4.699	6.265	12.53	56.39	213.0	839.5	5225
0.20	16.79	17.22	18.79	25.06	68.91	225.5	852.0	5237
0.50	10.45	104.9	106.5	112.8	156.6	313.2	939.8	5325
1.00	417.7	418.2	419.7	426.04	469.9	626.5	1253	5638
2.00	1671	1671	1672	1679	1723	1879	2506	6891
5.00	10442	10443	10444	10451	10494	10651	11277	15663

Table 9.2: Mass width of M$_{\text{X}_1}$ = 3.5 TeV for different coupling points in (λ_1, λ_2) parameter grid.
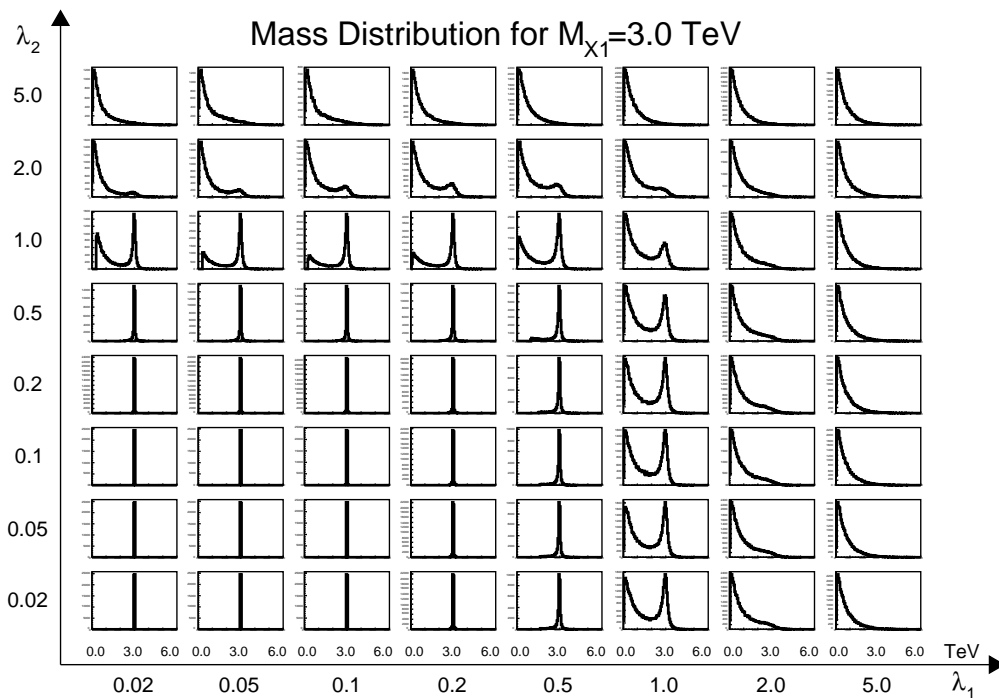
(a)
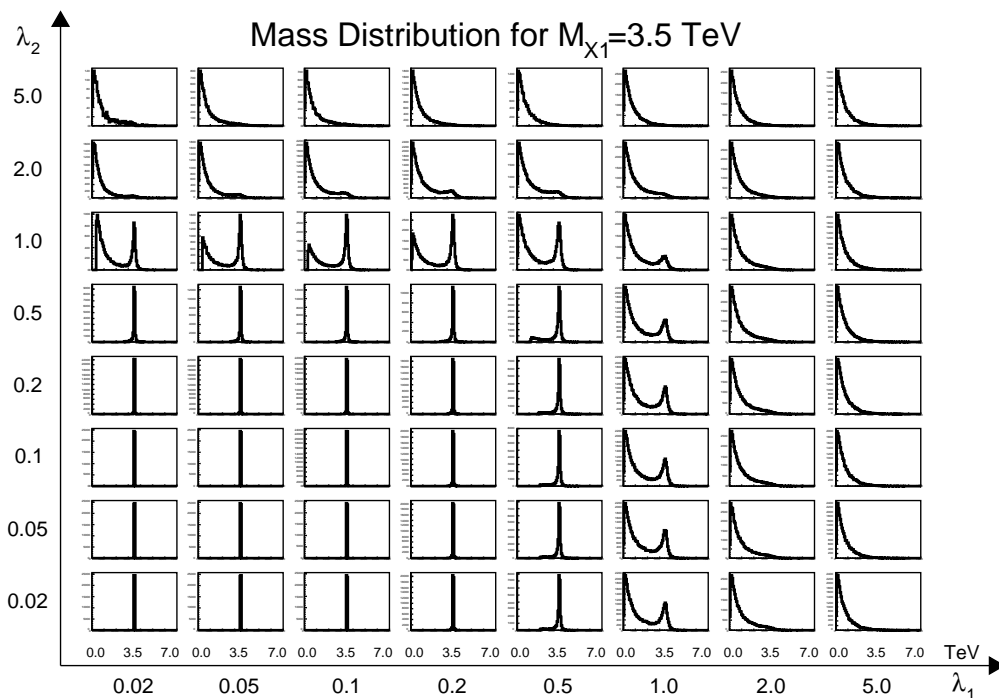
(b)

Figure 9.2: Mass distribution for M_{X_1} (a) 3.0 TeV and (b) 3.5 TeV as a function of (λ_1, λ_2).
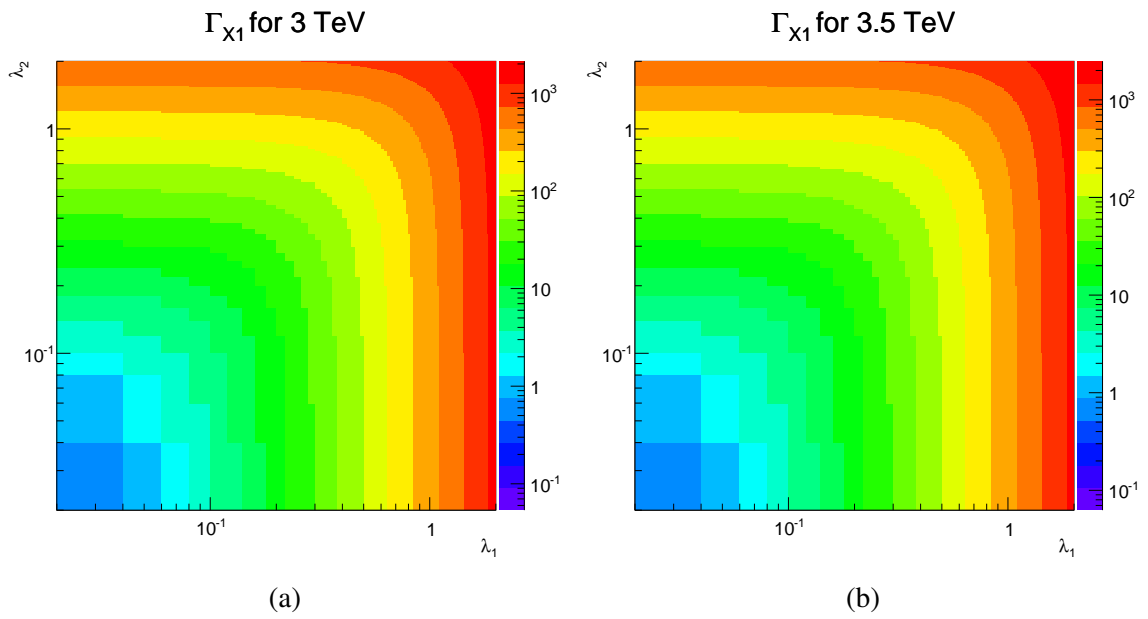
Figure 9.3: Mass Width for M_{X_1} (a) 3.0 TeV and (b) 3.5 TeV as a function of (λ_1, λ_2).

Cross-section vs Coupling and M$_{X1}$

λ_1	Cross-Section σ [pb] (M$_{X_1}$ = 3 TeV)			
	λ_2=0.05	λ_2=0.10	λ_2=0.20	λ_2=0.50
0.01	0.000009	0.00001	0.00001	0.00003
0.02	0.00003	0.00003	0.00004	0.00006
0.05	0.00008	0.00016	0.00022	0.00030
0.10	0.00011	0.00032	0.00067	0.00117
0.20	0.00013	0.00047	0.00144	0.00396
0.50	0.00018	0.00072	0.00276	0.01377
1.00	0.00037	0.00147	0.00574	0.03472
2.00	0.00082	0.00367	0.01406	0.08983
5.00	0.00068	0.00264	0.01147	0.07175

Table 9.3: Non-thermal DM model cross-sections for combined monojet and 2 jets plus $\not{E}_T$ signal for various λ_1 with M$_{X_1}$ = 3.0 TeV while keeping λ_2 fixed.

λ_1	Cross-Section σ [pb] (M$_{X_1}$ = 3.5 TeV)			
	λ_2=0.05	λ_2=0.10	λ_2=0.20	λ_2=0.50
0.01	0.000002	0.000003	0.000004	0.000014
0.02	0.000009	0.000012	0.000013	0.000028
0.05	0.000026	0.000052	0.000075	0.000124
0.10	0.000035	0.000108	0.000229	0.000452
0.20	0.000043	0.000162	0.000510	0.001565
0.50	0.000078	0.000309	0.001206	0.007139
1.00	0.000184	0.000751	0.003031	0.018151
2.00	0.000480	0.001992	0.008448	0.050313
5.00	0.000434	0.002006	0.007150	0.047301

Table 9.4: Non-thermal DM model cross-sections for combined monojet and 2 jets plus $\not{E}_T$ signal for various λ_1 with M$_{X_1}$ = 3.5 TeV while keeping λ_2 fixed.
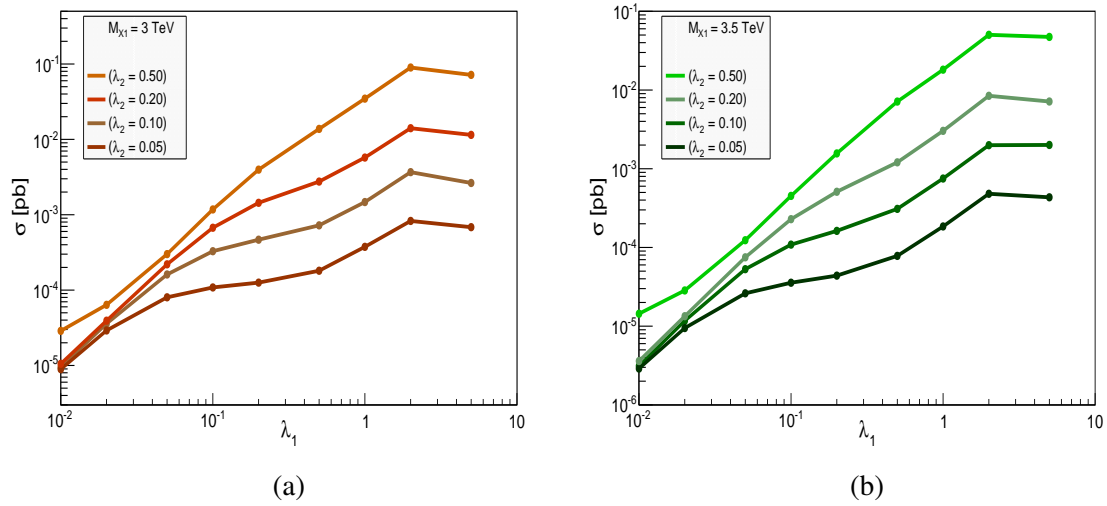
Figure 9.4: Cross-section σ as a function of coupling λ_1 for M_{X_1} = (a) 3.0 TeV and (b) 3.5 TeV.

APPENDIX B: KINEMATICS PLOTS IN SIGNAL AND CONTROL REGIONS

Signal Region

(a)   (b)
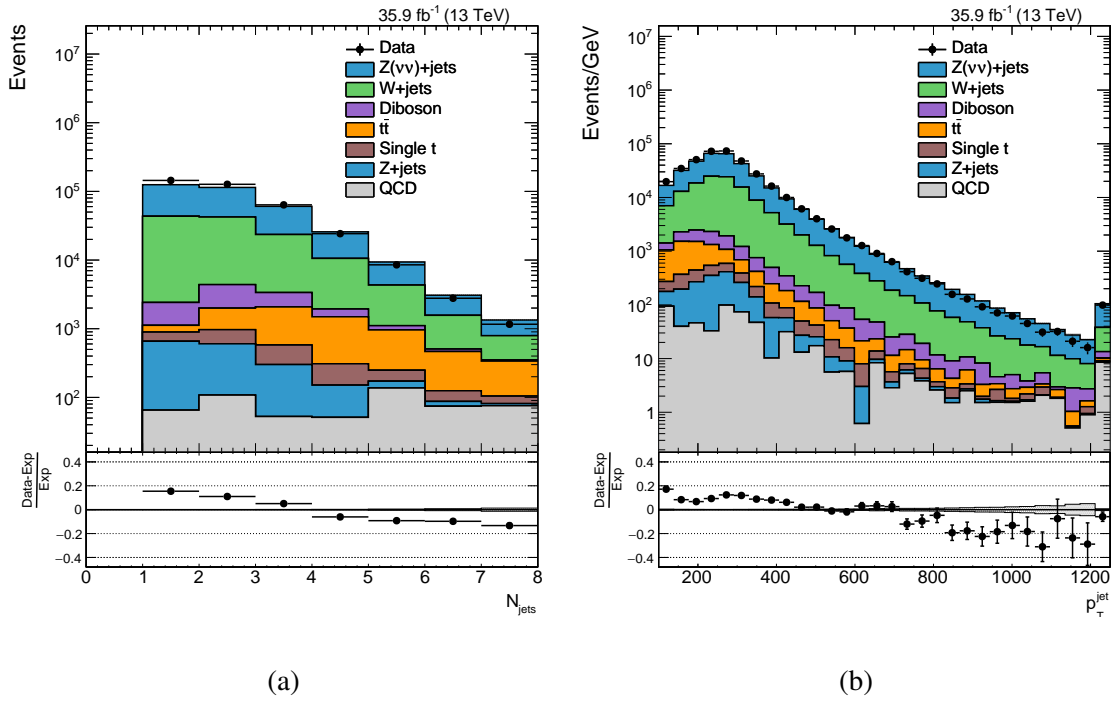
Figure 9.5: Comparison between data and Monte Carlo simulation in the signal region for (a) AK4 jet multiplicity and (b) leading jet p_T.

Dimuon CR

(a)

(b)

(c)

(d)
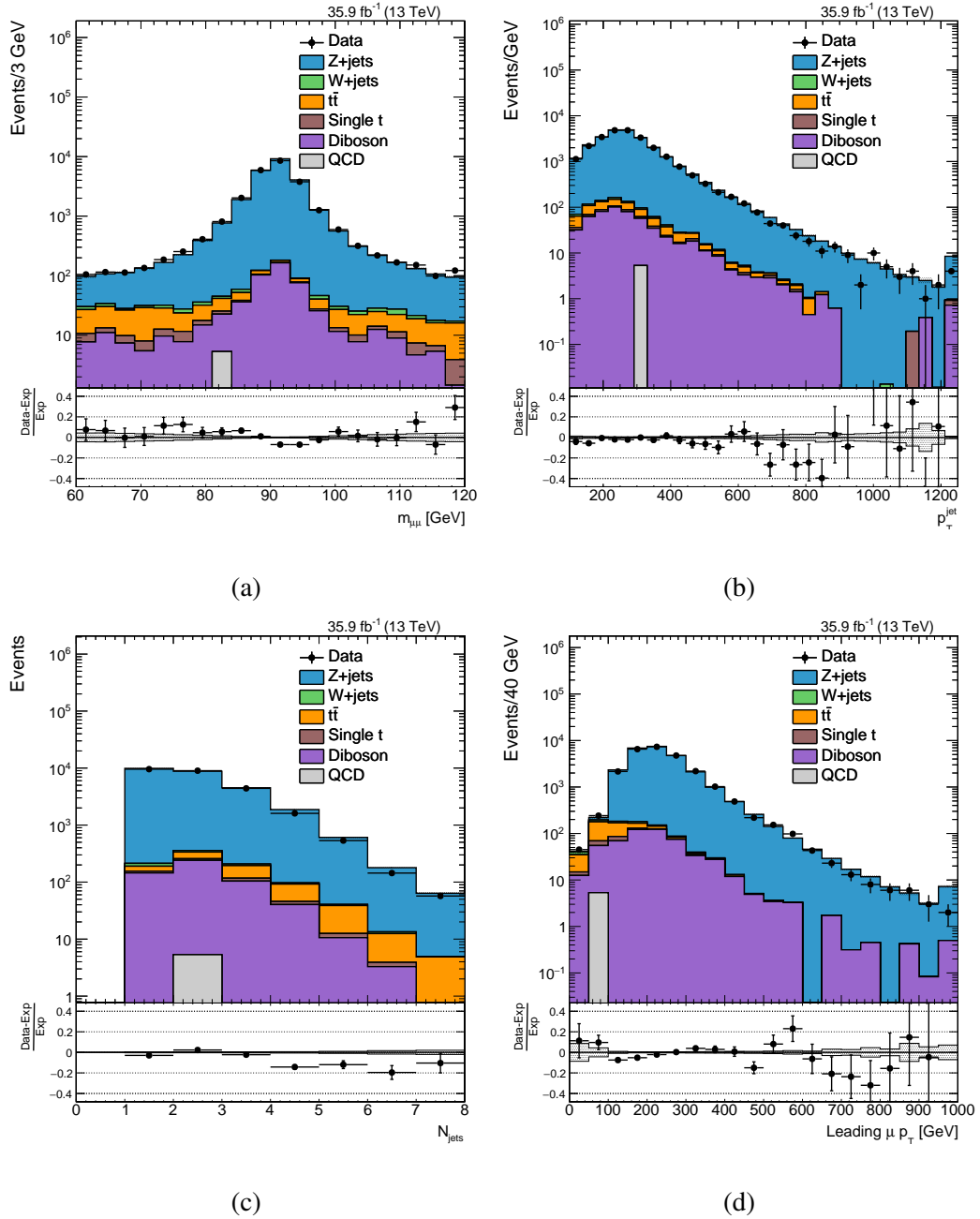
Figure 9.6: Comparison between data and Monte Carlo simulation in the dimuon region for (a) dimuon mass distribution, (b) leading jet p_T, (c) AK4 jet multiplicity and (d) leading muon p_T.
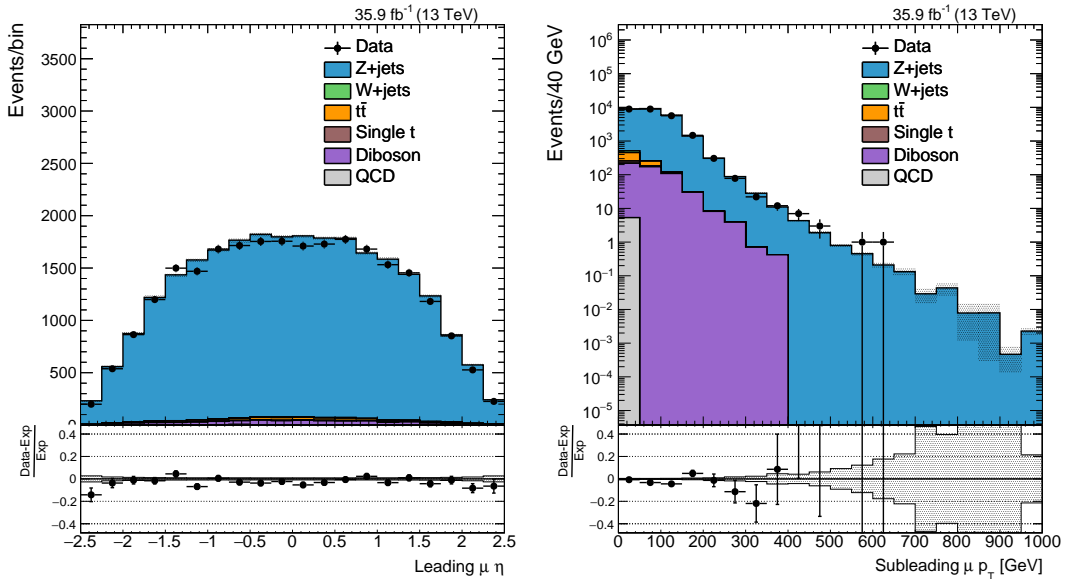
(a)

(b)
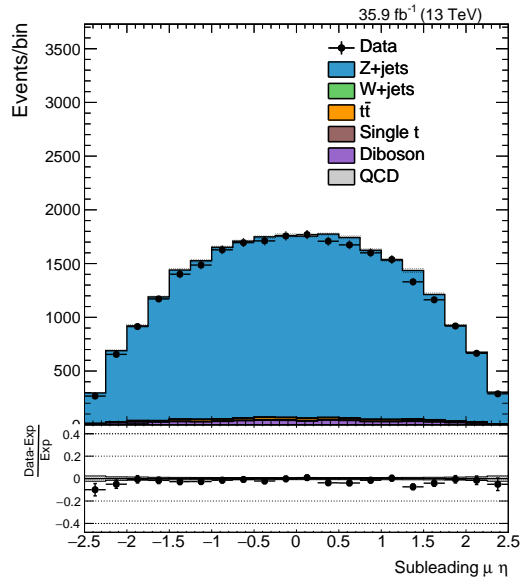
(c)

Figure 9.7: Comparison between data and Monte Carlo simulation in the dimuon region for (a) leading muon η, (b) sub-leading muon p_T and (c) sub-leading muon η.
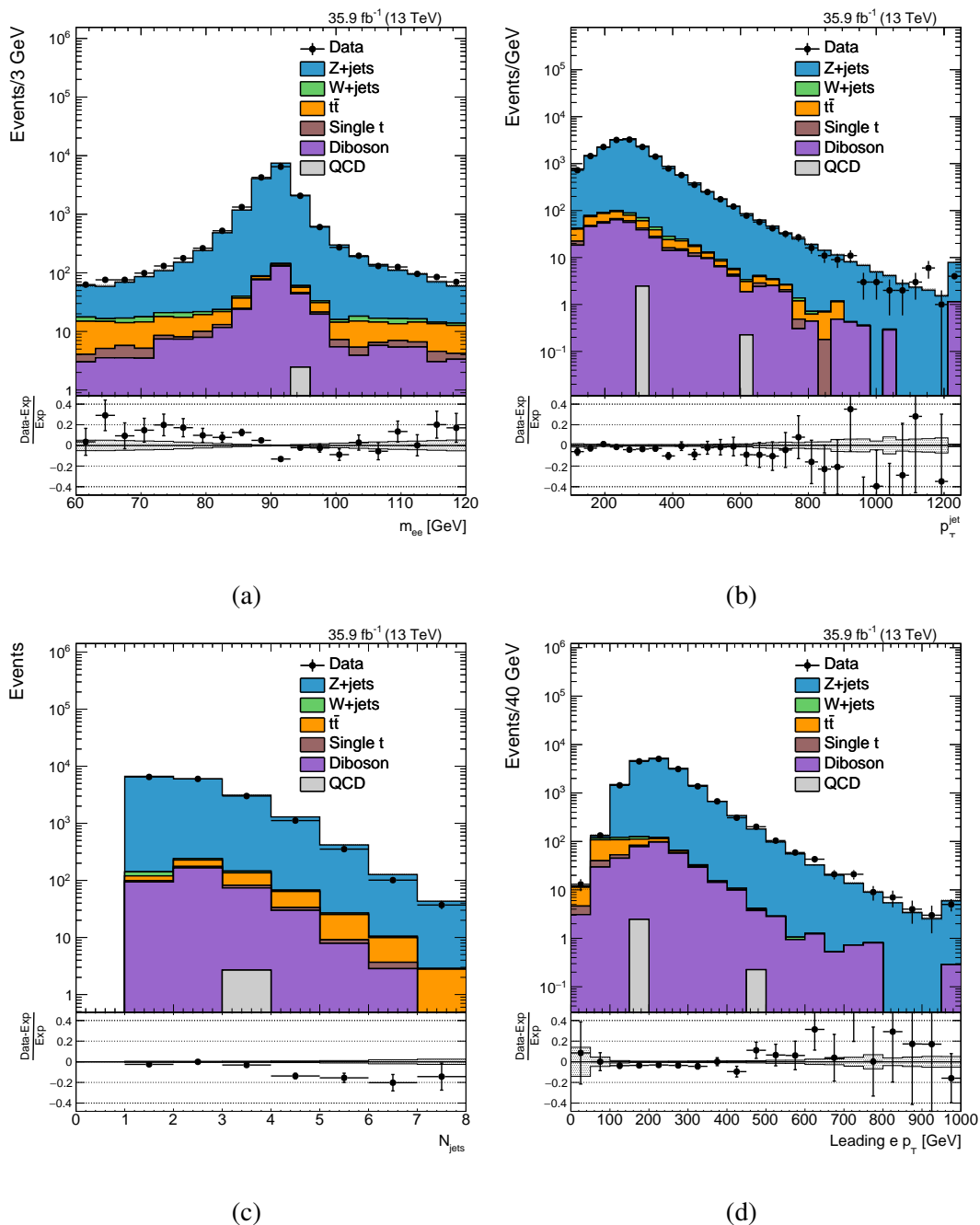
Double Electron CR

Figure 9.8: Comparison between data and Monte Carlo simulation in the double electron control region for (a) dielectron mass distribution, (b) leading jet p_T, (c) AK4 jet multiplicity and (d) leading electron p_T.
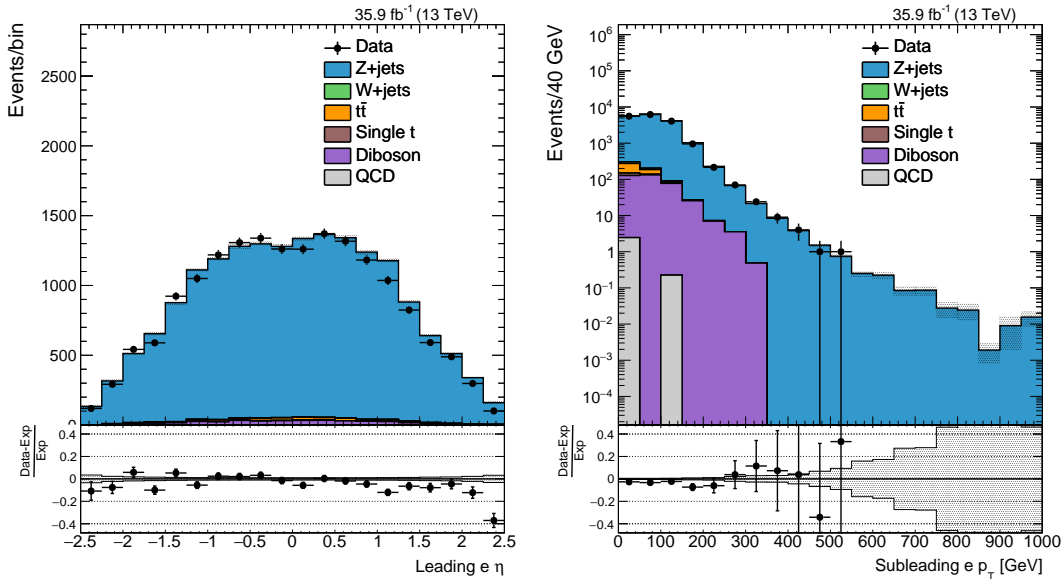
(a)

(b)
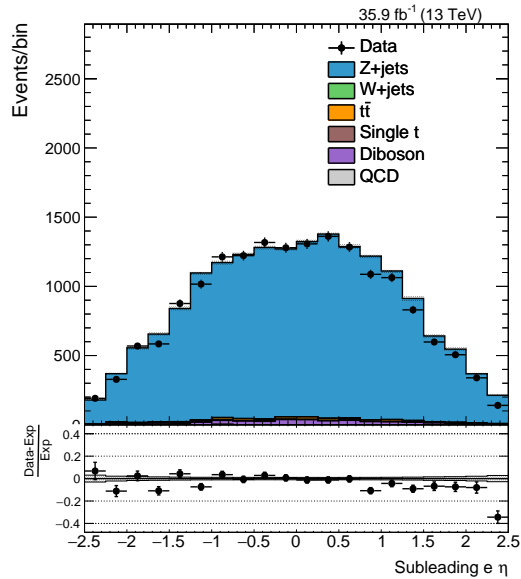
(c)

Figure 9.9: Comparison between data and Monte Carlo simulation in the double electron control region for (a) leading electron η, (b) sub-leading electron p_T and (c) sub-leading electron η.
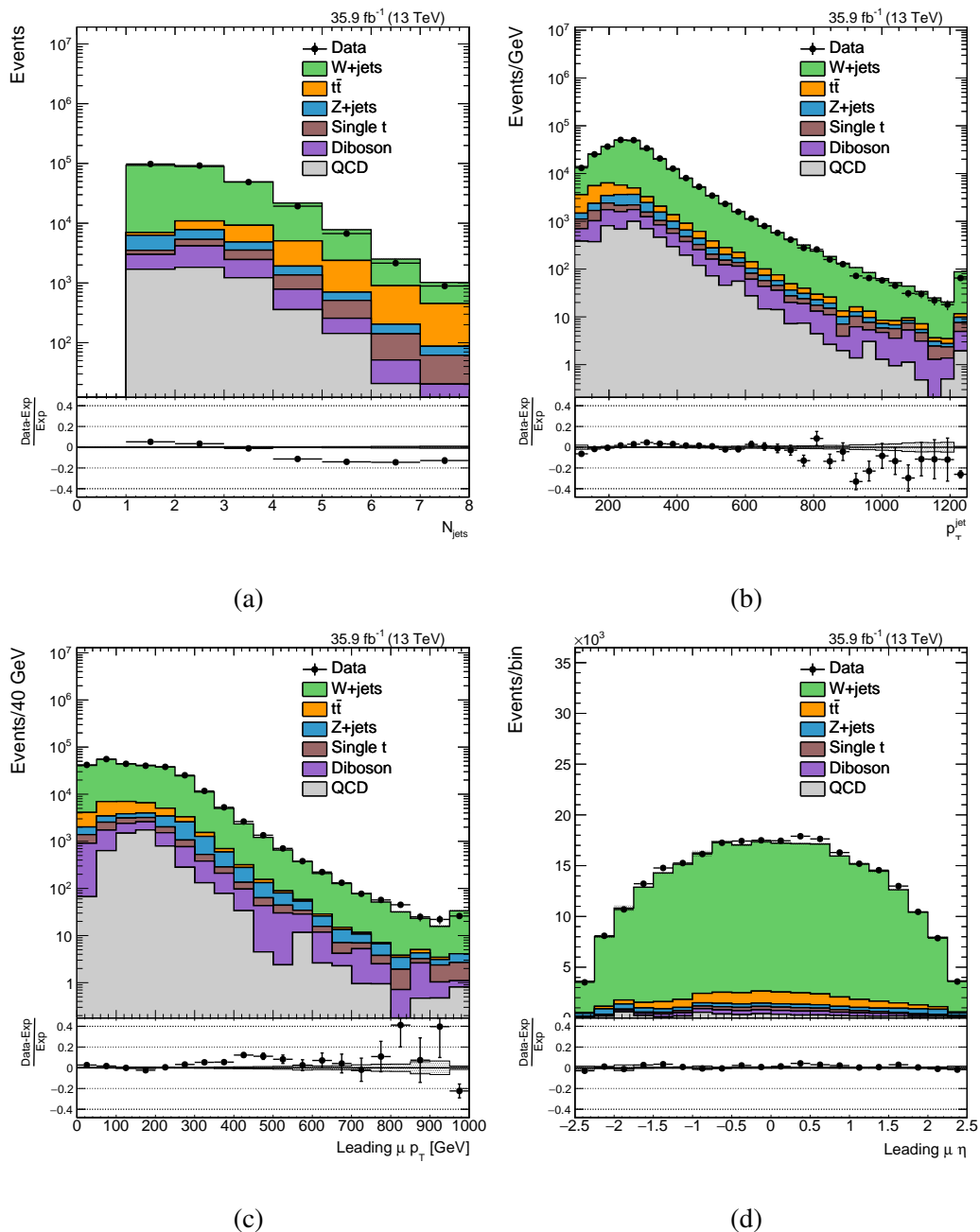
Single Muon CR

Figure 9.10: Comparison between data and Monte Carlo simulation in the single muon control region for (a) AK4 jet multiplicity, (b) leading jet p_T, (c) leading muon p_T and (d) leading muon η.

Single Electron CR

(a)

(b)

(c)

(d)
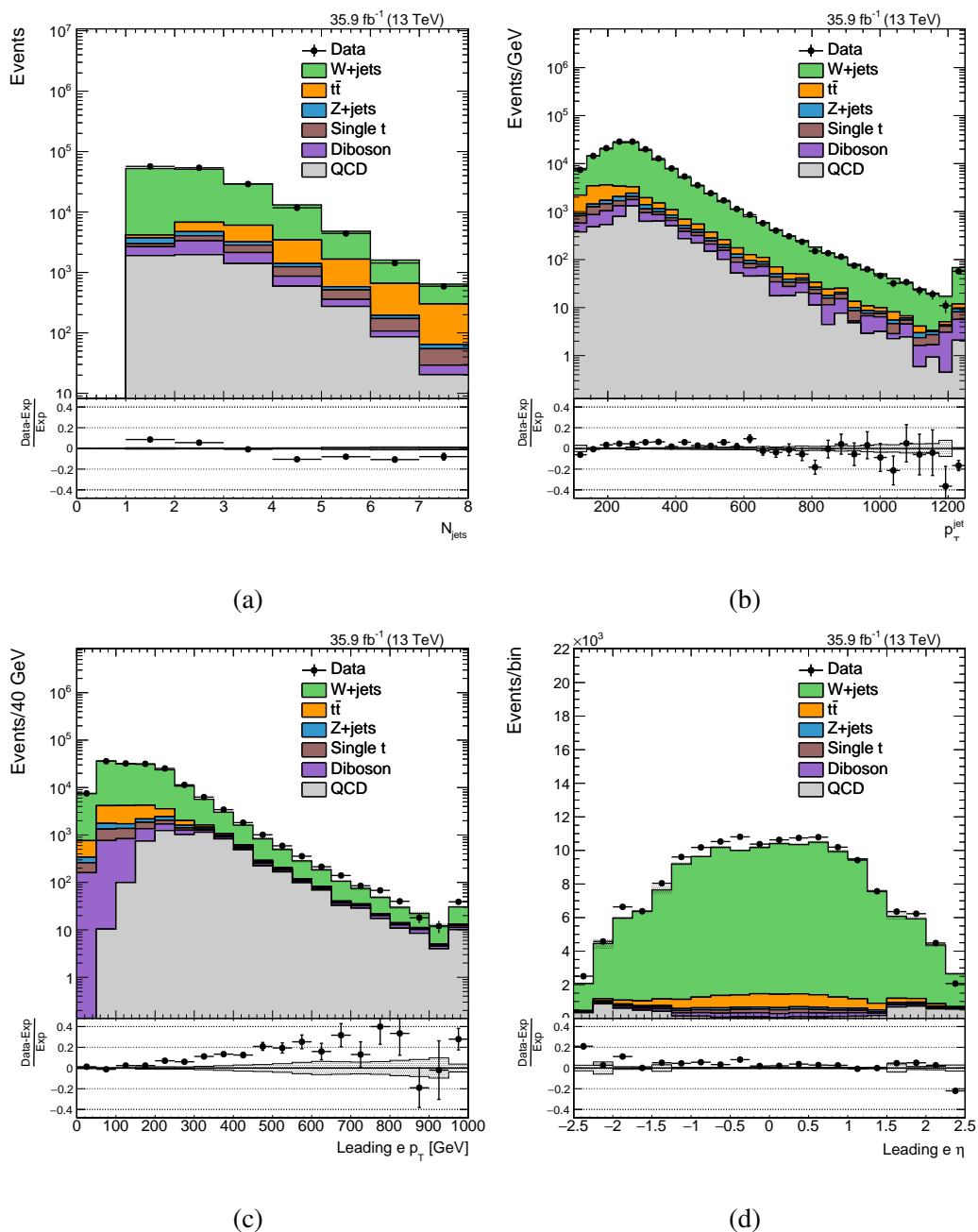
Figure 9.11: Comparison between data and Monte Carlo simulation in the single electron control region for (a) AK4 jet multiplicity, (b) leading jet p_T, (c) leading electron p_T and (d) leading electron η.
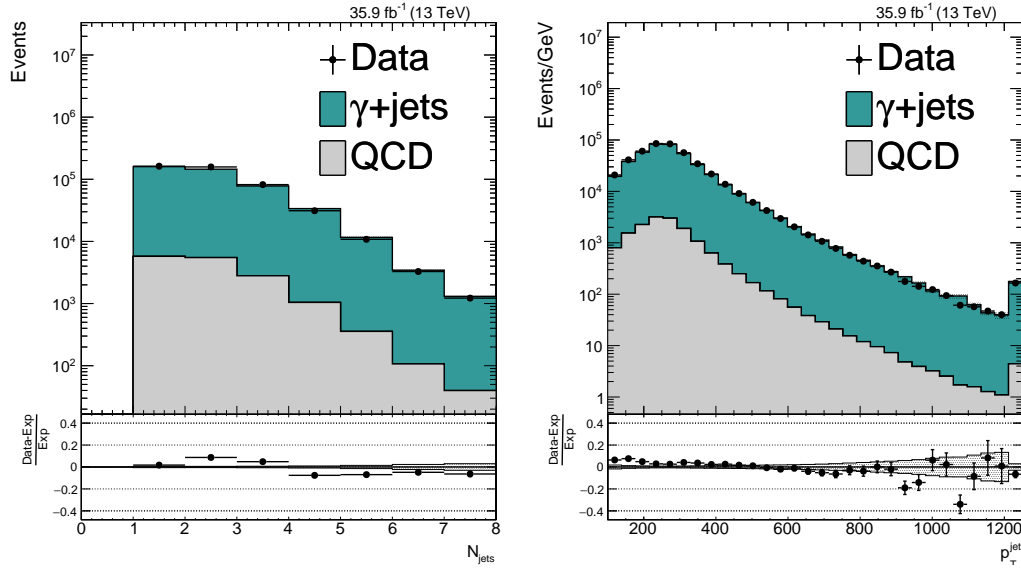
Single Photon CR

(a)

(b)
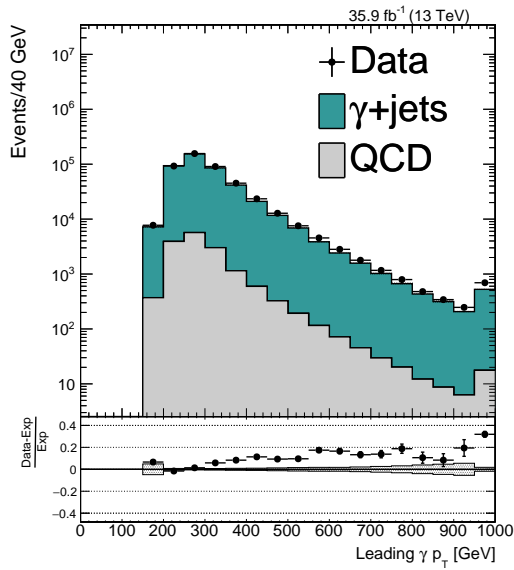
(c)

Figure 9.12: Comparison between data and Monte Carlo simulation in the single photon control region for (a) AK4 jet multiplicity, (b) leading jet p_T and (c) photon p_T .

APPENDIX C: POST-FIT RECOIL PLOTS

Control Region Only Fit
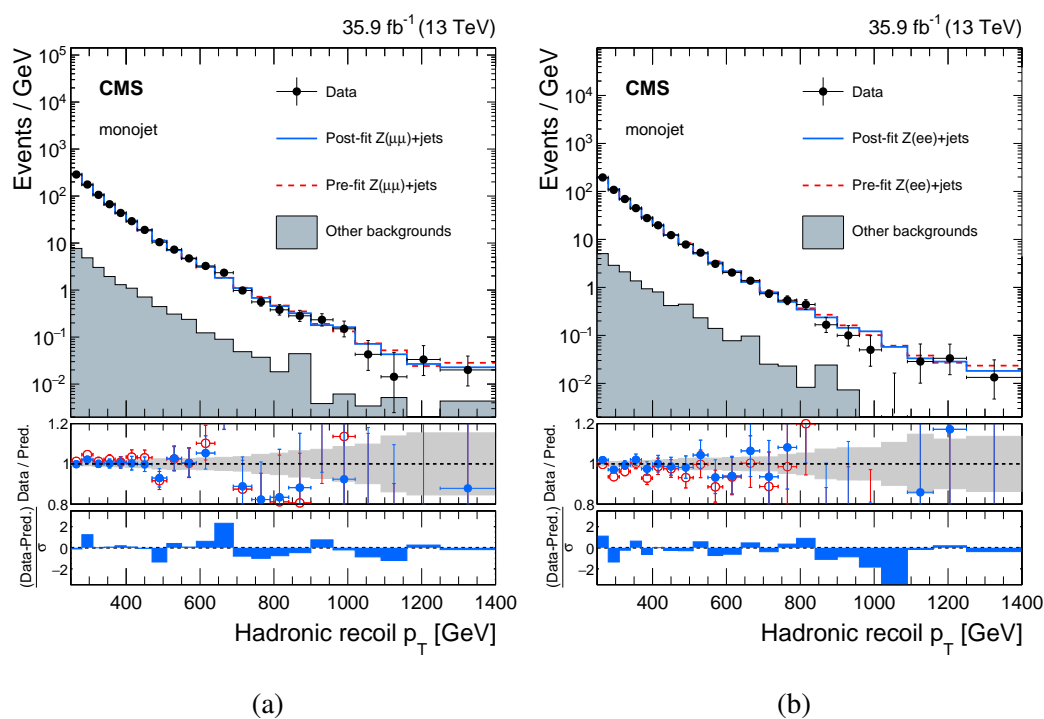
Figure 9.13: MC and data are compared for (a) dimuon and (b) dielectron control regions before and after the control region only fit. Experimental and theoretical uncertainties are represented by gray bands in ratio plots. An improved agreement between data and MC is seen [146].
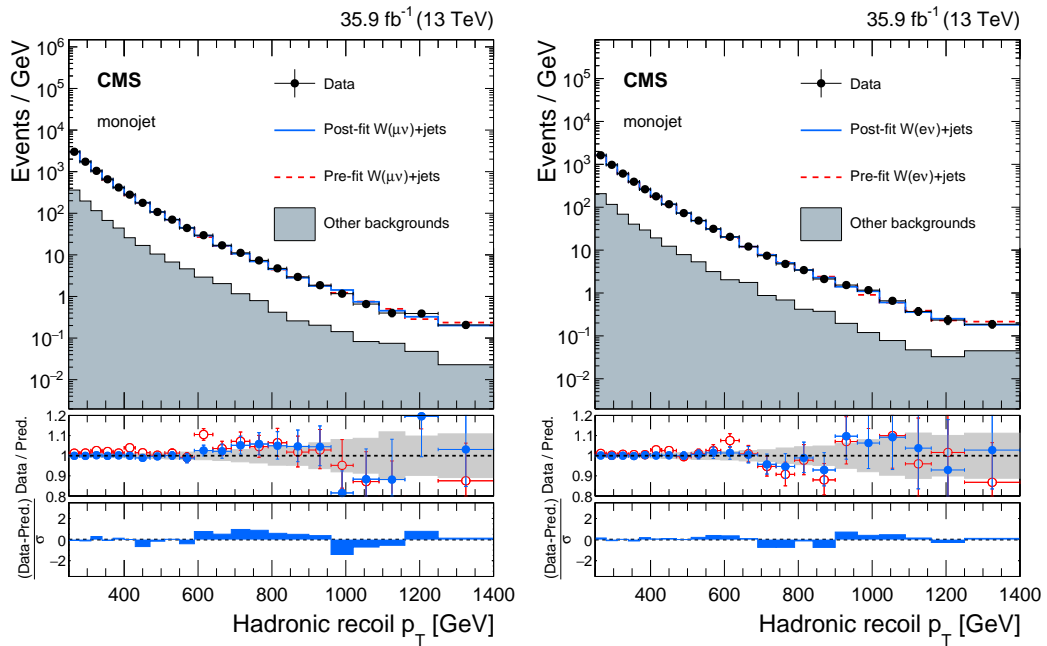
(a)

(b)
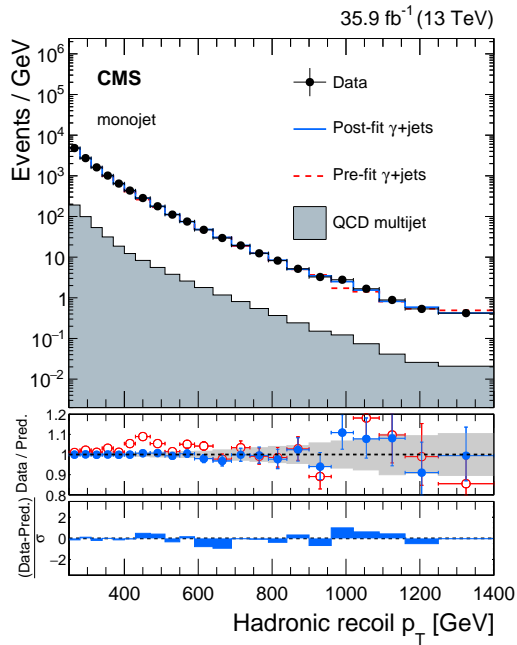
(c)

Figure 9.14: MC and data are compared for (a) single muon, (b) single electron and (c) single photon control region before and after the control region only fit. Experimental and theoretical uncertainties are represented by gray bands in ratio plot. An improved agreement between data and MC is seen [146].

147

Control Region and Signal Region Background only Fit
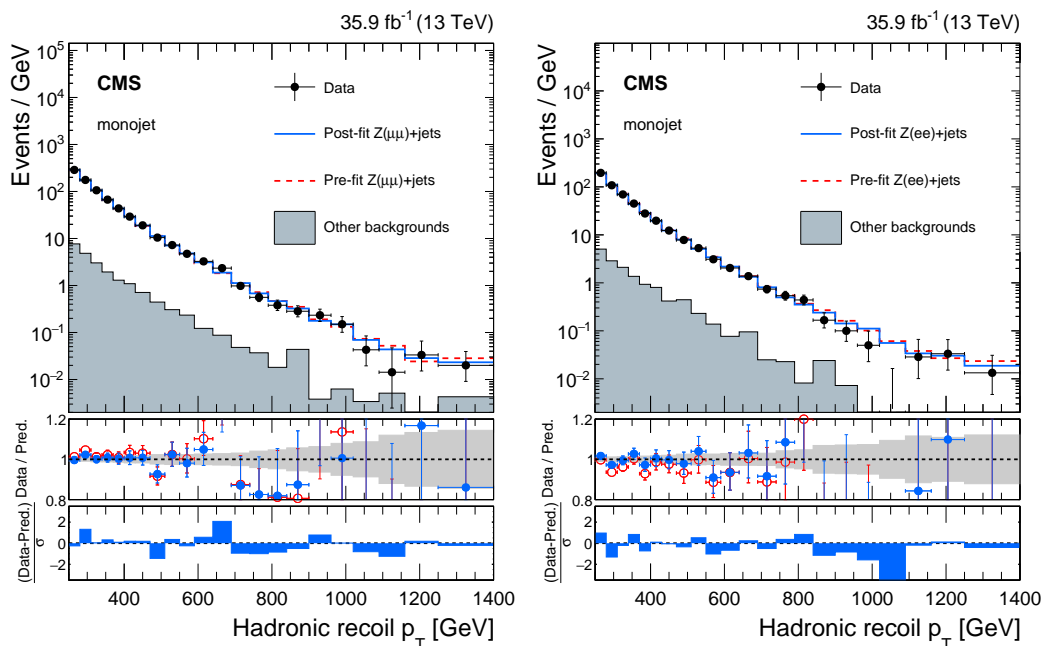
Figure 9.15: MC and data are compared for (a) dimuon and (b) dielectron control regions before and after the control region plus signal region background only fit. Experimental and theoretical uncertainties are represented by gray bands in ratio plots. An improved agreement between data and MC is seen [146].
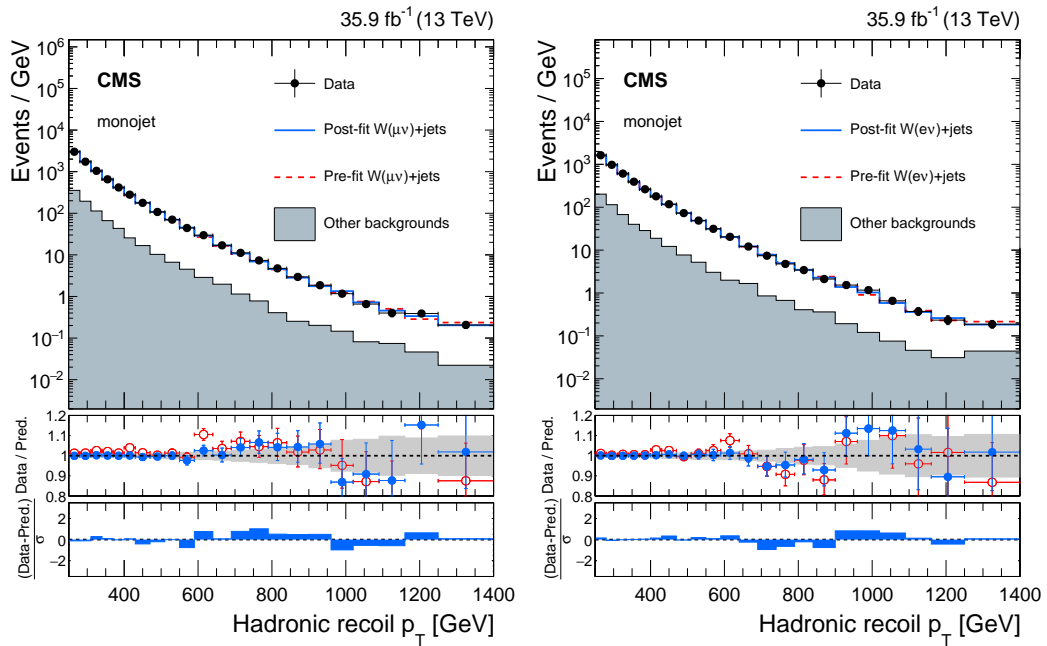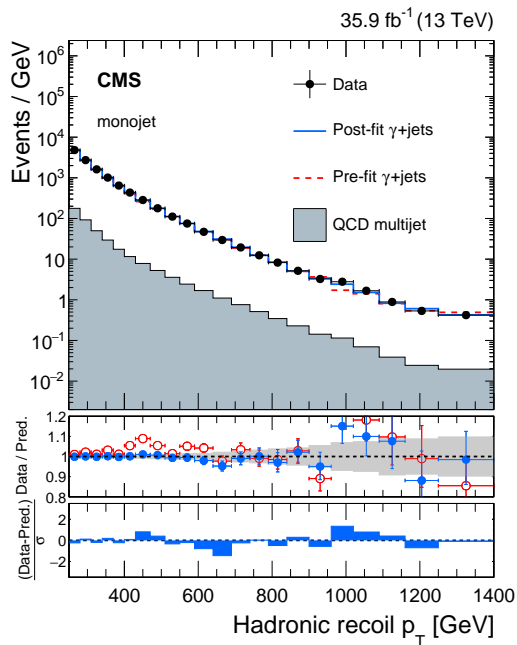
Figure 9.16: MC and data are compared for (a) single muon, (b) single electron and (c) single photon control region before and after the control region plus signal region background only fit. Experimental and theoretical uncertainties are represented by gray bands in ratio plot. An improved agreement between data and MC is seen [146].

APPENDIX D: THEORY UNCERTAINTIES

The variation in several uncertainties for W/Z transfer factors as a function of recoil, is shown in Figure 9.17. Left plot shows QCD-NLO uncertainties, whereas impact of NLO-EW uncertainties is shown in right plot. QCD-NLO process dependent uncertainties have the largest values, varying from 1.5-0.5%, while PDF and QCD-EW mixing nuisances show negligible effect. The legend N^{3}LO in NLO-EW uncertainties plot represents all three Sudakov uncertainties, whose effect is large at higher values of boson p_T and can reach up to 2% each.
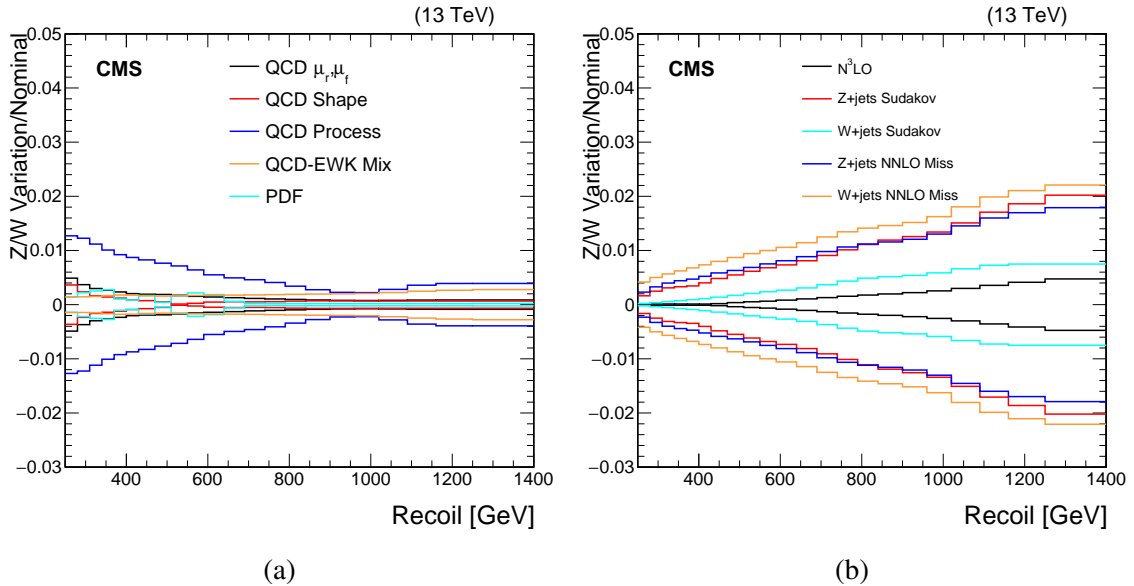
Figure 9.17: Theory uncertainties on W/Z ratio: (a) QCD-NLO nuisances and uncertainty related to mixing of QCD-NLO and EW-NLO, (b) variation of NLO electroweak nuisances [146].

The nuisances on Z/γ ratio are summarized in Figure 9.18. Similar to W/Z case, left plot shows fluctuations in QCD-NLO uncertainties and right plot sums up NLO-EW nuisances. Process dependent QCD-NLO uncertainties are dominant, changing from -2% for hadronic recoil < 400 GeV to +2% for larger values. Identical alternate sign of uncertainties is seen

for QCD-NLO renormalization and factorization scale and shape nuisances, but the effect is small. QCD-EW mixing is negligible for the whole range of recoil.

(a)   (b)
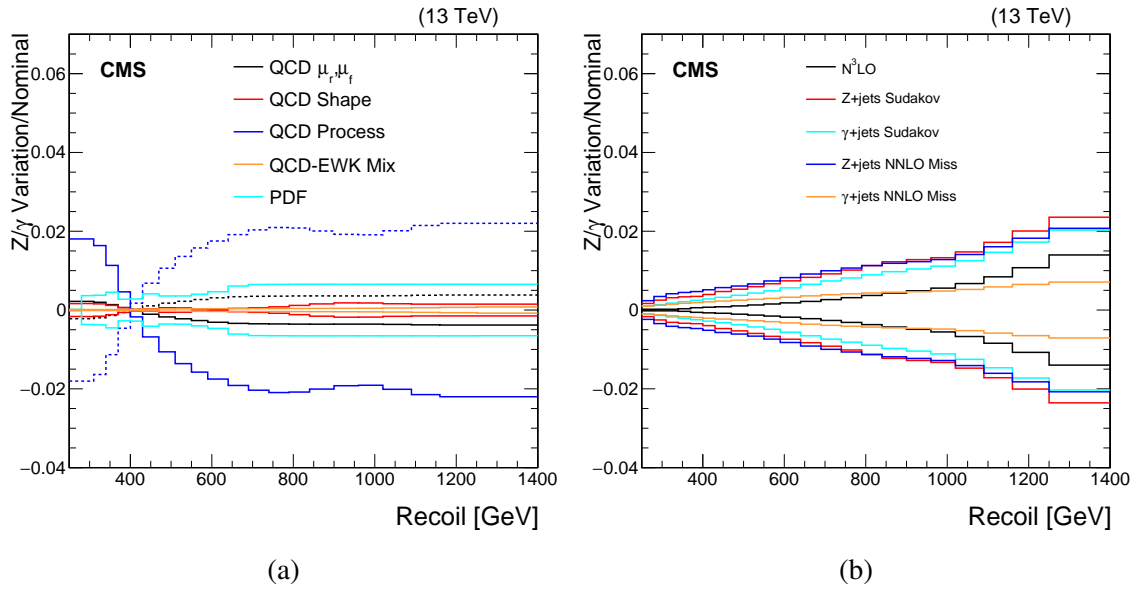
Figure 9.18: Theory uncertainties on γ/Z ratio: (a) QCD-NLO nuisances and uncertainty related to mixing of QCD-NLO and EW-NLO, (b) variation of NLO electroweak nuisances [146].